Master's Thesis
IB-RM-OP-2017-201

3D Kinematic Modeling and Evaluation of Rough-Terrain Locomotion Modes for an ExoMars-like Mobility Subsystem

Tim Wiese

Supervisor:
Prof. Dr.-Ing. Alin Albu-Schäffer

Advisors:
Dr.-Ing. Armin Wedler (DLR)
Pantelis Poulakis (ESA)

DLR – German Aerospace Center
Robotics and Mechatronics Center

Deutsches Zentrum
für Luft- und Raumfahrt
German Aerospace Center

Institut für Robotik und Mechatronik	BJ.: 2017 IB.Nr.: DLR-IB-RM-OP-2017-201

MASTER'S THESIS

3D KINEMATIC MODELING AND EVALUATION OF ROUGH-TERRAIN LOCOMOTION MODES FOR AN EXOMARS-LIKE MOBILITY SUBSYSTEM

Freigabe:	Der Bearbeiter:	Unterschriften
	Tim Wiese	
	Betreuer:	
	Dr.-Ing. Armin Wedler	
	Der Institutsdirektor	
	Prof. Alin Albu-Schäffer	

Dieser Bericht enthält 102 Seiten, 40 Abbildungen und 14 Tabellen

Ort: Oberpfaffenhofen	Datum:	Bearbeiter:	Zeichen:

Acknowledgements

It has been a long and adventurous journey on the way to my Master's thesis and there were many people on the sidelines without whom things would not have worked out the way they did. Here, I would like to acknowledge those that were essential for its success.

First of all, I would like to thank Prof. Alin Albu-Schäffer for supervising my thesis and Armin Wedler and Pantelis Poulakis for being my advisors. Armin, thank you for taking me in and placing your trust in my judgement and my abilities many times. The project was definitely a challenge but so far, I think, quite a success. Pantelis, you started this journey four years ago when I received a phone call from your office on a cold December evening. When I started my studies, I could only have dreamed about being involved in a project that would actually fly to Mars.

Additionally, I would like to thank everyone at DLR who was involved in the project in one way or the other. A special mention goes to Bernhard Rebele, the soil master, who did most of the dirty work in the lab and was always available for help and advice. Another dedicated thanks goes to Benedikt Pleintinger with whom I spent countless hours rewiring and debugging the rover electronics. Some others I would like to mention that were instrumental in hardware and software support are Wieland Bertleff, Tim Bodenmüller, Kristin Bussmann, Josef Reill and Florian Schmidt. As well as countless others who were available for help and advice.

I would also like to thank Fabian Beck for the – mostly worthwhile – discussions on mathematical notation and LaTeX formatting, as well as for supplying our office with a never-ending stash of chocolate.

And last – but definitely not least – I would like to thank my parents for supporting me at all times and allowing me to reach for the stars and follow my dreams. I love you, always!

Abstract

One of the main challenges of planetary rover missions is the traversability of rough terrain areas, steep slopes and very soft soil fields. In the past, rovers repeatedly struggled while driving especially in these soft soils, with the Spirit rover even having to be abandoned [1]. With ESA's upcoming ExoMars mission, a rover with an articulated suspension will land on Mars in 2021 that offers additional degrees of freedom through its actuated deployment joints. A full-body kinematic model allows to take full advantage of such a locomotion system. In this thesis, such a model was derived for EXM-BB2, a mobility subsystem prototype for the ExoMars rover. It features a similar suspension design with 18 active and 3 passive joints as well as flexible wheels and allows for rapid development and testing through a common software and electronics stack shared with other robotic systems at DLR.

The formulation of the kinematic model is based on a systematic velocity propagation approach. Wheel-terrain contact angles are estimated through force-torque sensors installed at the wheel hubs. The model allows to specify desired body velocities and additional constraints on joint rates to achieve desired motions and includes a slip formulation on wheel level. Additionally, kinematic redundancies can be exploited by the introduction of secondary sub-tasks through null-space projection. Based on this kinematic model, two locomotion modes were implemented for increased traversability performance in rough terrain: Balancing, a mode for body pose adjustment that allows to increase the rover's tip-over stability and decrease its body tilt, and Wheel Walking, a mode for increasing gradeability on slopes and traction in soft soils.

The effectiveness of the kinematic model and the locomotion modes were shown in a series of tests in the Planetary Exploration Laboratory at DLR. Balancing was able to reduce the rover body pitch and yaw angle by 5° in uneven terrain and decrease side-slip while driving sideways along a slope by more than 50%. Wheel Walking managed to outperform Normal Driving (which only actuates the rover wheels) significantly in terms of traction on a slope both for the full-body kinematic model as well as for a simplified, 2D-kinematic implementation. Using Wheel Walking, the rover managed to traverse a 30° slope with 70% of slip while Normal Driving failed at 21°. Additionally, using Wheel Walking, energy consumption for slope traversal could be reduced by 50%.

Contents

List of Figures

List of Tables

List of Acronyms

ABA Axle-by-Axle Gait
BLP Balancing Platform Tests
BLS Balancing Sideways Slope Tests
BO Burnout
CL Center-Left
CoG Center of Gravity
CPU Central Processing Unit
CR Center-Right
DC Direct Current
DEP Deployment Joint
DFKI Deutsches Forschungszentrum für Künstliche Intelligenz
DH Denavit-Hartenberg
DLR Deutsches Zentrum für Luft- und Raumfahrt
DoF Degrees of Freedom
DRV Driving Joint
ESA European Space Agency
EXM ExoMars
FB Full Body
FL Front-Left
FR Front-Right
FTS Force-Torque Sensor
GUI Graphical User Interface
HYB Hybrid Gait
IMU Inertial Measurement Unit
KRU Kruse Gait
LN Links and Nodes
LRU Lightweight Rover Unit
MSL Mars Science Laboratory
NASA National Aeronautics and Space Administration
ND Normal Driving
OBS Obstacle Tests
PC Personal Computer

PEL Planetary Robotics Laboratory
RCL Rover Company Ltd.
RK Robotkernel
RL Rear-Left
Rock Robot Construction Kit
ROS Robot Operating System
RR Rear-Right
SBS Side-by-Side Gait
STR Steering Joint
SVD Singular Value Decomposition
SW Single Wheel Gait
TRI Tripod Gait
UDP User Datagram Protocol
WMR Wheeled Mobile Robot
WW Wheel Walking
WWC Wheel Walking Comparison Tests
WWT Wheel Walking Traversability Tests
WWX Wheel Walking Extreme Tests

1 Introduction

1.1 Motivation

The ExoMars mission is a joint project between the European Space Agency (ESA) and Roscosmos which aims to investigate the geological and atmospheric environment on Mars, carry on the search for life on the planet and demonstrate technologies for future exploration missions [2]. It consists of three main elements: The Trace Gas Orbiter, launched in 2016 together with the Schiaparelli Entry, Descent and Landing Demonstrator and now in orbit around Mars, and the ExoMars Rover, Europe's first planetary robotic vehicle, to be launched in 2020 (see Figure 1.1 for an artist's impression). The rover will be the first to feature flexible wheels as well as a drill for taking soil samples from a depth of up to two meters beneath the surface for chemical and microbiological analysis.

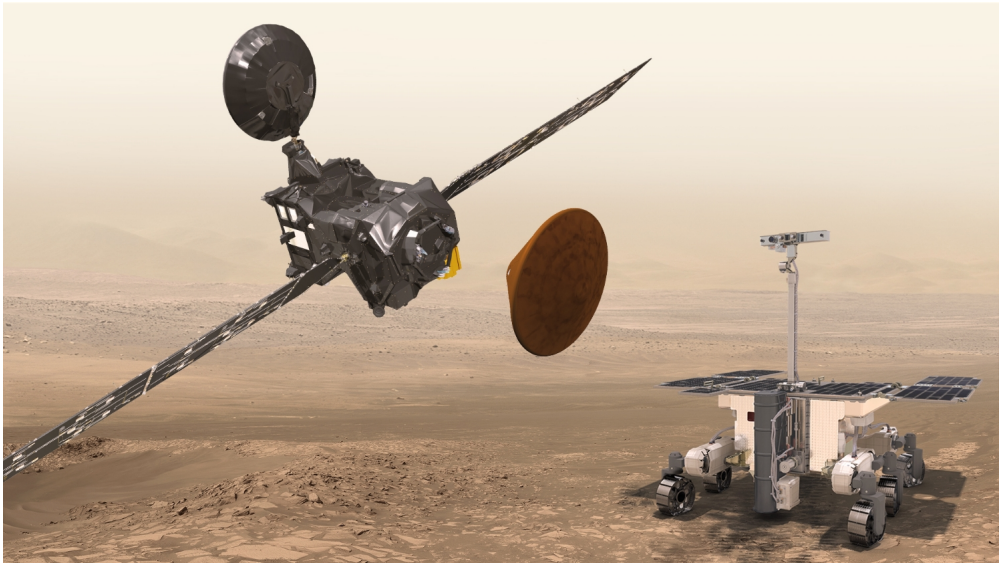

Figure 1.1: **Trace Gas Orbiter, Schiaparalli and ExoMars rover (taken from [3])**

The ExoMars rover features a triple-bogie suspension design with six steerable wheels, each with an additional deployment joint. These additional degrees of freedom could be used for a so-called "Wheel Walking" locomotion mode where the leg assemblies are rotated backwards and forwards during the rover motion, with the intended benefit of increased traction and driving stability in soft soils. This could improve gradeability on slopes, decrease wheel sinkage and provide additional safety margins for escaping from entrapment situations that could endanger the mission. Moreover, such a suspension design could allow for an adjustment of the rover body pose to shift its center of mass, increase tip-over stability and reduce the rover body tilt, e.g. to keep on-board experiments leveled while driving over obstacles or traversing slopes. Both methods could enlarge the traversability envelope, i.e. the areas the rover could traverse safely while performing scientific operations.

For simple locomotion modes with a small number of actuated joints, it is often sufficient to derive the joint command equations from a simple 2D geometric analysis of the problem (e.g. Ackermann steering). However, this introduces errors due to simplified assumptions like neglecting the motion of passive joints and ignoring wheel-terrain contact angles. For more sophisticated locomotion modes utilizing a higher number of actuated joints and aimed at driving in uneven terrain, such a geometric approach might even be infeasible or at least unnecessarily complex. To synchronize the motion of all available joints while taking into account terrain unevenness, a generic kinematic model can be created based on the rover joint configuration. Different locomotion modes – like Wheel Walking – can be implemented by introducing appropriate constraints. In addition to this, null-space projection methods allow for lower priority sub-tasks to be introduced, such as body pose adjustment.

1.2 Problem Statement

The EXM-BB2 rover at DLR is a phase B2 prototype of the ExoMars rover's mobility subsystem. It features a similar suspension configuration and wheel design with the same degrees of freedom and only slightly different physical dimensions. Equipped with commercial off-the-shelf electronics, an up-to-date desktop computing platform and DLR's own robotic middleware, it allows for open programming of joint actuator commands while processing data from sensors like an intertial measurement unit (IMU) and force-torque sensors (FTS). Before the beginning of this thesis, the rover's implemented driving abilities were limited to simple locomotion modes based on 2D geometric analysis. To make use of the additional degrees of freedom the platform offers while taking into account the motion of all available joints on rough terrain, a central part of this thesis was the derivation of

a full-body kinematic model for the rover. For estimation of the contact angles between wheels and terrain, a method was developed based on force-torque data provided by the sensors integrated at the platform's wheel hubs.

To analyze the benefits of the additional degrees of freedom in combination with the kinematic model, two locomotion modes were implemented:

1. A Balancing Mode for body pose adjustment, to increase the rover's tip-over stability and reduce body roll and pitch angle, based on IMU data.

2. Wheel Walking (WW) locomotion, to increase the rover's gradeability performance on slopes and increase traction in demanding driving situations.

The thesis was concluded with a two-week test campaign in DLR's Planetary Exploration Laboratory (PEL), a sand test bed facility, where the properties and behaviors of these modes were analyzed. For the Balancing Mode, its general behavior while driving over uneven terrain was tested as well as its impact on side-slip stability on a slope. For Wheel Walking locomotion, the tests covered comparisons of tractive performance and power consumption on a slope between Normal Driving, a simplified 2D Wheel Walking implementation and the implementation utilizing the full-body kinematic model, as well as between different Wheel Walking gaits and parameter settings.

1.3 Thesis Structure

This thesis is presented in nine chapters:

Chapter 1 serves as an introduction, describing the ExoMars mission, the motivation behind the thesis, its goals and contents.

The current State of the Art with respect to planetary rover locomotion is presented in **Chapter 2** with a look at past missions and the locomotion design of the upcoming ExoMars rover as well as kinematic modeling in general and Wheel Walking as a promising rover locomotion mode in particular.

The EXM-BB2 mobility subsystem rover, which was heavily modified in preparation of this thesis, is described in detail in **Chapter 3**. It gives an overview over its mechanical design, electronics, software and sensors.

The theoretical background behind the kinematic modeling approach, its application to the EXM-BB2 rover and the implementation of the advanced locomotion modes based on this model are presented in **Chapter 4**. It takes a specific look at the properties of the solution of the kinematic model and the handling of kinematic redundancies.

In **Chapter 5**, the setup and preparations for the tests of the implemented locomotion modes are mentioned, containing a description of the PEL sand test bed facility and describing the approach taken to fuse the tracking system data for multiple tracking targets on one rover body.

The results of the tests are presented in **Chapter 6**, both for the Balancing Mode and Wheel Walking locomotion, looking at performance and behavior of the implementations, power consumption and the impact of various parameters.

The report ends with discussion of the results in **Chapter 7**, a conclusion in **Chapter 8** and a discussion of potential future work in **Chapter 9**.

2 State of the Art

2.1 Planetary Rover Locomotion

2.1.1 Locomotion Concepts

Robotic exploration on Mars has been ongoing since over 20 years [4]. However, so far, only four rovers have driven on the surface of the planet: The Sojourner rover, launched in 1996 as part of the NASA Pathfinder mission, the MER rovers Spirit and Opportunity, launched by NASA in 2003, and the Curiosity rover, launched in 2011 as part of NASA's Mars Science Laboratory (MSL) mission (see Figure 2.1). All of these rovers feature a similar locomotion subsystem design: Six actuated wheels, with only the four corner wheels offering steering capability, arranged in a rocker-bogie passively compliant suspension layout. The wheels of these rovers are barrel-type wheels, with a hollow inside and a rigid outer driving surface equipped with grousers to increase traction on soft soil.

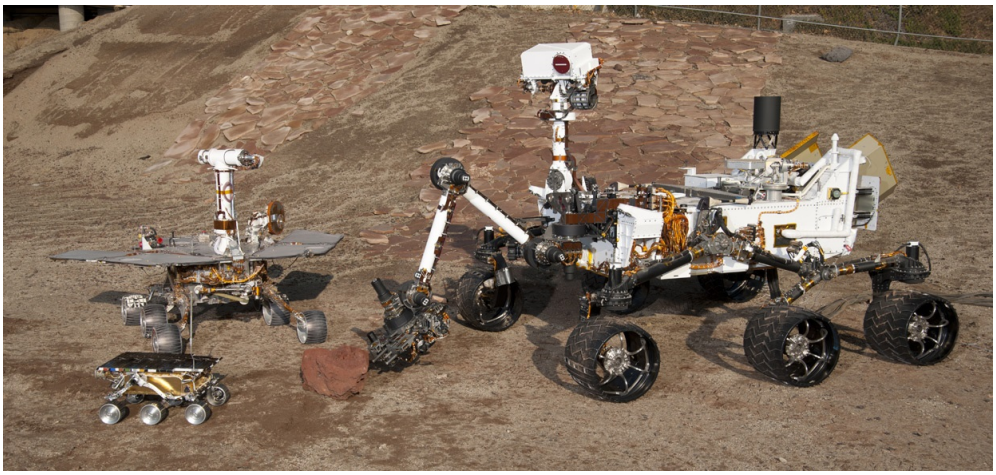

Figure 2.1: **NASA's Pathfinder, MER and MSL rovers (taken from [5])**

Many other types of suspension designs for planetary rovers have been proposed in the past. Some were even flown on other missions and are shown in Figure 2.2: The Soviet moon rovers Lunokhod 1 and 2, launched in 1970 and 1973, were the first mobile robotic vehicles operating on another planet [4]. They were driving on eight wheels, with each wheel suspended individually. In 1971, the Soviet Union launched the Mars 2 and 3 missions, which had the PrOP-M rover on board that featured a skiing-type locomotion system [6]. However, both missions failed during their arrival at Mars. In the 1990s, Russia planned to launch a rover called the Marsokhod during their Mars 96 mission [7]. It was designed to be able to negotiate obstacles up to twice the wheel diameter and climb slopes up to 45°, which was achieved through an articulated suspension with six large conically tapered cylindrical wheels that could move relative to each other. The rover was moved to the Mars 98 mission, which was canceled after the launch failure of Mars 96 [4].

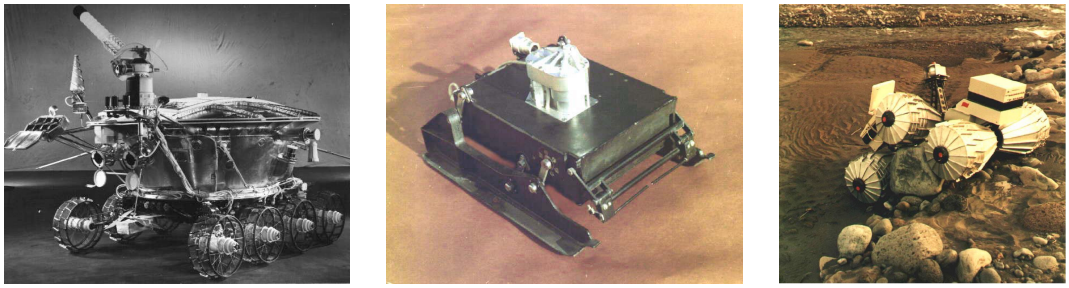

(a) **Lunokhod 1** (b) **PrOP-M** (c) **Marsokhod**

Figure 2.2: **Soviet rovers with other locomotion systems (taken from [8–10])**

Additional types of locomotion systems have been investigated in research and academia. These include crawling and hopping robots, tracked vehicles and rovers with walking capabilities [11–14]. Walking in particular offers advantages when negotiating obstacles and slopes, but is generally less efficient on flat terrain and complex to implement in terms of hardware and control.

2.1.2 The ExoMars Rover

ESA's ExoMars rover, shown in Figure 2.3 and to be launched in 2020, will be the first rover on Mars without a rocker-bogie suspension design. Through several studies [15–18], a six-wheel triple-bogie suspension layout was selected for the rover, shown in Figure 2.4. Compared to the rocker-bogie suspension, this layout offers advantages in terms of stowage, weight and complexity of the mechanical design while offering similar stability

performance and being passively compliant [19]. All six wheels are steerable, enabling a crab-like sideways motion for precise body positioning during experiments. Due to lander volume constraints, the wheels of the ExoMars rover are relatively small in diameter and width, leading to a high effective ground pressure. This is somewhat compensated by an inherent flexibility of the metallic wheels, increasing the size of the contact patch and thus the tractive performance compared to a wheel of equal size.

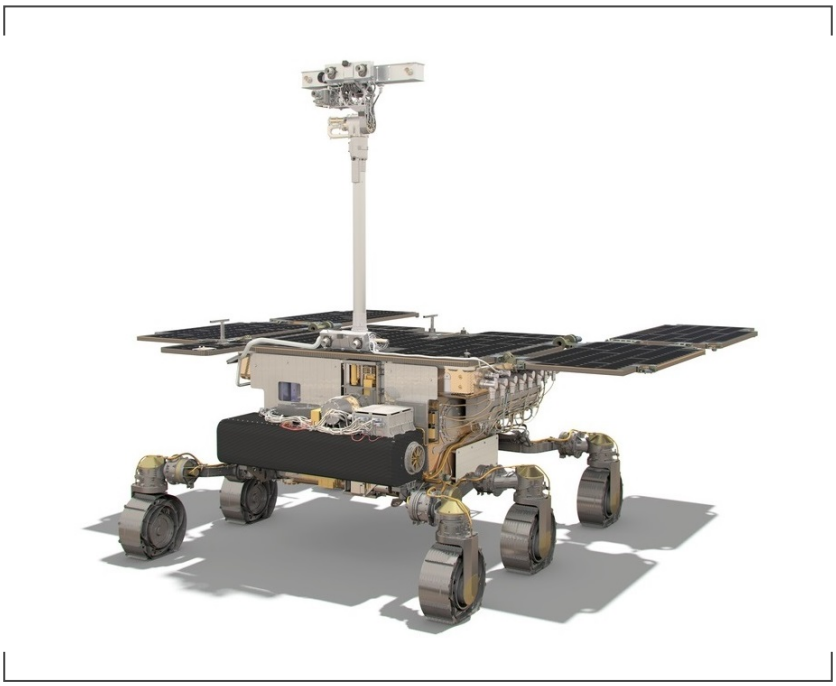

Figure 2.3: **ESA's ExoMars rover (rendering taken from [20])**

For deployment of the stowed wheels after landing, the ExoMars locomotion system additionally features actuated joints to rotate each leg assembly, making it an articulated suspension design. This offers the possibility of using these joints for active body pose adjustment and for introducing a so-called Wheel Walking locomotion mode, where the wheels are moved longitudinally backwards and forwards with respect to the rover body to increase the overall body traction. The current status of the design of the ExoMars mobility subsystem is described in [21, 22].

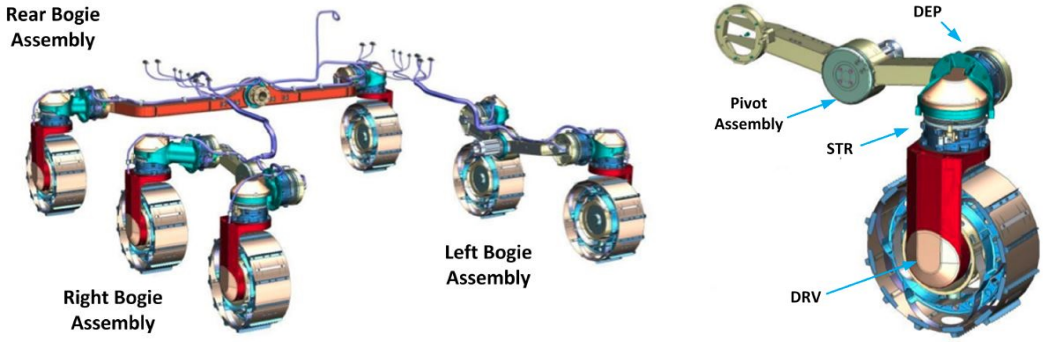

(a) **Triple-bogie suspension design** (b) **Front bogie assembly**

Figure 2.4: **Locomotion system of the ExoMars rover (taken from [22])**

2.1.3 Wheel Walking

Wheel Walking is a proposed hybrid locomotion mode for planetary rovers with articulated suspension. It aims to introduce some of the advantages of true walking locomotion to wheeled locomotion systems, which are generally less complex and more efficient on flat terrain, but lack in traversability performance on soft soils and steep slopes. Wheel Walking can be described as a longitudinal motion of the rolling wheels with respect to the rover body in a sequence called a gait. While some wheels remain stationary relative to the terrain, the others are moved forward while keeping contact with the ground. In soft soils, the stationary wheels provide an anchoring mechanism while the tractive effort needed to propel the moving wheels forward is decreased. The intended effect is an increase of overall body traction, measured as drawbar pull for planetary rovers.

Research on Wheel Walking locomotion for planetary rovers goes back to the 1970s, when it was investigated through the Soviet mock-up KIIIM (see Figure 2.5a), which was based on the wheel and suspension design of Lunokhod 1, followed by the EOSAIII-1 mock-up (see Figure 2.5b), which was additionally capable of body pose adjustments. For the KIIIM vehicle, Wheel Walking increased its slope gradeability from 18° to 34° [10]. In the 1990s, Wheel Walking was incorporated as well in the Marsokhod design, where the wheels were grouped in three units, allowing a peristaltic worm-like back-and-forth movement [4] (see Figure 2.5c). The most recent implementation for this type of rover was done by [23].

In literature, Wheel Walking is also known as inching, rolking or push-pull locomotion [26, 27]. Initially, the idea of an all-terrain vehicle with push-pull locomotion was presented

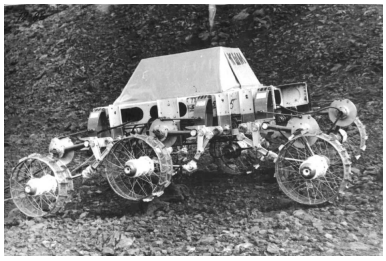

(a) **KIIIM mock-up**

(b) **EOSAIII-1 mock-up**

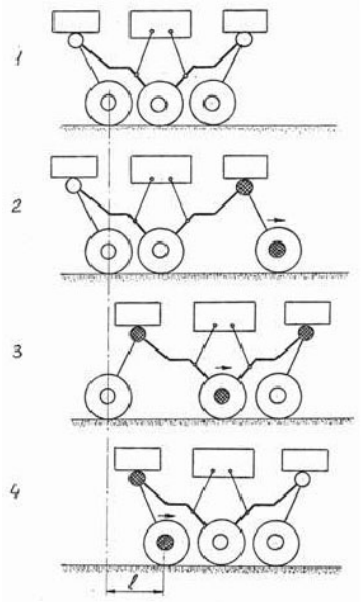

(c) **Marsokhod Wheel Walking scheme**

Figure 2.5: **Wheel Walking on Soviet rovers (taken from [24, 25])**

in 1961 by von Sybel and Große-Scharmann [28], including theoretical and experimental analysis on wheel-soil interaction for this locomotion mode. In 1963, Czako et al. introduced a concept of a segmented vehicle with the ability to inch [29]. Much more recently in 2011, Moreland et al. focused on the advantages of inching using the Scarab roving vehicle [30]. Tests on a single-wheel test bed showed that the tractive advantages of this type of locomotion mode stem from the difference in soil response below the stationary and the rolling wheel. Under the stationary wheel, the soil is pressed together to form a unified mass that supports the wheel without significant shear displacement, whereas under the rolling wheel the soil is constantly transported along the rim with varying direction of flow velocity. Using the same vehicle, the benefits of inching locomotion for extrication from sand entrapment situations were shown [26]. This is especially relevant in the context of NASAs Spirit rover, which had to be abandoned on Mars in 2010 after its wheels became deeply embedded in soft soil [1]. Another recent research robot implementing inching locomotion is the Sherpa robot developed by DFKI [31].

The ExoMars rover will be the first launched planetary rover featuring a suspension layout designed with Wheel Walking in mind [19]. Each of its six wheel-leg assemblies is

attached to an actuated deployment joint (DEP, see Figure 2.4b) used to unfold the legs and bring them to their nominal position after landing on Mars. These additional joints enable the implementation of Wheel Walking locomotion by swiveling the legs backwards and forwards in a coordinated pattern, with the aim of increasing the rover's traversability envelope for steep slopes and soft soils. Based on the current design of the flight rover, the implemented patterns (gaits) will be constrained by the possible swivel range of the legs (see Figure 2.6 for an approximate illustration) and the maximum velocity of the deployment actuators. Due to the suspension layout of the ExoMars rover, during Wheel Walking operation, no steering operation is possible. Thus, the Wheel Walking mode is not intended as a regular driving mode, but rather to be used in extreme situations where additional traction is needed to climb steeper slopes or to escape entrapment situations.

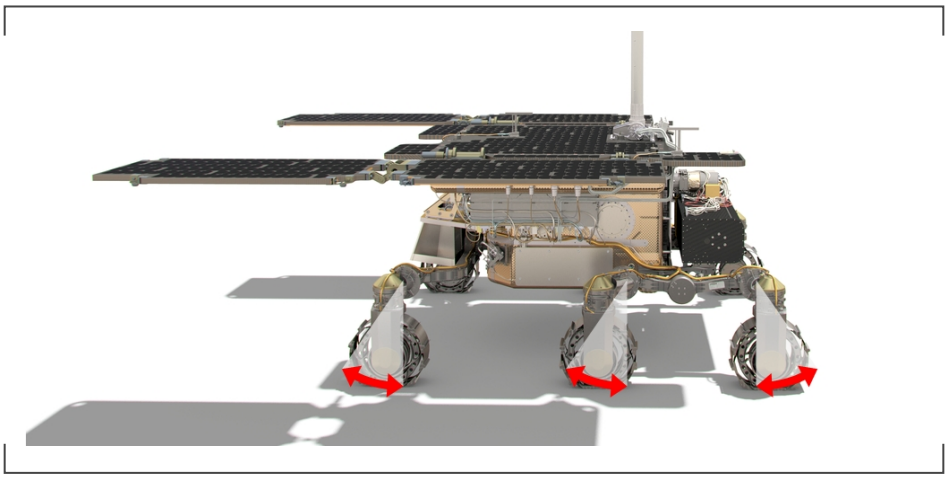

Figure 2.6: **ExoMars rover leg swivel range (image taken from [32])**

Initial investigations in the implementation of Wheel Walking for the ExoMars rover were performed by Azkarate et al. using ESA's scaled-down laboratory prototype ExoTeR [33]. Its locomotion configuration is based on the early RCL-E design proposal for the ExoMars rover [19] and does not feature flexible wheels. The author of this thesis was involved in these investigations, implementing the algorithm performing the Wheel Walking motion. During this project, several basic gaits were defined and initial experiments on slip performance on slopes were carried out, showing clear advantages of Wheel Walking over Normal Driving.

2.2 Kinematic Modeling

To control the motion of a rover, commands for joint actuation need to be generated. In the simplest case, these can be determined from basic geometrical considerations. For a non-articulated rover with six wheels driving on flat ground, driving modes like Ackermann steering [34] can be used to compute steering angles and wheel speeds in order to achieve a certain body speed and turn radius. However, for robots driving in rough terrain with a complex suspension arrangement, these basic 2D driving modes lead to oversimplifications that can degrade the driving performance. Additionally, for articulated rover suspensions with an increased number of joints, more complex models are required to make use the additional degrees of freedom.

A standard approach to tackle this task is the derivation of a kinematic model that relates rover body speeds to joint rates based on the current joint configuration. This is a well-known problem for robotic manipulators, where the joint rates required to achieve a desired end-effector velocity need to be determined. There, the end-effector velocities are related to the manipulator joint rates through the manipulator Jacobian matrix [35]. This approach was originally extended by Muir and Neuman for wheeled mobile robots (WMR) [36]. The kinematic configuration of such a robot can be split into kinematic chains, with one kinematic chain per wheel. For each such kinematic chain, a wheel Jacobian can be found, relating the velocities at the wheel-ground contact point (the "end-effector") to the joint rates of the chain and the velocities of the rover body frame (the origin of the chain). These wheel Jacobians can be fused into a single representation which can be solved for the desired actuation quantities. In general, this approach is viable for rovers with velocity-controlled joints under the assumption of rigid wheels with a single point of contact with the ground.

The method followed in this thesis is based mainly on the work of Tarokh et al. [37–40] which builds on [36] to develop a systematic approach for WMR kinematic modeling for rough-terrain locomotion including slip kinematics. It is based on the representation of the robot's kinematic configuration as chains of joints and linkages through Denavit-Hartenberg parameters [35]. Their most recent publication [40] employs velocity propagation to compute the wheel Jacobian and includes null-space projection for constrained optimization of an objective function. If the robots joint configuration is kinematically redundant, this allows to introduce lower-priority sub-tasks like adjustment of the rover body pose while still fulfilling the desired body velocity and joint rate constraints. In [40], an objective function is specifically defined to enhance tip-over stability of an articulated robot. A similar objective is pursued by Iagnemma et al. [41] who also tackle the problem of contact angle estimation [42] through geometric considerations. The wheel-terrain contact

angle is a required quantity in the kinematic chain that defines the rover configuration. An alternative visual approach for this is presented in [43]. The methods by Tarokh et al. were applied in the past for systems like [44] and [45]. Similar approaches were formulated by other authors, e.g. [46] and [47]. Based on this, the latter also introduce a method for body-level slip prediction.

3 The EXM-BB2 Rover

The EXM-BB2 rover (shown in Figure 3.1 in its current configuration) was initially designed and built in 2009 as a test platform based on the ExoMars mobility subsystem during phase B2. It was used during a test campaign to assess traversability performance of the platform on soft, Mars-like soils and to verify the original requirements [48]. The platform is central to this thesis, as the developed algorithms were implemented for and tested on this specific system. This chapter is therefore dedicated to a thorough description of the system – its design, its components and its sensors. Its electronics were heavily modified and additional sensors were installed in preparation for this thesis. A substantial amount of time was spent on their integration and configuration, which led to a detailed understanding of the system.

Figure 3.1: **The EXM-BB2 rover**

3.1 Mechanical Design

Table 3.1: **Main geometrical specifications**

Property	Value
Track Width	1200 mm
Front to Center Axle	640 mm
Center to Rear Axle	720 mm
Wheel Diameter	250 mm
Wheel Width	110 mm
Grouser Height (center)	9 mm
Grousers per Wheel	12

3.1.1 Suspension

The rover features the same six-wheel triple-bogie articulated suspension design as the ExoMars rover at a scale of 1:1, with three wheels on both sides. Table 3.1 lists the main geometric dimensions for suspension and wheels. Each wheel is part of a leg assembly connected to a passive bogie for terrain adaptability. Two bogies are attached on the sides of the rover and one in the back, each supporting two leg assemblies at each end. At the connection point between the bogie and the leg assembly sits the walking joint which allows the assembly to be pivoted, mainly intended for deployment after landing. Each assembly can be rotated forwards and backwards, in contrast to the flight rover, where the front wheels are limited to forward motion and the center and back wheels are limited to backward motion (see Figure 2.6). Additionally, each leg contains a steering joint, which allows each wheel to be pointed in an arbitrary direction, i.e. to align it with the local driving direction. Each wheel can be rotated around its hub axis (the driving joint) to move along the local terrain. Figure 3.2 shows the rear-right leg assembly with labeled joints. In total, the rover has 18 active and three passive joints, making it a system with a large number of degrees of freedom and interesting control capabilities.

3.1.2 Wheels

The wheel design itself is also based on the design of the ExoMars rover wheels. They are made from aluminium, with a thin, cylindrical outer sheath as the driving surface, open sides, leaf springs on the inside as a support structure and bump stops to prevent

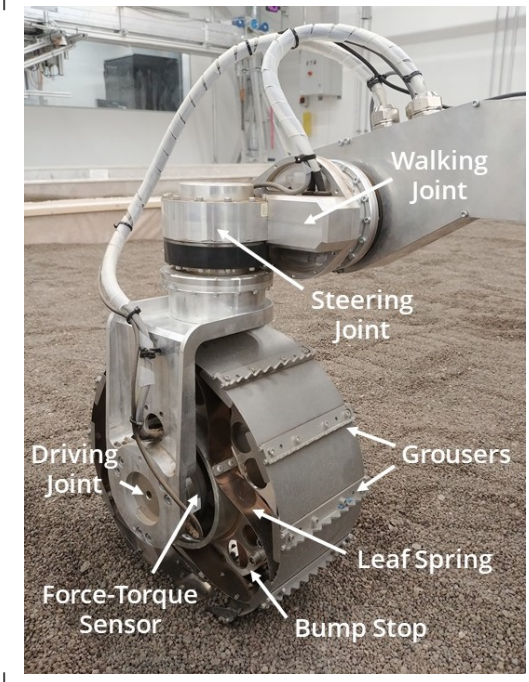

Figure 3.2: **EXM-BB2 right-rear leg assembly**

excessive deflection (see Figure 3.2). At a diameter of 0.250 m, the wheels are relatively small, leading to a high effective ground pressure. To compensate for this, they were designed to be inherently flexible, thus having a larger footprint while driving, leading to less sinkage. Since rolling friction on a smooth metal surface is low, 12 grousers are mounted on the outer surface of the wheels at equal spacing. They are meant to dig into the soil and provide extra grip and support by providing a surface perpendicular to the driving direction.

3.1.3 Chassis

Even though the geometrical properties of the suspension system as well as the design of the wheels are similar to the ExoMars rover, the rest of the platform is not. It was built to serve as a test platform for the verification of the mobility subsystem and is thus subject to different constraints. No space grade components are used. The chassis is built from aluminium profiles, making it cheap and easy to adapt. The suspension parts are built from aluminium as well, with no specific emphasis placed on weight reduction. Additionally, for

each active joint, the suspension allows the installation of a force-torque sensor for data acquisition, which are not present in the real system.

Originally, the platform was equipped with a tower made out of aluminium profiles, mounted on top of the chassis. This tower contained the power electronics components, with the batteries mounted at a height to simulate the center of gravity (CoG) location of the flight rover. This has meanwhile been replaced with a lower inner tower for easier handling, carrying the power electronics as well as the on-board PC, and a lower and wider outer box structure, on which the new motor controllers are mounted. As a result of this, the CoG is now below the CoG of the flight rover.

3.1.4 Weight Distribution

Table 3.2: **Comparison of rover weight distribution on flat ground**

Rover	FR	CR	RR	RL	CL	FL	Total
ExoMars (Mars)	176 N	176 N	208 N	208 N	177 N	178 N	1123 N
EXM-BB2 (Earth)	190 N	176 N	209 N	204 N	177 N	198 N	1153 N

Wheel traction is dependent on the normal force acting at the wheel-ground contact point caused by the rover weight and CoG position. Overall, by being reduced to the components needed for the locomotion system, the platform weighs approximately one third of the flight rover. This allows for accurate testing on earth, since gravity here is about three times that of Mars, meaning that the effective ground pressure levels of the flight rover on Mars are similar to the ones of the EXM-BB2 rover on earth.

Additionally, the specific weight distribution on the wheels was recorded after all components were installed right before the beginning of testing. It was measured in a leveled position (0° pitch and roll) by lowering the rover onto industrial scales placed beneath the individual wheels on flat ground. These measurements were repeated three times and the results were averaged. Due to internal forces in the system, measurements varied significantly, so these results should just give an indication of the true weight distribution in comparison with the flight rover.

3.2 Electronics

In preparation for this thesis, the rover was equipped with a new stack of control electronics components to upgrade the platform and bring it in line with other systems currently in use at DLR, like the LRU rover [49]. This brings the advantage of available in-house domain knowledge for installation and troubleshooting as well as the re-usability of already available software components. Nevertheless, a large amount of work was needed for setup and integration. The system had to be reconfigured from the ground up.

3.2.1 Motors & Gearboxes

Table 3.3: **Motor specifications**

Property	Value
Nominal Voltage	48 V
Nominal Speed	8660 rpm
Nominal Torque	27.8 mNm
Nominal Current	637 mA

The walking, steering and driving joints are actuated by brushed DC electric motors with a high reduction rate through the attached gearbox assembly, leading to high torques at slow joint speeds. Table 3.3 lists the motor specifications. The walking and steering joints contain a worm gear followed by a harmonic drive gear, whereas the driving joints contain a planetary gear head before the harmonic drive. The gear ratios are listed in Table 3.4. All motor/gearbox assemblies are sealed for dust protection.

Table 3.4: **Gearbox reduction ratios**

Joint Type	Gearbox 1	Ratio 1	Gearbox 2	Ratio 2	Total Ratio
Walking	Worm Gear	1:38	Harmonic Drive	1:101	1:3838
Steering	Worm Gear	1:12	Harmonic Drive	1:101	1:1212
Driving	Planetary Gear	1:19	Harmonic Drive	1:101	1:1919

3.2.2 Motor Controllers

Previously installed motor controllers were replaced by Elmo DC Gold Whistle drives, one for each of the 18 actuated joints. The controllers allow for position, velocity and torque control, based on the data of the connected rotary encoders and the current flow. For the steering and walking joints, potentiometers are installed on each axis and read out by the motor controllers to allow for an absolute zero-positioning (homing) of the joints. This is not needed for the driving joints. Three of the six driving joint controllers are used to read out the potentiometers of the passive bogie joints. Two other driving joint controllers are used to read out the voltage and current levels of the power supply which is powering the motor controllers separately. The controllers (and therefore the motors) are powered at a voltage of 28 to 32 V. They are interconnected through an EtherCAT bus with a line topology which ends at the on-board PC which is also part of the bus.

3.2.3 Sensors

Potentiometers

The rover is equipped with potentiometers on the walking, steering and bogie axes to measure their absolute position. For the walking and steering axes, this is only needed for an initial position measurement, since the relative positioning can be measured more accurately through the less noisy motor encoders. For the bogie axes, the potentiometers are the only position data source. Transformation from the bogie potentiometer values to an angular position is performed in the Rover Interface component of the software stack (see Section 3.3.3) by applying a linear conversion factor and a zero offset. A linearity analysis for the bogie potentiometers showed a sufficient linearity in the normal operating range (see Figure 3.3) with a conversion factor of 30.5 $\frac{^\circ}{\text{mV}}$ (negative for the front-left bogie). Zero offsets for the bogie potentiometers are listed in Table 3.5. To compute the joint velocity of the bogie joints, the (filtered) discrete derivative of the position estimate is taken.

Table 3.5: **Bogie potentiometers zero offset**

Bogie	Zero Offset
Front-Right	5440 mV
Rear	2835 mV
Front-Left	5400 mV

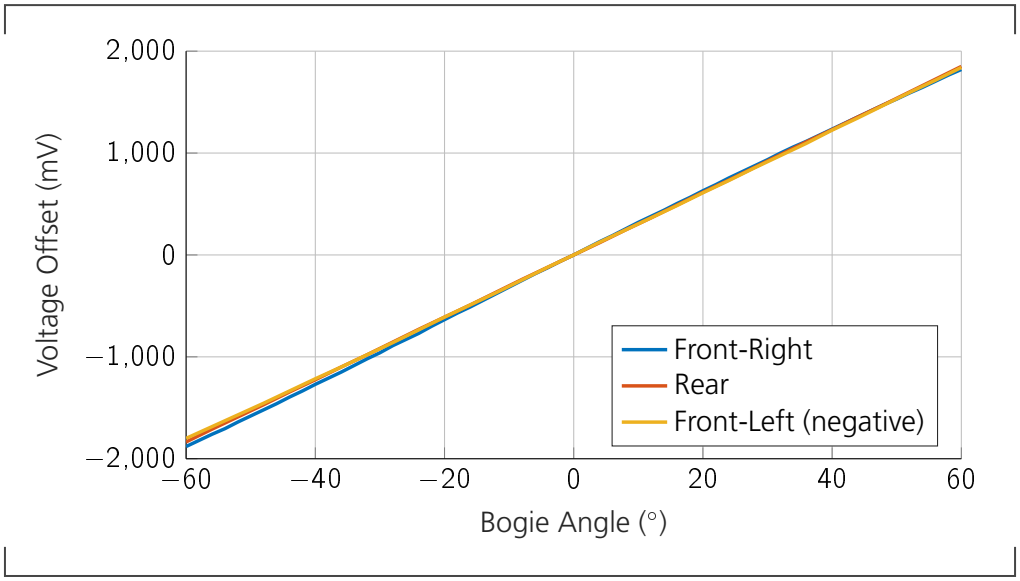

Figure 3.3: **Bogie potentiometer linearity analysis**

Inertial Measurement Unit

Table 3.6: **IMU specifications [50]**

Property	Value
Angular Resolution	0.05°
Repeatability	0.02°
Static Accuracy (roll/pitch)	0.5°
Static Accuracy (yaw)	1.0°

An inertial measurement unit (IMU) is installed on the rover to measure linear accelerations, rotation rates and absolute orientation based on a magnetometer. Its specifications are listed in Table 3.6. The IMU is installed laterally at the center of the rover body and longitudinally/vertically on top of the front chassis cross-beam (see Figure 3.4), with the direction of the IMU-frame axes coinciding with the ones of the rover reference frame (see Section 4.1.1). The orientation is output as a quaternion $\mathbf{q} = [q_0, q_1, q_2, q_3]^T$ with its zero value coinciding with a coordinate frame where x points towards magnetic north, z points towards the ground and y completes a right-handed coordinate system. The rover roll Φ, pitch Θ and yaw Ψ angles are computed from this quaternion according to the XYZ euler convention as [50]

$$\begin{bmatrix} \Phi \\ \Theta \\ \Psi \end{bmatrix} = \begin{bmatrix} \arctan2(2q_0q_1 + 2q_2q_3), 2q_0^2 + 2q_3^2 - 1) \\ -\arcsin(2q_1q_3 - 2q_0q_2)) \\ \arctan2(2q_0q_3 + 2q_1q_2), 2q_0^2 + 2q_1^2 - 1) \end{bmatrix} \tag{3.1}$$

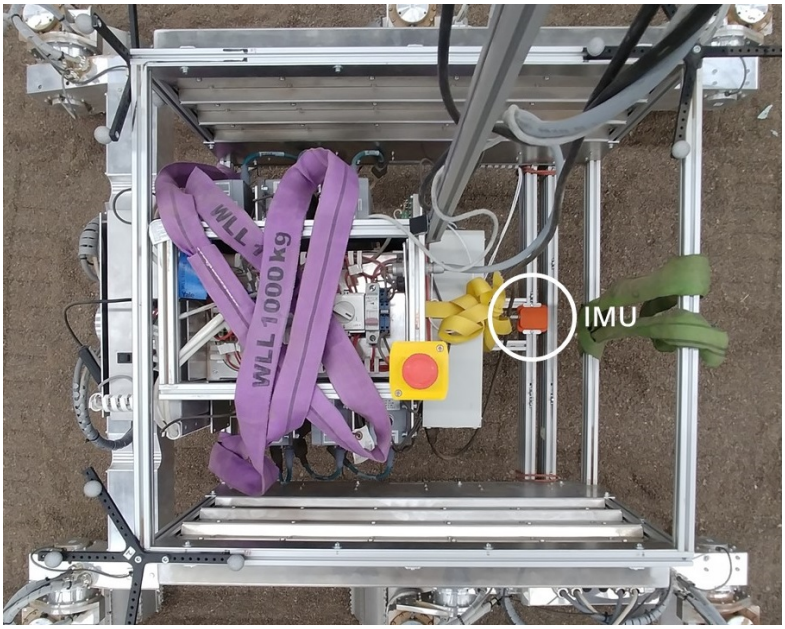

Figure 3.4: **IMU placement on front chassis cross-beam**

Force-Torque Sensors

Table 3.7: **FTS specifications**

Axes	Sensing Range	Resolution
f_x, f_y	± 1000 N	0.19 N
f_z	± 2000 N	0.28 N
τ_x, τ_y	± 50 Nm	0.008 Nm
τ_z	± 50 Nm	0.007 Nm

The suspension design of the EXM-BB2 rover offers interfaces for the installation of force-torque sensors (FTS) at the walking, steering and driving joints. In places where no sensor is installed, dummy sensors are mounted instead. The sensors are mounted on the inner

chassis-side of the joints and do not rotate with the outer part. For this thesis, one sensor was installed on each driving joint axis (see Figure 3.2), mounted at an offset of 51 mm from the wheel center plane. This offset is accounted for in the sensor software to move the virtual measurement origin to this point. For consistency of measurements on rover level, the FTS coordinate frames on the left side of the rover were rotated in software by 180° around their x-axis. When all joints are in their nominal position, forces in x-direction are measured in the wheel center plane parallel to the rover reference frame z-axis, forces in y-direction are measured parallel to the reference frame x-axis and forces in z-direction are measured parallel to the reference frame y-axis. The sensors were calibrated shortly before the test campaign. Their specifications are listed in Table 3.7. Their data is used for the measurement of wheel-terrain contact forces and contact angle estimation (see Section 4.1.2).

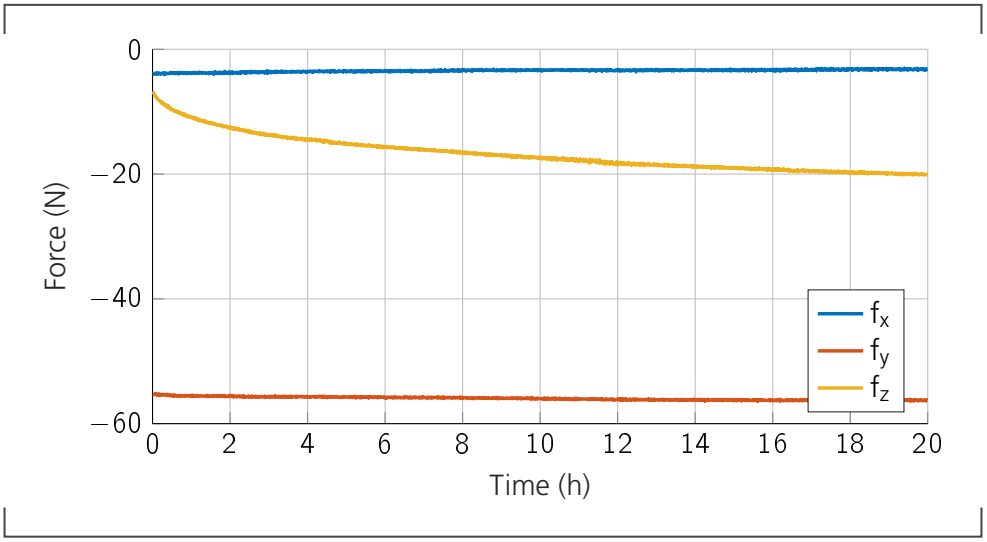

Figure 3.5: **FTS measurement drift after switch-on**

The force-torque sensors are subject to a significant amount of measurement drift while warming up. To assess this behavior, a long term drift analysis was undertaken by recording the measurements of an unloaded sensor over a period of 20 hours after power on. The results can be seen in Figure 3.5. Even after 20 hours, the values have not reached a steady state. Nevertheless, since the variation of the f_x and f_y values over the measurement period is less than 1 N and thus less than 0.1% of the rover weight, it can be neglected and no warm-up period is necessary if only measurements along these axes are of interest – which is the case here. The f_z measurements behave significantly worse with a variation of over 15 N over 20 hours and thus more than 1% of the rover weight. Between two measurements of the same load after warm-up over multiple days in the same environment, no significant differences were noted.

Additionally to sensor drift, each sensor is subject to measurement bias where values are measured even though no forces are applied. Before the test campaign, these biases were recorded for each sensor while installed on the rover with dismounted wheels and corrected via software.

3.2.4 On-Board PC

The communication with the motor controllers, read-out of sensor data as well as the execution of higher-level control models to compute motor controller commands is performed by an on-board PC with a quad-core Intel Core i7 desktop CPU. It is running a 64 bit Linux system with real-time kernel patch (PREEMPT-RT). It is powered separately from the motor controllers by an external power supply. Communication with the system is possible via Ethernet.

3.3 Software Stack

The rover's on-board PC runs a whole host of modules necessary to communicate with components and to compute commands. This includes drivers for IMU and gamepad, capture of UDP data from the force-torque sensors, communication with the motor controllers via EtherCAT and the higher level control models making use of this data to generate new motor controller commands. The modules are interconnected via two frameworks developed internally at DLR: Robotkernel and Links and Nodes [51, 52].

3.3.1 Robotkernel

Robotkernel (RK) is a runtime-configurable hardware abstraction framework that provides cross-platform device driver modules with generic hardware interfaces. It facilitates an easy reuse of already existing modules and makes it possible to access the device data output as a published Links and Nodes topic. It provides an EtherCAT Master module for communication with the motion controllers as well as modules for data acquisition from Gamepad, IMU and force-torque sensors. For the motion controllers, Robotkernel sets limit values on motor current and joint speeds. It also provides a mapping between radians and encoder steps for joint commands/measurements. Communication with the motor controllers runs at 1000 Hz.

3.3.2 Links and Nodes

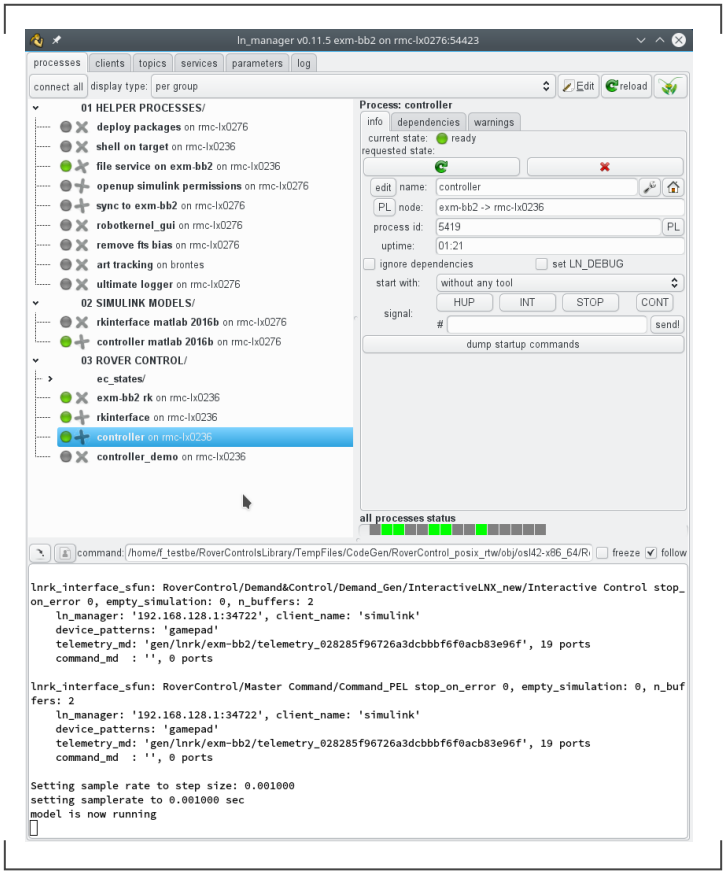

Figure 3.6: **LN Manager GUI**

Links and Nodes (LN) is DLR's internal robot middleware. It can be compared to similar frameworks like ROS and Rock. It works on the basis of modules which are interconnected through LN via published message topics or as services. Modules are deployed locally or on other nodes in the network via the LN Manager and can subscribe to topics of other running modules, independent of system boundaries. Inter-process communication is real-time capable. The LN Manager provides an overview of the current status of the modules and allows to specify module interdependencies so that a whole network of modules can be started at once. It additionally provides functionality for module configuration via GUI parameters and logging capabilities for published topics. Modules can be written in C++ or Python or can be created in Simulink and compiled as real-time target binaries.

3.3.3 Rover Interface

As a layer between modules for higher level control and the communication with the hardware components through Robotkernel, a rover interface module was created in Simulink. It acts as an intermediary to provide a clean interface to higher level modules and to perform rover initialization and safety tasks. It processes and reorganizes the data to make it consistent regarding coordinate frames, units and naming, creates commands for the motion controllers from higher level joint commands, determines the joint position zero offset at power up, performs the homing procedure and enforces safety limits on the joint speeds and positions. It is run at 1000 Hz, triggered by the arrival of new measurements from the motor controllers.

4 Kinematic Modeling and Implementation

For the implementation of rough-terrain locomotion modes for a rover with a large number of degrees of freedom, it is desirable to derive a universal kinematic model relating rover body speeds to rover joint rates. Locomotion modes can then be implemented by specifying known and unknown quantities and solving the system of equations accordingly, with optional joint weighting and the introduction of lower-priority sub-tasks.

This chapter presents the kinematic modeling approach taken in this thesis and its application to the EXM-BB2 rover. It explains the basic ideas, equations and steps needed to derive the model as well as the properties of the solution and the handling of kinematic redundancies. Afterwards, the implementation of two rough-terrain locomotion modes is discussed: Balancing, a mode aimed at increasing tip-over stability and reducing body tilt, and Wheel Walking, a mode aimed at improving terrain traversability and increasing safety margins on soft soils.

4.1 Kinematic Modeling for EXM-BB2

The modeling approach applied to the EXM-BB2 rover in this thesis is mainly based on the method published by Tarokh et al. in 2013 [40], which in turn is based on several earlier publications by the same authors [37–39] and initially on the work [36] by Muir and Neuman. It is applicable to any wheeled rover with an articulated suspension that can be broken up into chains of single degree of freedom (DoF) joints and linkages.

The method is based on the propagation of velocities from the rover reference frame to the wheel-terrain contact point for each kinematic chain (with one chain per wheel) and the fusion of the resulting equations into one system relating rover body speeds to rover joint rates. To make the method systematically applicable, it makes use of a Denavit-Hartenberg formulation for describing the transformations between consecutive joint co-

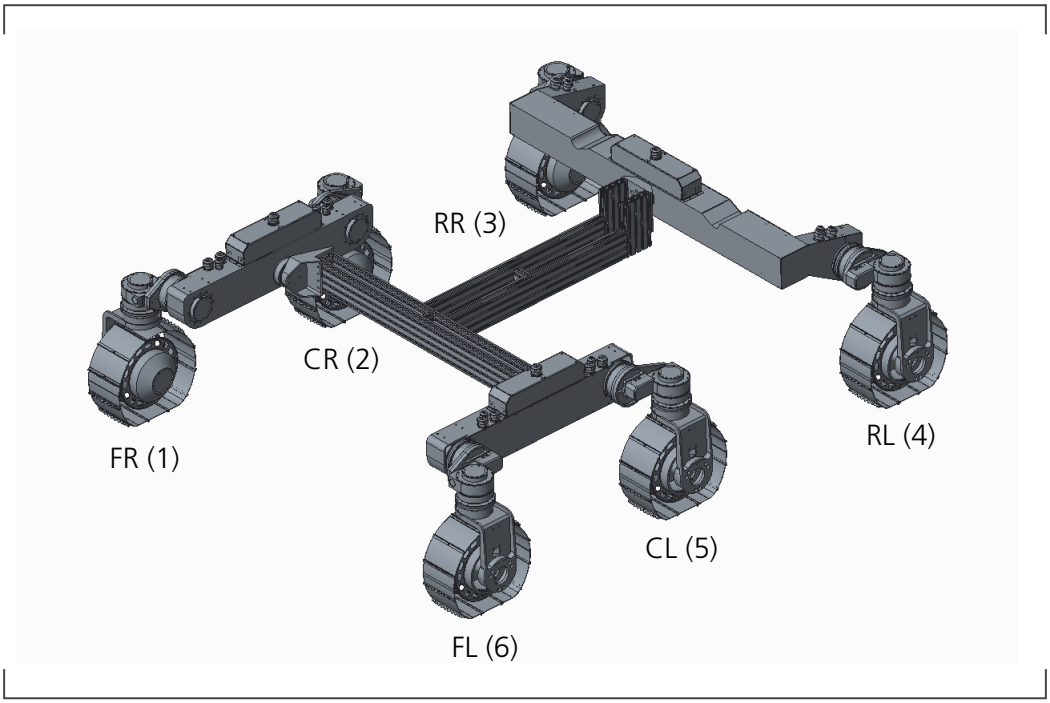

Figure 4.1: **3D view and kinematic chains of the EXM-BB2 suspension**

Table 4.1: **Kinematic Chains**

Chain	Label	j
Front-right	FR	1
Center-right	CR	2
Rear-right	RR	3
Rear-left	RL	4
Center-left	CL	5
Front-left	FL	6

ordinate frames. After reordering the system of equations according to the desired task, it can be solved for unknown rates by means of the pseudoinverse. The method additionally allows for a weighting of the joints and the utilization of kinematic redundancies through null-space projection. The approach is presented in detail in the following sections.

4.1.1 Denavit-Hartenberg Parameters

Denavit-Hartenberg parameters are a means to systematically attach coordinate frames to a chain of joints and linkages. Multiple definitions exist, with the proximal convention being used here [35]. Starting at the rover reference frame, coordinate frames with axes $(\boldsymbol{x}_i, \boldsymbol{y}_i, \boldsymbol{z}_i)$ and origin $\boldsymbol{o}_i$ are defined for each joint i in a chain, such that

- the $\boldsymbol{z}_i$ axis lies along the axis of motion of joint i
- the $\boldsymbol{x}_i$ axis is perpendicular to $\boldsymbol{z}_i$ and $\boldsymbol{z}_{i+1}$
- the origin $\boldsymbol{o}_i$ lies at the intersection between $\boldsymbol{x}_i$ and $\boldsymbol{z}_i$

The transformation between two consecutive frames with axes $(\boldsymbol{x}_{i-1}, \boldsymbol{y}_{i-1}, \boldsymbol{z}_{i-1})$ and $(\boldsymbol{x}_i, \boldsymbol{y}_i, \boldsymbol{z}_i)$ is then defined through four parameters:

- a_{i-1} is the distance from z_{i-1} to z_i measured along x_{i-1}
- α_{i-1} is the angle from z_{i-1} to z_i measured about x_{i-1}
- d_i is the distance from x_{i-1} to x_i measured along z_i
- θ_i is the angle from x_{i-1} to x_i measured about z_i

The parameter θ_i is variable for revolute joints.

For the EXM-BB2 rover, Denavit-Hartenberg (DH) parameters for six kinematic chains need to be determined, each starting at the rover reference frame and ending at the wheel-terrain contact point of one of the wheels. Figure 4.1 shows a 3D rendering of the EXM-BB2 suspension including chain labels, which are explained in Table 4.1. Figures 4.2, 4.3 and 4.4 show the overall placement of frames on the rover. Figure 4.5 specifically illustrates the frame placement at the end of the chain.

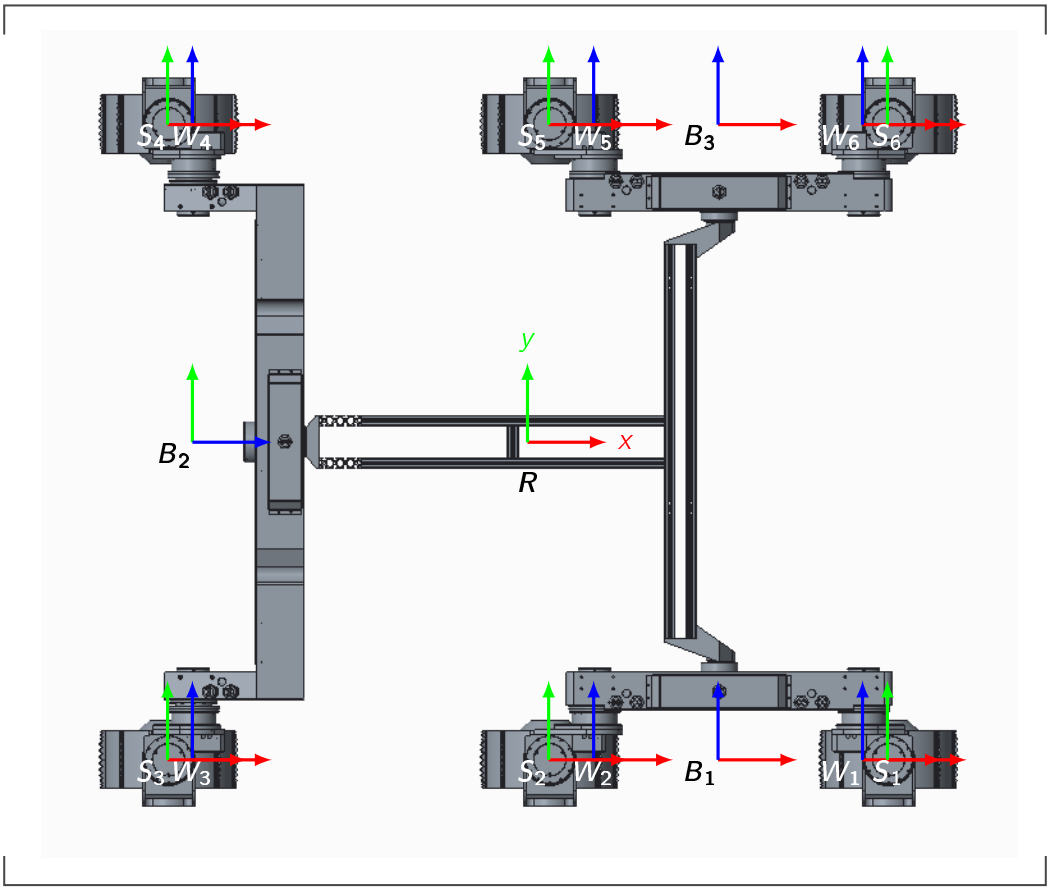

Figure 4.2: **Placement of frames for rover joints (top view)**

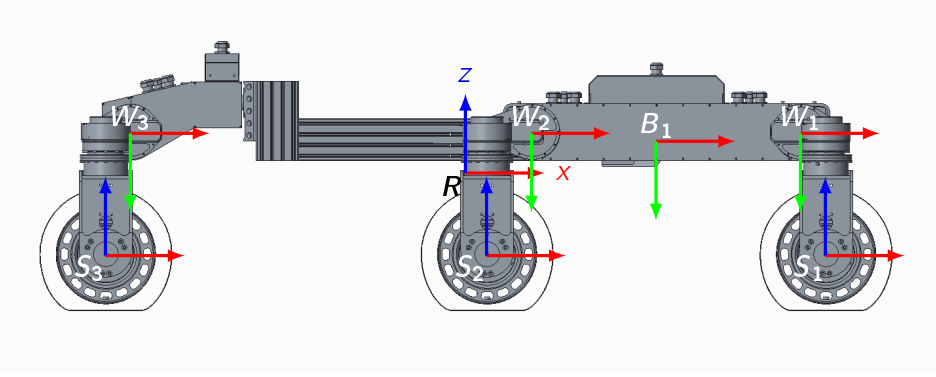

Figure 4.3: **Placement of frames for rover joints (side view)**

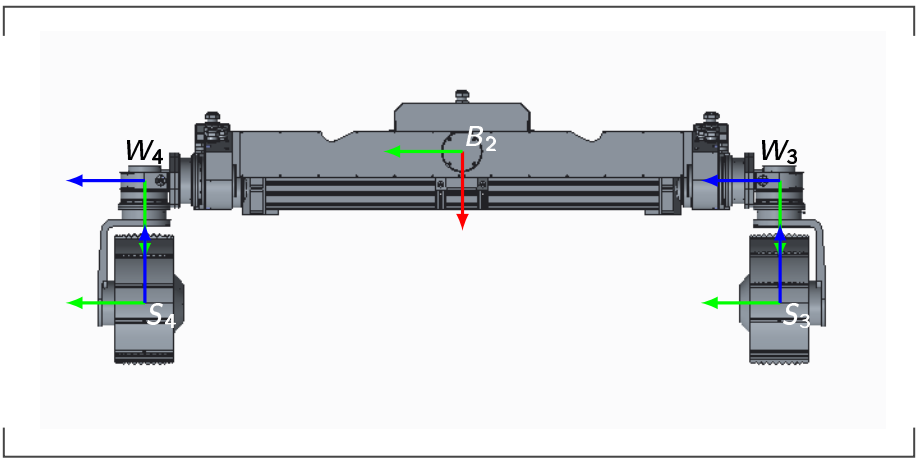

Figure 4.4: **Placement of frames for rover joints (rear view)**

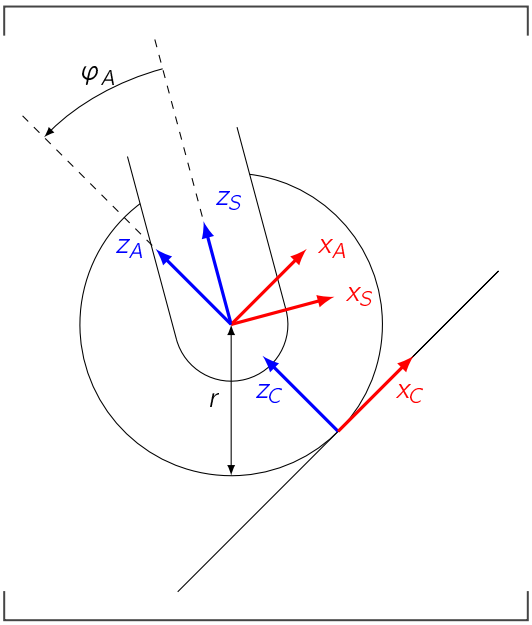

Figure 4.5: **Placement of frames at rover wheel**

Frame 0 in each chain corresponds to the rover reference frame R, centered between the left and right wheels and the front and back wheels, sitting right below the chassis' central beam, with its x-axis pointing forwards, its y-axis pointing left and its z-axis pointing upwards. The other frames are named according to the joint they are attached to and are consecutively numbered by their listing in the DH table:

- Frames B_{1-3} are attached to and rotating with the bogie joints
- Frames W_{1-6} are attached to and rotating with the walking joints
- Frames S_{1-6} are attached to and rotating with the steering joints
- Frames A_{1-6} are attached to the driving joint axis and are rotating with the contact angle so that the frame's y-axis is perpendicular to the ground

As in [40], at the end of each chain sits the frame C_{1-6} at the point of contact between wheel and terrain, with its x-axis parallel to the terrain and pointing forwards in nominal position, its y-axis pointing to the left and its z-axis perpendicular to the terrain and pointing towards the driving joint axis. This is under the assumption of a wheel as a rigid disc with only one point of contact on non-deformable terrain. Additionally, multiple non-rotating intermediary frames I_{1-6} are introduced to move from one joint to the next while keeping with the DH convention. Some frames are shared between multiple chains, for example at the bogie joints, where two wheels are attached to one bogie.

The chosen DH parameters are listed in Table 4.2 for all six kinematic chains. The table includes the name of the frame, the label of the chain it belongs to, the position i of the frame in the chain, the four DH parameters a_{i-1}, α_{i-1}, d_i and θ_i and the joint rate variable $\dot{\theta}_i$ for frames attached to movable (rotatory) joints. Table 4.3 lists the values of the constants used in Table 4.2 which are based on the physical dimensions of the rover.

In the following, frame indices will often be omitted for brevity if they are apparent from context.

Table 4.2: **Denavit-Hartenberg parameters for the EXM-BB2 rover**

Frame	Chain	i	a_{i-1}	α_{i-1}	d_i	θ_i	$\dot{\theta}_i$
I_1	FR/CR/CL/FL	1	l_1	0	l_2	0	0
I_2	RR/RL	1	0	0	l_3	$\frac{\pi}{2}$	0
B_1	FR/CR	2	0	$-\frac{\pi}{2}$	$-l_4$	φ_{B_1}	$\dot{\varphi}_{B_1}$
B_2	RR/RL	2	0	$\frac{\pi}{2}$	$-l_5$	$-\frac{\pi}{2}+\varphi_{B_2}$	$\dot{\varphi}_{B_2}$
B_3	CL/FL	2	0	$-\frac{\pi}{2}$	l_4	φ_{B_3}	$\dot{\varphi}_{B_3}$
I_3	FR	3	l_6	0	0	$-\frac{\pi}{2}$	0
I_4	CR	3	$-l_7$	0	0	$-\frac{\pi}{2}$	0
I_5	CL	3	$-l_7$	0	0	$-\frac{\pi}{2}$	0
I_6	FL	3	l_6	0	0	$-\frac{\pi}{2}$	0
W_1	FR	4	l_8	0	0	$\frac{\pi}{2}+\varphi_{W_1}$	$\dot{\varphi}_{W_1}$
W_2	CR	4	l_8	0	0	$\frac{\pi}{2}+\varphi_{W_2}$	$\dot{\varphi}_{W_2}$
W_3	RR	3	l_9	$-\frac{\pi}{2}$	$-l_4$	$-\frac{\pi}{2}+\varphi_{W_3}$	$\dot{\varphi}_{W_3}$
W_4	RL	3	l_9	$-\frac{\pi}{2}$	l_4	$-\frac{\pi}{2}+\varphi_{W_4}$	$\dot{\varphi}_{W_4}$
W_5	CL	4	l_8	0	0	$\frac{\pi}{2}+\varphi_{W_5}$	$\dot{\varphi}_{W_5}$
W_6	FL	4	l_8	0	0	$\frac{\pi}{2}+\varphi_{W_6}$	$\dot{\varphi}_{W_6}$
S_1	FR	5	l_{10}	$\frac{\pi}{2}$	$-l_{11}$	φ_{S_1}	$\dot{\varphi}_{S_1}$
S_2	CR	5	$-l_{12}$	$\frac{\pi}{2}$	$-l_{11}$	φ_{S_2}	$\dot{\varphi}_{S_2}$
S_3	RR	4	$-l_{10}$	$\frac{\pi}{2}$	$-l_{11}$	φ_{S_3}	$\dot{\varphi}_{S_3}$
S_4	RL	4	$-l_{10}$	$\frac{\pi}{2}$	$-l_{11}$	φ_{S_4}	$\dot{\varphi}_{S_4}$
S_5	CL	5	$-l_{12}$	$\frac{\pi}{2}$	$-l_{11}$	φ_{S_5}	$\dot{\varphi}_{S_5}$
S_6	FL	5	l_{10}	$\frac{\pi}{2}$	$-l_{11}$	φ_{S_6}	$\dot{\varphi}_{S_6}$
A_1	FR	6	0	$-\frac{\pi}{2}$	0	φ_{A_1}	$\dot{\varphi}_{A_1}$
A_2	CR	6	0	$-\frac{\pi}{2}$	0	φ_{A_2}	$\dot{\varphi}_{A_2}$
A_3	RR	5	0	$-\frac{\pi}{2}$	0	φ_{A_3}	$\dot{\varphi}_{A_3}$
A_4	RL	5	0	$-\frac{\pi}{2}$	0	φ_{A_4}	$\dot{\varphi}_{A_4}$
A_5	CL	6	0	$-\frac{\pi}{2}$	0	φ_{A_5}	$\dot{\varphi}_{A_5}$
A_6	FL	6	0	$-\frac{\pi}{2}$	0	φ_{A_6}	$\dot{\varphi}_{A_6}$
C_1	FR	7	0	$\frac{\pi}{2}$	$-r$	0	0
C_2	CR	7	0	$\frac{\pi}{2}$	$-r$	0	0
C_3	RR	6	0	$\frac{\pi}{2}$	$-r$	0	0
C_4	RL	6	0	$\frac{\pi}{2}$	$-r$	0	0
C_5	CL	7	0	$\frac{\pi}{2}$	$-r$	0	0
C_6	FL	7	0	$\frac{\pi}{2}$	$-r$	0	0

Table 4.3: **Rover constants of physical dimensions**

Constant	Value	Description
l_1	360 mm	Rover reference frame to front bogie (horizontal)
l_2	60 mm	Rover reference frame to front bogie (vertical)
l_3	130 mm	Rover reference frame to rear bogie (vertical)
l_4	600 mm	Rover center line to wheel center line
l_5	633 mm	Rover reference frame to rear walking axis (horizontal)
l_6	273 mm	Front bogie axis to front walking axis (horizontal)
l_7	235 mm	Front bogie axis to center walking axis (horizontal)
l_8	15 mm	Front bogie axis to front walking axis (vertical)
l_9	55 mm	Rear bogie axis to rear walking axis (vertical)
l_{10}	47 mm	Front/rear walking axis to front/rear steering axis (horizontal)
l_{11}	231 mm	Walking axis to driving axis (vertical, "leg length")
l_{12}	85 mm	Center walking axis to center steering axis (horizontal)
r	125 mm	Wheel radius

4.1.2 Contact Angle Estimation

For the EXM-BB2 rover, the joint position values φ_B, φ_W and φ_S can be measured by the potentiometers (for the bogie joints) or the motor encoders (for the walking and steering joints). The values φ_A of the contact angle, defined as the angle between the steering axis and the terrain perpendicular, need to be estimated by a different method.

Flat Terrain Assumption

A simple solution would be to assume the terrain to be locally flat and parallel to the rover body base plane (spanned by the x- and y-axis of the rover reference frame R. In this case, the terrain normal $\boldsymbol{n}$ is parallel to the rover reference frame z-axis:

$$\boldsymbol{n}^R = \begin{bmatrix} 0 \\ 0 \\ 1 \end{bmatrix} \tag{4.1}$$

and can be transformed into the steering frame S by applying the accumulated rotation matrix $\boldsymbol{R}_R^S$, which can be determined from the transformation matrices:

$$\boldsymbol{n}^S = \boldsymbol{R}_R^S \boldsymbol{n}^R = \begin{bmatrix} n_x^S \\ n_y^S \\ n_z^S \end{bmatrix} \tag{4.2}$$

The contact angle φ_A can now be calculated as the angle between the z-axis of the steering frame S and the terrain normal $\boldsymbol{n}^S$, projected onto the x-z-plane:

$$\varphi_{A,\text{est}} = \arctan\left(\frac{n_x^S}{n_z^S}\right) \tag{4.3}$$

However, this estimation might not be sufficiently accurate, especially if the rover is traveling in rough terrain. Therefore, a method was developed to estimate the contact angle from the force-torque sensors mounted on the wheel hubs.

Force-Torque Sensor Measurement

The rover is assumed to be sitting on the ground in a static equilibrium. A wheel is again assumed to be a rigid disc with one point of contact with the ground. Here, a force $\boldsymbol{f}$ is acting on a wheel to counteract the partial rover weight. This force $\boldsymbol{f} = [f_x, f_y, f_z]^T$ and the corresponding torque $\boldsymbol{\tau} = [\tau_x, \tau_y, \tau_z]^T$ can be measured through the force-torque sensor. Since we are interested in the contact angle measured in the wheel plane, the z-component of the force and the x- and y-components of the torque are ignored.

In this scenario, $\boldsymbol{f}$ can be split up into the two components $\boldsymbol{f}_X$ and $\boldsymbol{f}_Y$ measured along the respective axes of the sensor. It can also be split up into a normal force $\boldsymbol{f}_N$ perpendicular to the ground and a friction force $\boldsymbol{f}_F$ parallel to the ground. It is the angle δ from $\boldsymbol{f}_X$, which lies along the the z-axis of the steering frame, to $\boldsymbol{f}_N$ that is of interest. Figure 4.6 shows an illustration of the geometrical relationships.

The partial angle α from $\boldsymbol{f}_X$ to $\boldsymbol{f}$ can be computed as

$$\alpha = \arctan\frac{|\boldsymbol{f}_Y|}{|\boldsymbol{f}_X|} \tag{4.4}$$

The magnitude of $\boldsymbol{f}_F$ can be estimated from the torque measurement τ_z around the z-axis of the sensor as

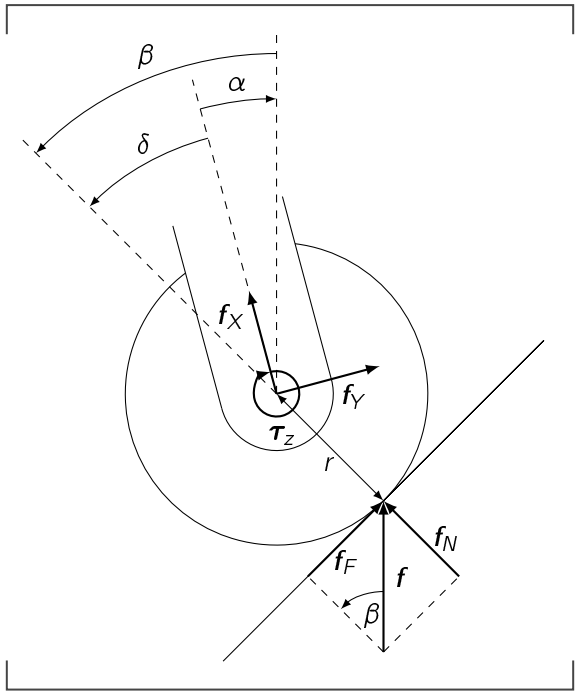

Figure 4.6: **Contact angle computation from FTS data**

$$|\boldsymbol{f}_F| = \frac{\tau_z}{r} \tag{4.5}$$

with r being the wheel radius. From this, the angle β from $\boldsymbol{f}$ to $\boldsymbol{f}_N$ can be computed as

$$\beta = \arcsin \frac{|\boldsymbol{f}_F|}{|\boldsymbol{f}|} = \arcsin \frac{\tau_z}{r|\boldsymbol{f}|} \tag{4.6}$$

Thus, the overall angle δ from $\boldsymbol{f}_X$ to $\boldsymbol{f}_N$ can be computed as

$$\delta = \alpha + \beta = \arctan \frac{|\boldsymbol{f}_Y|}{|\boldsymbol{f}_X|} + \arcsin \frac{\tau_z}{r|\boldsymbol{f}|} \tag{4.7}$$

This angle corresponds to the contact angle $\varphi_{A,\text{est}}$:

$$\varphi_{A,\text{est}} = \delta \tag{4.8}$$

4.1.3 Velocity Propagation

The following is based on the work of Tarokh et al. [40] and was adapted for the EXM-BB2 rover.

For each kinematic chain, a relationship between the motion of the rover body, the wheel and the joints in between needs to be established. The motion of the rover reference frame is expressed as its translational velocity $\mathbf{v}^0 = \mathbf{v}^R = [v_x^R, v_y^R, v_z^R]^T$ and rotational velocity $\boldsymbol{\omega}^0 = \boldsymbol{\omega}^R = [\omega_x^R, \omega_y^R, \omega_z^R]^T$. Using velocity propagation, these can be propagated along the kinematic chain from one frame to the next, with each subsequent frame adding some motion due to the rotation rate of its associated joint. The translational velocity of the current frame i is based on the translational and rotational velocity of the previous frame $i-1$ and can be written as

$$\boldsymbol{v}^i = \boldsymbol{R}_{i-1}^i \left(\boldsymbol{v}^{i-1} + \boldsymbol{\omega}^{i-1} \times \boldsymbol{p}_i^{i-1} \right) \tag{4.9}$$

under the assumption of having no translational joints. Here, $\boldsymbol{R}_{i-1}^i$ is the rotation matrix that rotates frame $i-1$ onto frame i. $\boldsymbol{p}_i^{i-1}$ is the vector of the origin of i expressed in coordinates of frame $i-1$. The rotational velocity of the current frame is based on the rotational velocity of the previous frame and the motion of the current frame and can be written as

$$\boldsymbol{\omega}^i = \boldsymbol{R}_{i-1}^i \boldsymbol{\omega}^{i-i} + \begin{bmatrix} 0 \\ 0 \\ \dot{\theta}_i \end{bmatrix} \tag{4.10}$$

under the assumption that the rotation of the joint corresponding to frame i occurs along the frame's z-axis, which is the case for the frame definition according to the Denavit-Hartenberg convention. The parameters of these equations can be extracted from the transformation matrices between two consecutive frames $i-1$ and i. This transformation matrix can be determined from the Denavit-Hartenberg parameters as follows:

$$\boldsymbol{T}_i^{i-1} = \begin{bmatrix} \cos(\theta_i) & -\sin(\theta_i) & 0 & a_{i-1} \\ \cos(\alpha_{i-1})\sin(\theta_i) & \cos(\alpha_{i-1})\cos(\theta_i) & -\sin(\alpha_{i-1}) & -\sin(\alpha_{i-1})d_i \\ \sin(\alpha_{i-1})\sin(\theta_i) & \sin(\alpha_{i-1})\cos(\theta_i) & \cos(\alpha_{i-1}) & \cos(\alpha_{i-1})d_i \\ 0 & 0 & 0 & 1 \end{bmatrix} \tag{4.11}$$

From this, the rotation matrix from frame i to frame $i-1$ can be extracted as

$$\boldsymbol{R}_i^{i-1} = \begin{bmatrix} \cos(\theta_i) & -\sin(\theta_i) & 0 \\ \cos(\alpha_{i-1})\sin(\theta_i) & \cos(\alpha_{i-1})\cos(\theta_i) & -\sin(\alpha_{i-1}) \\ \sin(\alpha_{i-1})\sin(\theta_i) & \sin(\alpha_{i-1})\cos(\theta_i) & \cos(\alpha_{i-1}) \end{bmatrix} \tag{4.12}$$

and thus the rotation matrix from frame $i-1$ to frame i needed for velocity propagation is given as its inverse

$$\boldsymbol{R}_{i-1}^{i} = \left(\boldsymbol{R}_i^{i-1}\right)^{-1} = \left(\boldsymbol{R}_i^{i-1}\right)^{T} = \begin{bmatrix} \cos(\theta_i) & \cos(\alpha_{i-1})\sin(\theta_i) & \sin(\alpha_{i-1})\sin(\theta_i) \\ -\sin(\theta_i) & \cos(\alpha_{i-1})\cos(\theta_i) & \sin(\alpha_{i-1})\cos(\theta_i) \\ 0 & -\sin(\alpha_{i-1}) & \cos(\alpha_{i-1}) \end{bmatrix} \tag{4.13}$$

The vector of the origin of frame i expressed in coordinates of frame $i-1$ can also be extracted from this transformation matrix as

$$\boldsymbol{p}_i^{i-1} = \begin{bmatrix} a_{i-1} \\ -\sin(\alpha_{i-1})d_i \\ \cos(\alpha_{i-1})d_i \end{bmatrix} \tag{4.14}$$

The cross product in (4.9) can be rewritten as

$$\boldsymbol{\omega}^{i-1} \times \boldsymbol{p}_i^{i-1} = \boldsymbol{\omega}^{i-1} \times \begin{bmatrix} a_{i-1} \\ -\sin(\alpha_{i-1})d_i \\ \cos(\alpha_{i-1})d_i \end{bmatrix} = \boldsymbol{S}_i^{i-1}\boldsymbol{\omega}^{i-1} \tag{4.15}$$

with the skew symmetric matrix

$$\boldsymbol{S}_i^{i-1} = \begin{bmatrix} 0 & \cos(\alpha_{i-1})d_i & \sin(\alpha_{i-1})d_i \\ -\cos(\alpha_{i-1})d_i & 0 & a_{i-1} \\ -\sin(\alpha_{i-1})d_i & -a_{i-1} & 0 \end{bmatrix} \tag{4.16}$$

Combining (4.9) and (4.10) with (4.15) leads to

$$\begin{bmatrix} \boldsymbol{v}^i \\ \boldsymbol{\omega}^i \end{bmatrix} = \begin{bmatrix} \boldsymbol{R}_{i-1}^i & \boldsymbol{R}_{i-1}^i \boldsymbol{S}_i^{i-1} \\ \boldsymbol{0}_{3\times 3} & \boldsymbol{R}_{i-1}^i \end{bmatrix} \begin{bmatrix} \boldsymbol{v}^{i-1} \\ \boldsymbol{\omega}^{i-1} \end{bmatrix} + \begin{bmatrix} \boldsymbol{0}_{5\times 1} \\ \dot{\theta}_i \end{bmatrix} \tag{4.17}$$

which can be written as

$$\begin{bmatrix} \boldsymbol{v}^i \\ \boldsymbol{\omega}^i \end{bmatrix} = \boldsymbol{A}_i \begin{bmatrix} \boldsymbol{v}^{i-1} \\ \boldsymbol{\omega}^{i-1} \end{bmatrix} + \boldsymbol{B}_i \dot{\theta}_i \tag{4.18}$$

Recursively applying (4.18) for a kinematic chain j starting from frame 0 (which is equivalent to frame R) until reaching frame C_j leads to the formulation

$$\begin{bmatrix} \boldsymbol{v}^{C_j} \\ \boldsymbol{\omega}^{C_j} \end{bmatrix} = \boldsymbol{D}_j \begin{bmatrix} \boldsymbol{v}^{R} \\ \boldsymbol{\omega}^{R} \end{bmatrix} + \boldsymbol{E}_j \dot{\boldsymbol{\varphi}} \tag{4.19}$$

relating the motion of the wheel contact frame to the motion of the rover reference frame and the joints in the chain. $\boldsymbol{D}_j$ is a 6×6 matrix, $\boldsymbol{E}_j$ is a 6×21 matrix and $\dot{\boldsymbol{\varphi}}$ is the 21×1 vector of joint rates for the bogie, walking and steering joints as well as the contact angles. If a joint is not part of the kinematic chain, its corresponding column in $\boldsymbol{E}_j$ contains only zeros. This is called the *contact kinematics* equation in [40].

4.1.4 Actuation Kinematics

The contact kinematics equation is still missing the rotation of the wheel itself as a joint rate variable. The rotation leads to a translational velocity of the contact frame in x-direction by rolling the wheel along the surface. Additional motion might occur due to slip. Hence, the x-component of the translational velocity vector can be rewritten as

$$v_x^C = r\dot{\rho} + \upsilon_x \tag{4.20}$$

with r being the wheel radius, $\dot{\rho}_j$ being the wheel angular velocity at the contact point of wheel j and υ_x being the longitudinal slip. All other components of the velocity vector are not affected by the rotation of the wheel and are modeled as additional slip variables:

$$\begin{bmatrix} \boldsymbol{v}^C \\ \boldsymbol{\omega}^C \end{bmatrix} = \begin{bmatrix} v_x^C \\ v_y^C \\ v_z^C \\ \omega_x^C \\ \omega_y^C \\ \omega_z^C \end{bmatrix} = \begin{bmatrix} r \\ 0 \\ 0 \\ 0 \\ 0 \\ 0 \end{bmatrix} \dot{\rho} + \begin{bmatrix} \upsilon_x \\ \upsilon_y \\ \upsilon_z \\ \zeta_x \\ \zeta_y \\ \zeta_z \end{bmatrix} = \boldsymbol{h}\dot{\rho} + \boldsymbol{\epsilon} \tag{4.21}$$

For a rigid wheel on a rigid surface, υ_z , ζ_x and ζ_y can be set to zero, since the wheel can not move through the surface and is assumed to stay in contact with it at all times. υ_y and ζ_z can occur due to side and turn slip. Substituting (4.21) into (4.19) for wheel j leads to

$$\boldsymbol{h}\dot{\rho}_j + \boldsymbol{\epsilon}_j = \boldsymbol{D}_j \begin{bmatrix} \boldsymbol{v}^R \\ \boldsymbol{\omega}^R \end{bmatrix} + \boldsymbol{E}_j\dot{\boldsymbol{\varphi}} \tag{4.22}$$

The overall body motion of the rover reference frame is the composite effect of all kinematic chains [40]. Combining the equations resulting from (4.22) for all six wheels, one obtains the aggregate formulation

$$\boldsymbol{H}\dot{\rho} + \boldsymbol{\epsilon} = \boldsymbol{D} \begin{bmatrix} \boldsymbol{v}^R \\ \boldsymbol{\omega}^R \end{bmatrix} + \boldsymbol{E}\dot{\boldsymbol{\varphi}} \tag{4.23}$$

with $\boldsymbol{H} = \mathrm{blockdiag}(\boldsymbol{h})$ the 36×6 blockdiagonal matrix created from $\boldsymbol{h}$, $\dot{\boldsymbol{\rho}} = [\dot{\rho}_1 \ldots \dot{\rho}_6]^T$ the 6×1 vector of wheel angular velocities, $\boldsymbol{\epsilon} = \left[\boldsymbol{\epsilon}_1^T \ldots \boldsymbol{\epsilon}_6^T\right]^T$ the 36×1 vector of all slip values, $\boldsymbol{D} = \mathrm{stack}(\boldsymbol{D}_j)$ the 36×6 matrix of stacked $\boldsymbol{D}_j$ matrices, $\boldsymbol{E} = \mathrm{stack}(\boldsymbol{E}_j)$ the 36×21 matrix of stacked $\boldsymbol{E}_j$ matrices and $\boldsymbol{\varphi}$ the 21×1 vector of the DH joint rates. This can be rewritten as

$$\boldsymbol{K} \begin{bmatrix} \dot{\boldsymbol{\rho}} \\ \boldsymbol{\epsilon} \end{bmatrix} = \boldsymbol{J} \begin{bmatrix} \boldsymbol{v}^R \\ \boldsymbol{\omega}^R \\ \dot{\boldsymbol{\varphi}} \end{bmatrix} \tag{4.24}$$

with $\boldsymbol{K} = \begin{bmatrix} \boldsymbol{H} & \boldsymbol{I}_{36} \end{bmatrix}$ being a 36×42 matrix, $\boldsymbol{I}_{36}$ being the 36×36 unity matrix and $\boldsymbol{J} = \begin{bmatrix} \boldsymbol{D} & \boldsymbol{E} \end{bmatrix}$ being the 36×27 *rover jacobian* matrix, relating body and joint velocities to velocities at the contact points.

To control the rover motion, the joint rates of the actuated joints need to be computed for a given desired body velocity and potential additional constraints. To achieve this, (4.24) can be partitioned into sets of known ($\hat{}$) and unknown ($\tilde{}$) quantities:

$$\begin{bmatrix} -\tilde{\boldsymbol{J}} & \tilde{\boldsymbol{K}} \end{bmatrix} \begin{bmatrix} \tilde{\boldsymbol{v}}^R \\ \tilde{\boldsymbol{\omega}}^R \\ \dot{\tilde{\boldsymbol{\varphi}}} \\ \dot{\tilde{\boldsymbol{\rho}}} \\ \dot{\tilde{\boldsymbol{\epsilon}}} \end{bmatrix} = \begin{bmatrix} \hat{\boldsymbol{J}} & -\hat{\boldsymbol{K}} \end{bmatrix} \begin{bmatrix} \hat{\boldsymbol{v}}^R \\ \hat{\boldsymbol{\omega}}^R \\ \dot{\hat{\boldsymbol{\varphi}}} \\ \dot{\hat{\boldsymbol{\rho}}} \\ \dot{\hat{\boldsymbol{\epsilon}}} \end{bmatrix} \tag{4.25}$$

Known quantities could be desired body velocities, sensed or constrained slip values or desired constraints on the motion of joints. Unknown quantities are generally unconstrained or unmeasurable body velocities, joint rates, rolling rates or slip values. $\hat{\boldsymbol{J}}$ and $\tilde{\boldsymbol{J}}$ are appropriate submatrices of $\boldsymbol{J}$, respectively containing the columns corresponding to the known and unknown body velocities and joint rates. The submatrices $\hat{\boldsymbol{K}}$ and $\tilde{\boldsymbol{K}}$ are similarly defined for the wheel rolling rates and slip values. (4.25) specifies the *actuation kinematics* as in [38, 40] and can be written in a more compact form as

$$\boldsymbol{L}\dot{\boldsymbol{p}} = \boldsymbol{N}\dot{\boldsymbol{q}} \tag{4.26}$$

with $\boldsymbol{L} = \begin{bmatrix} -\tilde{\boldsymbol{J}} & \tilde{\boldsymbol{K}} \end{bmatrix}$ a $36 \times \tilde{n}$ matrix where $\tilde{n}$ is the number of unknowns, $\boldsymbol{N} = \begin{bmatrix} \hat{\boldsymbol{J}} & -\hat{\boldsymbol{K}} \end{bmatrix}$ a $36 \times \hat{n}$ matrix where $\hat{n}$ is the number of knowns and $\dot{\boldsymbol{q}}$ and $\dot{\boldsymbol{p}}$ the $\hat{n}$- and $\tilde{n}$-dimensional vectors of known and unknown body velocities, joint rates, rolling rates and slip values. Solving this equation for $\dot{\boldsymbol{p}}$, one can extract the quantities needed for actuating the rover joints to achieve the desired motion. These values, together with the actuated joint rates specified as known quantities in $\dot{\boldsymbol{q}}$, can be commanded to the joint motors. Other quantities are found as a by-product.

4.1.5 Pseudoinverse Solution

Moore-Penrose Pseudoinverse

Since in general the matrix $\boldsymbol{L}$ is non-square and does not have full rank, it can not simply be inverted to find the solution for $\dot{\boldsymbol{p}}$ in (4.26). Depending on the rank of $\boldsymbol{L}$, no solution or even infinitely many solutions might exist. Instead of searching for an exact solution, one can try to minimize the least-squares task error norm

$$\frac{1}{2} \left\| \boldsymbol{N}\dot{\boldsymbol{q}} - \boldsymbol{L}\dot{\boldsymbol{p}} \right\|^2 \tag{4.27}$$

This can be accomplished through the Moore-Penrose pseudoinverse, which can be computed through singular value decomposition (SVD) and is denoted by a superscript $^+$:

$$\dot{\boldsymbol{p}} = \boldsymbol{L}^+ \boldsymbol{N}\dot{\boldsymbol{q}} \tag{4.28}$$

When computing the pseudoinverse, numerical inaccuracies can lead to undesired solutions and erratic joint movements. These can be suppressed by treating singular values in the computation below a tolerance threshold as zero. This has to be tuned to not suppress desired motions. Moreover, computing the pseudoinverse is computationally expensive. The kinematic model was implemented on the EXM-BB2 rover running at a reduced rate of 100 Hz.

Additionally to minimizing the task error norm, the Moore-Penrose pseudoinverse minimizes the norm $\frac{1}{2} \left\| \dot{\boldsymbol{p}} \right\|^2 = \frac{1}{2} \dot{\boldsymbol{p}}^T \dot{\boldsymbol{p}}$ out of all minimal task error solutions. Thus, if infinitely many solutions exist for vector $\dot{\boldsymbol{p}}$, it computes the one with minimal length. Alternatively, the weighted norm $\frac{1}{2} \left\| \dot{\boldsymbol{p}} \right\|_{\boldsymbol{W}}^2 = \frac{1}{2} \dot{\boldsymbol{p}}^T \boldsymbol{W} \dot{\boldsymbol{p}}$ of the the solution vector can be minimized, with $\boldsymbol{W}$ an $\tilde{n} \times \tilde{n}$ weighting matrix for the elements in $\dot{\boldsymbol{p}}$. According to [53], the corresponding weighted Moore-Penrose pseudoinverse can be computed as

$$\boldsymbol{L}_{\boldsymbol{W}}^+ = \boldsymbol{W}^{-\frac{1}{2}} \left(\boldsymbol{L}\boldsymbol{W}^{-\frac{1}{2}} \right)^+ \tag{4.29}$$

with the solution vector $\dot{\boldsymbol{p}}$ then given as

$$\dot{\boldsymbol{p}} = \boldsymbol{L}_{\boldsymbol{W}}^+ \boldsymbol{N}\dot{\boldsymbol{q}} = \boldsymbol{W}^{-\frac{1}{2}} \left(\boldsymbol{L}\boldsymbol{W}^{-\frac{1}{2}} \right)^+ \boldsymbol{N}\dot{\boldsymbol{q}} \tag{4.30}$$

This allows for an optimization of the possible minimal task error solutions according to some chosen goal – e.g. minimal energy consumption or joint prioritization.

Rank Analysis

The character of the solution of (4.26) depends on the rank of $\boldsymbol{L}$ and $\boldsymbol{N}$ and can be related to properties of the rover joint configuration. Three cases can be examined according to [38]:

- Only in the case of $\text{rank}[\boldsymbol{L}|\boldsymbol{N}] = \text{rank}[\boldsymbol{L}]$, one exact solution exists.
- If $\text{rank}[\boldsymbol{L}|\boldsymbol{N}] > \text{rank}[\boldsymbol{L}]$, the system of equations is overdetermined.

  In this case, an exact solution exists only if $\text{rank}[\boldsymbol{L}|\boldsymbol{N}\dot{\boldsymbol{q}}] = \text{rank}[\boldsymbol{L}]$, otherwise not. This might be the case due to an overconstrained system, where the desired motion is impossible to achieve, or due to numerical or motor controller inaccuracies. For example, if all rover wheels are pointing forwards and side slip v_y for all wheels is constrained to 0, no sideways motion v_y^R of the rover body is possible.
- If $\text{rank}[\boldsymbol{L}] < \text{size}(\dot{\boldsymbol{p}})$, the system of equations is underdetermined.

  In this case, infinitely many solutions exist. This can be due to a kinematic configuration of the robot that allows multiple combinations of joint motions to achieve the desired body motion. For the EXM-BB2 rover for example, a forward motion v_x^R of the rover body at steering joint angle $\varphi_S = 0$ for all wheels is possible both by a rotation $\dot{\rho}$ of the rover wheels or by a rotation $\dot{\varphi}_W$ of the walking joints and a simultaneous counter-rotation $\dot{\varphi}_A$ of the leg assembly around the wheel axis.

4.1.6 Kinematic Redundancies

The EXM-BB2 rover is a high-mobility rover with a large number of joints. Depending on the joint configuration, the desired body velocity as well as the joint and slip constraints, the solution vector $\dot{\boldsymbol{p}}$ is not unique and offers additional degrees of freedom to achieve the desired motion. This can be utilized to achieve lower-priority objectives in addition to the desired body motion. One possible method to fulfill lower-priority sub-tasks is through null-space projection.

Null-Space Projection

All solutions to the homogeneous equation $\boldsymbol{L}\dot{\boldsymbol{p}}_h = \boldsymbol{0}$ lie in the null-space of $\boldsymbol{L}$. They can be superimposed onto a particular solution for $\boldsymbol{L}\dot{\boldsymbol{p}} = \boldsymbol{N}\dot{\boldsymbol{q}}$ without interfering with the primary task. Generalizing (4.30) with the homogeneous solution leads to

$$\dot{\boldsymbol{p}} = \boldsymbol{L}_W^+ \boldsymbol{N}\dot{\boldsymbol{q}} + \dot{\boldsymbol{p}}_h \tag{4.31}$$

consisting of the particular solution $\dot{\boldsymbol{p}}_p = \boldsymbol{L}_W^+ \boldsymbol{N}\dot{\boldsymbol{q}}$ and the homogeneous solution $\dot{\boldsymbol{p}}_h$. According to [54], $\dot{\boldsymbol{p}}_h$ can be chosen according to a desired sub-task by formulating it in terms of a desired vector of unknown quantities $\dot{\boldsymbol{p}}_0$ and projecting it into the null-space of $\boldsymbol{L}$:

$$\dot{\boldsymbol{p}}_h = \left(\boldsymbol{I} - \boldsymbol{L}_W^+ \boldsymbol{L}\right) \dot{\boldsymbol{p}}_0 \tag{4.32}$$

$\dot{\boldsymbol{p}}_0$ is a $\tilde{n} \times 1$ vector ($\tilde{n}$ being the number of unknown quantities) with the same element order as the solution $\dot{\boldsymbol{p}}$. $\boldsymbol{I}_{\tilde{n}}$ is the $\tilde{n} \times \tilde{n}$ unity matrix. Overall, this leads to the general solution

$$\dot{\boldsymbol{p}} = \boldsymbol{L}_W^+ \boldsymbol{N}\dot{\boldsymbol{q}} + \left(\boldsymbol{I} - \boldsymbol{L}_W^+ \boldsymbol{L}\right) \dot{\boldsymbol{p}}_0 \tag{4.33}$$

which solves (4.26) by minimizing the least-squares error (4.27) while fulfilling the desired sub-task $\dot{\boldsymbol{p}}_0$ as good as possible without interfering with the primary task. (4.33) can be implemented more efficiently by rewriting it as

$$\dot{\boldsymbol{p}} = \dot{\boldsymbol{p}}_0 + \boldsymbol{L}_W^+ \left(\boldsymbol{N}\dot{\boldsymbol{q}} - \boldsymbol{L}\dot{\boldsymbol{p}}_0\right) \tag{4.34}$$

which reduces the number of required matrix-vector multiplications from four to three. $\dot{\boldsymbol{p}}_0$ can be chosen as the negative gradient of an objective function $s(\boldsymbol{p})$ to be minimized (*projected gradient method*, PG, see [53, 54]):

$$\dot{\boldsymbol{p}}_0 = -\nabla_{\boldsymbol{p}} s(\boldsymbol{p}) \tag{4.35}$$

Through this choice of $\dot{\boldsymbol{p}}_0$, (4.34) realizes one step of a constrained optimization problem. A possible formulation for $s(\boldsymbol{p})$ is presented in Section 4.2.2.

4.1.7 Joint Actuation

Joint Commands

The quantities needed for actuating the rover joints can be extracted from vectors $\dot{\boldsymbol{p}}$ and $\dot{\boldsymbol{q}}$. For the EXM-BB2 rover, these quantities are the walking joint rates $\dot{\varphi}_W$, the steering joint rates $\dot{\varphi}_S$, the contact angle rates $\dot{\varphi}_A$ and the wheel rolling rates $\dot{\rho}$. The walking joint rates $\dot{\varphi}_W$ and the steering joint rates $\dot{\varphi}_S$ can be directly commanded to the respective joint motors. The contact angle rates $\dot{\varphi}_A$, which are caused by a rotation of the leg assembly around the wheel axis with respect to the wheel-terrain contact point, and the wheel rolling rates $\dot{\rho}_j$ are both relative motions around the same axis. They are commanded to the driving joint motors as the sum $\dot{\varphi}_A + \dot{\rho}$.

Actuation of Steering Joints

Actuated motion at a wheel contact point is only possible along the wheel rolling direction. If a wheel is not oriented properly, this would lead to the overall body motion being impossible to achieve or lateral slip being induced at the contact point. Thus, each wheel needs to be aligned such that the translational velocity vector $\mathbf{v}^C = [v_x^C, v_y^C, v_z^C]^T$ at the contact point aligns with the x-axis of the contact frame C. This alignment can be accomplished by rotating the steering joint accordingly. $\mathbf{v}^C$ can be estimated from (4.19) as

$$\boldsymbol{v}_{\text{est}}^C = \mathbf{v}^C\left(\dot{\boldsymbol{\varphi}} = \mathbf{0}\right) = \bar{\boldsymbol{D}} \begin{bmatrix} \boldsymbol{v}^R \\ \boldsymbol{\omega}^R \end{bmatrix} \tag{4.36}$$

by setting the joint rate vector $\dot{\boldsymbol{\varphi}}$ to zero, whose quantities are not yet known for the current time step. $\bar{\boldsymbol{D}}$ consists of the first three rows of $\boldsymbol{D}_j$. From this, the desired steering joint angle $\varphi_{S,\text{des}}$ can be computed as

$$\varphi_{S,\text{des}} = \varphi_S + \arctan\frac{v_{y,\text{est}}^C}{v_{x,\text{est}}^C} = \arctan\frac{v_{y,\text{est}}^C\left(\varphi_S = 0\right)}{v_{x,\text{est}}^C\left(\varphi_S = 0\right)} \tag{4.37}$$

under the assumption of small contact angles φ_C. Due to invariance of the wheel driving direction, this can be adjusted by $\pm\pi$ to choose the shorter angular distance and to avoid

joint limits. To pull the steering joint towards this position, the steering joint rate $\dot{\varphi}_S$ is set to

$$\dot{\varphi}_S = k_S \left(\varphi_S - \varphi_{S,\text{des}} \right) \tag{4.38}$$

which is essentially the derivative of a quadratic potential function with the scaling parameter k_S. $\dot{\varphi}_S$ needs to be computed as a preliminary step and is then included as a known quantity in vector $\dot{\boldsymbol{q}}$ of 4.26.

4.2 Driving Mode 1: Balancing

Based on the kinematic modeling approach described above, two locomotion modes were implemented for the EXM-BB2 rover. The first one is the so-called Balancing Mode. It is a general locomotion mode that allows to specify a desired motion for the rover body through the velocities v_x^R, v_y^R and ω_z^R of the rover reference frame without any additional primary joint constraints. Specifying only translational velocities v_x^R and v_y^R while setting ω_z^R to zero results in a crab steering motion, while specifying translational velocity v_x^R and rotational velocity ω_z^R while seting v_y^R to zero is similar to Ackermann steering. On top of this, the mode utilizes the available kinematic redundancies to achieve a balanced rover configuration as a secondary objective through

- keeping joints close to their nominal position (away from joint limits)
- increasing tip-over stability
- reducing the rover body tilt

Increasing the tip-over stability can increase safety margins while driving over rough terrain to avoid losing balance. Reducing the rover body tilt can allow the rover to traverse higher slope angles while still meeting operational requirements for on-board experiments that specify a maximum roll or pitch angle during operation. Additionally, it can reduce side-slip while driving sideways along a slope.

4.2.1 Constraints Modeling

Known and Unknown Quantities

The following 27 quantities are specified as known in $\dot{\boldsymbol{q}}$:

- Elements 1 . . . 3: Desired rover body rates $v_x^R = v_{x,\text{des}}^R$, $v_y^R = v_{y,\text{des}}^R$ and $\omega_z^R = v_{z,\text{des}}^R$
- Elements 4 . . . 9: Steering joint rates $\dot{\boldsymbol{\varphi}}_S = [\dot{\varphi}_{S_1}, \ldots, \dot{\varphi}_{S_6}]^T$ as defined in Section 4.1.7
- Elements 10 . . . 15: Longitudinal slip rates $\boldsymbol{\upsilon}_x = [\upsilon_{x,1}, \ldots, \upsilon_{x,6}]^T$ constrained to $\mathbf{0}$
- Elements 16 . . . 21: Perpendicular slip rates $\boldsymbol{\upsilon}_x = [\upsilon_{x,1}, \ldots, \upsilon_{z,6}]^T$ constrained to $\mathbf{0}$
- Elements 22 . . . 27: Pitch slip rates $\boldsymbol{\zeta}_y = [\zeta_{y,1}, \ldots, \zeta_{y,6}]^T$ constrained to $\mathbf{0}$

$$\dot{\boldsymbol{q}} = \begin{bmatrix} v_x^R \\ v_y^R \\ \omega_z^R \\ \dot{\boldsymbol{\varphi}}_S \\ \boldsymbol{\upsilon}_x \\ \boldsymbol{\upsilon}_z \\ \boldsymbol{\zeta}_y \end{bmatrix} = \begin{bmatrix} v_{x,\text{des}}^R \\ v_{y,\text{des}}^R \\ \omega_{z,\text{des}}^R \\ \dot{\boldsymbol{\varphi}}_S \\ \mathbf{0}_{6\times 1} \\ \mathbf{0}_{6\times 1} \\ \mathbf{0}_{6\times 1} \end{bmatrix} \in \mathbb{R}^{27} \tag{4.39}$$

This leaves 42 unknown quantities to be computed in $\dot{\boldsymbol{p}}$:

- Elements 1 . . . 3: Rover body rates v_z^R, ω_x^R and ω_y^R
- Elements 4 . . . 6: Bogie joint rates $\dot{\boldsymbol{\varphi}}_B = [\dot{\varphi}_{B_1}, \ldots, \dot{\varphi}_{B_3}]^T$
- Elements 7 . . . 12: Walking joint rates $\dot{\boldsymbol{\varphi}}_W = [\dot{\varphi}_{W_1}, \ldots, \dot{\varphi}_{W_6}]^T$
- Elements 13 . . . 18: Contact angle rates $\dot{\boldsymbol{\varphi}}_C = [\dot{\varphi}_{C_1}, \ldots, \dot{\varphi}_{C_6}]^T$
- Elements 19 . . . 24: Wheel driving rates $\dot{\boldsymbol{\rho}} = [\dot{\rho}_1, \ldots, \rho_6]^T$
- Elements 25 . . . 30: Lateral slip rates $\boldsymbol{\upsilon}_y = [\upsilon_{y,1}, \ldots, \upsilon_{y,6}]^T$

- Elements 31 . . . 36: Roll slip rates $\boldsymbol{\zeta}_x = [\zeta_{x,1}, \ldots, \zeta_{x,6}]^T$
- Elements 37 . . . 42: Yaw slip rates $\boldsymbol{\zeta}_z = [\zeta_{z,1}, \ldots, \zeta_{z,6}]^T$

$$\dot{\boldsymbol{p}} = \begin{bmatrix} v_z^R \\ \omega_x^R \\ \omega_y^R \\ \dot{\boldsymbol{\varphi}}_B \\ \dot{\boldsymbol{\varphi}}_W \\ \dot{\boldsymbol{\varphi}}_C \\ \dot{\boldsymbol{\rho}} \\ \boldsymbol{v}_y \\ \boldsymbol{\zeta}_x \\ \boldsymbol{\zeta}_z \end{bmatrix} \in \mathbb{R}^{42} \tag{4.40}$$

Pseudoinverse Weighting

The weighting matrix $\boldsymbol{W}$ for the pseudoinverse $\boldsymbol{L}_{\boldsymbol{W}}^{+}$ is specified as a 42×42 diagonal matrix, with $\boldsymbol{W} = \mathrm{diag}(\boldsymbol{w})$, $\boldsymbol{w} \in \mathbb{R}^{42}$ and

$$\boldsymbol{w}_{1:18} = [1, \ldots, 1]^T \tag{4.41}$$

$$\boldsymbol{w}_{19:24} = \left[\frac{1}{10}, \ldots, \frac{1}{10}\right]^T \tag{4.42}$$

$$\boldsymbol{w}_{25:42} = [1, \ldots, 1]^T \tag{4.43}$$

Elements 19 through 24 correspond to the wheel driving rates $\dot{\boldsymbol{\rho}}$. This weighting leads to a preference of wheel rolling over walking joint motion when moving the rover body forward.

4.2.2 Sub-Task Objective Function

The sub-tasks mentioned at the beginning of this section are defined through an objective function s to be minimized subject to the primary task constraints using the projected

gradient method as described in Section 4.1.6:

$$s = k_\Theta s_\Theta + k_\Phi s_\Phi + k_\mu s_\mu + k_W s_W \tag{4.44}$$

It consists of the four terms s_Θ, s_Φ, s_μ and s_W based on the rover body pitch and roll angle Θ and Φ, a tip-over measure μ as well as the walking joint angles and φ_W. The terms are described in the following sections and can be weighted through the factors k_Θ, k_Φ, k_μ and k_W to tune the rover behavior.

Reducing Rover Body Tilt

To reduce the rover body tilt, the objective is to reduce the rover's pitch and roll angle Θ and Φ, which can be measured through the IMU. The objective function can be formulated for both pitch and roll independently as quadratic functions:

$$s_\Theta = \frac{1}{2}\Theta^2 \tag{4.45}$$

$$s_\Phi = \frac{1}{2}\Phi^2 \tag{4.46}$$

Increasing Tip-Over Stability

Tip-over of the rover body happens when the rover's gravity vector, originating at the rover's center of mass, lies outside of the rover's support polygon. The further the gravity vector lies inside, the more stable the rover configuration is. Based on this, a stability measure μ was formulated by Tarokh et al. in [40], using wheel-terrain contact point vectors $\boldsymbol{o}_j^R = \left[o_{j,x}^R, o_{j,y}^R, o_{j,z}^R\right]^T$ pointing to the origin of the contact frame, with

$$\begin{bmatrix} o_{j,x}^R \\ o_{j,y}^R \\ o_{j,z}^R \\ 1 \end{bmatrix} = \boldsymbol{T}_C^R \boldsymbol{o}_j^C = \boldsymbol{T}_C^R \begin{bmatrix} 0 \\ 0 \\ 0 \\ 1 \end{bmatrix} \tag{4.47}$$

under the assumption that the CoG lies roughly at the origin of the rover reference frame. Each consecutive pair of vectors $\boldsymbol{o}_j^R$ forms a plane for which the perpendicular unit vector is given as

$$\boldsymbol{t}_j = \frac{\boldsymbol{o}_j^R \times \boldsymbol{o}_{j+1}^R}{\left\| \boldsymbol{o}_j^R \times \boldsymbol{o}_{j+1}^R \right\|}, \quad j = 1, \ldots, 6, \quad \boldsymbol{o}_7^R = \boldsymbol{o}_1^R \tag{4.48}$$

From the IMU orientation data, the rover unit gravity vector $\boldsymbol{g}$ can be computed as

$$\boldsymbol{g} = \begin{bmatrix} \sin(\Phi) \\ -\sin(\Theta)\cos(\Phi) \\ -\cos(\Theta)\cos(\Phi) \end{bmatrix} \tag{4.49}$$

with body pitch angle Θ and body roll angle Φ. Based on this, a stability measure μ_j can be formulated as the dot product between $\boldsymbol{t}_j$ and $\boldsymbol{g}$:

$$\mu_j = \boldsymbol{g}^T \boldsymbol{t}_j \tag{4.50}$$

As an approximation, the support polygon is assumed to be spanned by the six wheel-terrain contact points. When the gravity vector is at the edge of this polygon between $\boldsymbol{o}_j^R$ and $\boldsymbol{o}_{j+1}^R$, the rover is at the verge of tip-over. In this case, $\boldsymbol{t}_j$ and $\boldsymbol{g}$ are orthogonal, which results in $\mu_j = 0$. On the other hand, when $\boldsymbol{t}_j$ and $\boldsymbol{g}$ are parallel, the rover is stable with regard to this edge, resulting in $\mu_j = 1$. An objective function for the overall tip-over stability of the rover can then be formulated as the negative product of all μ_j:

$$s_\mu = -\prod_{j=1}^{6} \mu_j \tag{4.51}$$

Preferring Nominal Configuration

Only considering s_Θ, s_Φ and s_μ for the objective function s would result in a flat rover configuration where the legs are spread away from the body. To avoid this, a fourth term has to be introduced that pulls the walking joints towards their nominal (zero) position:

$$s_W = \frac{1}{4}\sum_{j=1}^{6}\varphi_{W_j}^4 \tag{4.52}$$

As a fourth degree function compared to a second degree function, it allows more movement around the nominal position while pushing away stronger from the joint limits.

Gradient of Objective Function

Overall, the objective function is given as

$$s = k_\Theta \frac{1}{2}\Theta^2 + k_\Phi \frac{1}{2}\Phi^2 + k_\mu s_\mu + k_W \frac{1}{4}\sum_{j=1}^{6}\varphi_{W_j}^4 \tag{4.53}$$

Minimization of this function leads to the desired behavior. However, this minimization is subject to the constraints defined through $\dot{\boldsymbol{q}}$, which define the primary task of the rover. The solution for this constrained optimization problem is given by (4.34) with the choice of $\dot{\boldsymbol{p}}_0$ as the negative gradient of s as defined in (4.35). Looking at the elements of $\dot{\boldsymbol{p}}$ as given in Section 4.2.1, this gradient can be expressed as

$$\nabla_{\boldsymbol{p}} s(\boldsymbol{p}) = \begin{bmatrix} 0 \\ \partial_\Theta s \\ \partial_\Phi s \\ \mathbf{0}_{3\times 1} \\ \partial_{\boldsymbol{\varphi}_W} s \\ \mathbf{0}_{30\times 1} \end{bmatrix} + \nabla_{\boldsymbol{p}} s_\mu(\boldsymbol{p}) \tag{4.54}$$

with

$$\partial_\Theta s = \frac{\partial s}{\partial \Theta} = k_\Theta \Theta \tag{4.55}$$

$$\partial_\Phi s = \frac{\partial s}{\partial \Phi} = k_\Phi \Phi \tag{4.56}$$

$$\partial_{\boldsymbol{\varphi}_W} s = \frac{\partial s}{\partial \boldsymbol{\varphi}_W} = \left[\frac{\partial s}{\partial \varphi_{W_1}}, \ldots, \frac{\partial s}{\partial \varphi_{W_6}} \right]^T \tag{4.57}$$

and

$$\frac{\partial s}{\partial \varphi_{W_j}} = k_W \varphi_{W_j}^3 \tag{4.58}$$

$\nabla_{\boldsymbol{p}} s_\mu(\boldsymbol{p})$ can be approximated through numerical differentiation. Using the symmetric derivative, the elements of $\nabla_{\boldsymbol{p}} s_\mu(\boldsymbol{p})$ can be computed as

$$\frac{\partial s_\mu}{\partial p_i} = \frac{s_\mu(\boldsymbol{p} + \boldsymbol{\epsilon}_i) - s_\mu(\boldsymbol{p} - \boldsymbol{\epsilon}_i)}{2 \left\| \boldsymbol{\epsilon}_i \right\|} + \mathcal{O}(\left\| \boldsymbol{\epsilon}_i \right\|) \tag{4.59}$$

with $\boldsymbol{\epsilon}_i \in \mathbb{R}^{42}$ a vector of zeros except for the i-th element.

4.3 Driving Mode 2: Wheel Walking

The second locomotion mode implemented based on the kinematic model is the so-called Wheel Walking locomotion mode. It is a specialized mode for enhanced traversability of slopes, increased traction in entrapment situations and reduced sinkage in soft soils. By employing the walking joints to swivel the rover legs below the rover body in a repeating pattern, slip (and thus sinkage) at the rolling wheels can be reduced while holding the other wheels stationary. Using the kinematic model, the motion of all joints can be synchronized and adapted to the current terrain profile while the rover body is commanded at a constant velocity. Due to the alignment of the joints on the rover leg assemblies, the steering joints cannot be used in this mode and their positions are fixed at $\varphi_{S_j} = 0 \; \forall \, j \in \{1, \ldots, 6\}$.

4.3.1 Parameters

Gait

By changing the order and combination of the leg movements, different Wheel Walking gaits can be implemented. Each gait can be split into a number of phases n_p, where in each phase a set of wheels moves forward simultaneously. In a gait with a higher number of phases, less wheels move simultaneously, but higher joint speeds are needed to achieve the same desired body velocity. Following the last phase, the sequence starts from the beginning, with a swap of the left and right side wheels in the sequence for some gaits to avoid a drift around the yaw axis.

- The Side-by-Side gait moves the right side wheels followed by the left side wheels of the rover.
- The Tripod gait moves front and rear wheels of one side and the center wheel of the other side simultaneously.
- The Axle-by-Axle gait moves both front wheels followed by both center wheels followed by both rear wheels.
- The Kruse gait moves front and center wheels simultaneously as one group followed by the rear wheels one by one.
- The Hybrid gait is a mix between the Axle-by-Axle and the Kruse gait. It moves both front wheels followed by both center wheels followed by the rear wheels one by one.
- The Single Wheel gait moves each wheel separately, going through from one side to the other and from front to rear.

Table 4.4 lists the implemented gaits in a concise form. Preliminary tests showed that a higher number of phases / a lower number of simultaneously moved wheels is advantageous with regard to slip. Additionally, unsymmetrical gaits where a left side wheel is not moved simultaneously with its counterpart on the right side are less directionally stable. Due to this, the Side-by-Side gait as well as the Tripod gait were discarded for the experimental part. The Single Wheel gait was discarded since it needs significantly higher joint speeds to achieve the same desired body velocity as the other gaits due to the high number of phases.

Table 4.4: **Wheel Walking gaits**

Gait name	Abbrev.	# of phases (n_p)	Active wheel sequence
Side-by-Side	SBS	2	(1,2,3) → (4,5,6)
Tripod	TRI	2	(1,3,5) → (2,4,6)
Axle-by-Axle	ABA	3	(1,6) → (2,5) → (3,4)
Kruse	KRU	3	(1,2,5,6) → (3) → (4) (1,2,5,6) → (4) → (3)
Hybrid	HYB	4	(1,6) → (2,5) → (3) → (4) (1,6) → (2,5) → (4) → (3)
Single Wheel	SW	6	(1) → (6) → (2) → (5) → (3) → (4) (6) → (1) → (5) → (2) → (4) → (3)

Burnout

When traversing slopes, Wheel Walking reduces the effective slip of the rover by "anchoring" the stationary wheels in the sand while moving the others forward. The effectiveness of this depends on the amount of soil supporting the stationary wheels from behind. To increase this effect, a "burnout" phase can be added to the Wheel Walking motion, where the wheels are turning on the spot after the leg forward movement is completed to dig into the soil and transport material behind the wheel. This doubles the number of phases for a gait and increases the wheel rolling speed if the desired rover body velocity should remain unchanged. Impact on traversability and power consumption needs to be analyzed to see whether this provides an overall advantage.

Swivel Angle

For the movement of the rover "legs", some measure has to be defined that determines the switch-over to the next phase. Additionally, the leg movement needs to be constrained in order to avoid a drift of the walking joint angle towards the joint limits over time. This is achieved by defining maximum backwards and forwards walking joint angles for each wheel which hold the wheel in position when reached and act as a trigger for the next phase. In general, larger swivel angles seem advantageous, since they allow the rover to take larger "steps" and move the wheels further out of their pits. At the same time, the load on the walking joint is increased with a larger torque acting on gearbox and motor. Additionally, the construction of the flight rover limits the walking joints to be turned only in one direction from their nominal position, as mentioned in Section 2.1.3.

4.3.2 Constraints Modeling

Wheel Type Mapping

In every time step, each rover wheel $j \in \mathcal{W} = \{1, \ldots, 6\}$ is assigned to one or more of the following groups:

- Active wheels $\mathcal{W}_a \subset \mathcal{W}$ are the wheels performing the forward walking motion during the current phase as defined for the gait
- Inactive wheels $\mathcal{W}_i = \mathcal{W} \setminus \mathcal{W}_a$ are all other wheels
- Walking wheels $\mathcal{W}_w \subset \mathcal{W}_a$ are all active wheels which have not yet reached the forward walking joint angle limit
- Stopped wheels $\mathcal{W}_s \subset \mathcal{W}_i$ are all inactive wheels which have not yet reached the backward walking joint angle limit
- Holding wheels $\mathcal{W}_h = (\mathcal{W}_a \setminus \mathcal{W}_w) \cup (\mathcal{W}_i \setminus \mathcal{W}_s)$ are all active wheels which have reached the forward walking joint angle limit and all inactive wheels which have reached the backward walking joint angle limit
- Burnout wheels $\mathcal{W}_b = \mathcal{W}_a$ are only set during the burnout phase, otherwise $\mathcal{W}_b = \emptyset$

Based on these assignments, the known and unknown quantities in $\dot{\boldsymbol{q}}$ and $\dot{\boldsymbol{p}}$ as well as the joint weighting matrix $\boldsymbol{W}$ are specified. The phase of the current gait is switched to the next whenever all active wheels have reached the forward walking joint angle limit or when the burnout phase has reached its timer threshold.

Known and Unknown Quantities

The following quantities are specified as known in $\dot{\boldsymbol{q}}$:

- Desired rover body forward velocity $v_x^R = v_{x,\text{des}}^R$
- Rover body lateral velocity $v_y^R = 0$ and rotation rate $\omega_z^R = 0$

- Walking joint rates $\dot{\varphi}_{W_j}\ \forall\, j \in W_w$ as vector $\hat{\dot{\boldsymbol{\varphi}}}_W \in \mathbb{R}^{|\mathcal{W}_w|}$ with

$$\dot{\varphi}_{W_j} = \begin{cases} -2n_p \frac{v_x^R}{l_{11}} & \text{if burnout enabled} \\ -0.7n_p \frac{v_x^R}{l_{11}} & \text{otherwise} \end{cases} \qquad \forall\, j \in \mathcal{W}_w \tag{4.60}$$

- Steering joint rates $\dot{\boldsymbol{\varphi}}_S = [\dot{\varphi}_{S_1}, \ldots, \dot{\varphi}_{S_6}]^T$ as defined in Section 4.1.7
- Longitudinal slip rates $\boldsymbol{\upsilon}_x = [\upsilon_{x,1}, \ldots, \upsilon_{x,6}]^T$ with

$$\upsilon_{x,j} = \begin{cases} -2n_p v_x^R & \forall\, j \in \mathcal{W}_b \\ 0 & \text{otherwise} \end{cases} \tag{4.61}$$

  to achieve the burnout motion
- Lateral slip rates $\boldsymbol{\upsilon}_y = [\upsilon_{y,1}, \ldots, \upsilon_{y,6}]^T$ constrained to $\mathbf{0}$
- Perpendicular slip rates $\boldsymbol{\upsilon}_z = [\upsilon_{z,1}, \ldots, \upsilon_{z,6}]^T$ constrained to $\mathbf{0}$
- Pitch slip rates $\boldsymbol{\zeta}_y = [\zeta_{y,1}, \ldots, \zeta_{y,6}]^T$ constrained to $\mathbf{0}$

$$\dot{\boldsymbol{q}} = \begin{bmatrix} v_x^R \\ v_y^R \\ \omega_z^R \\ \hat{\dot{\boldsymbol{\varphi}}}_W \\ \dot{\boldsymbol{\varphi}}_S \\ \boldsymbol{\upsilon}_x \\ \boldsymbol{\upsilon}_y \\ \boldsymbol{\upsilon}_z \\ \boldsymbol{\zeta}_y \end{bmatrix} = \begin{bmatrix} v_{x,\text{des}}^R \\ 0 \\ 0 \\ \hat{\dot{\boldsymbol{\varphi}}}_W \\ \dot{\boldsymbol{\varphi}}_S \\ \boldsymbol{\upsilon}_x \\ \mathbf{0}_{6\times 1} \\ \mathbf{0}_{6\times 1} \\ \mathbf{0}_{6\times 1} \end{bmatrix} \in \mathbb{R}^{33+|\mathcal{W}_w|} \tag{4.62}$$

This leaves the following unknown quantities to be computed in $\dot{\boldsymbol{p}}$:

- Rover body rates v_z^R, ω_x^R and ω_y^R
- Bogie joint rates $\dot{\boldsymbol{\varphi}}_B = [\dot{\varphi}_{B_1}, \ldots, \dot{\varphi}_{B_3}]^T$
- Walking joint rates $\dot{\varphi}_{W_j}$ for $j \in (\mathcal{W}_s \cup \mathcal{W}_h)$ as vector $\tilde{\dot{\boldsymbol{\varphi}}}_W \in \mathbb{R}^{|\mathcal{W}_s|+|\mathcal{W}_h|}$

- Contact angle rates $\dot{\boldsymbol{\varphi}}_C = [\dot{\varphi}_{C_1}, \ldots, \dot{\varphi}_{C_6}]^T$
- Wheel driving rates $\dot{\boldsymbol{\rho}} = [\dot{\rho}_1, \ldots, \rho_6]^T$
- Roll slip rates $\boldsymbol{\zeta}_x = [\zeta_{x,1}, \ldots, \zeta_{x,6}]^T$
- Yaw slip rates $\boldsymbol{\zeta}_z = [\zeta_{z,1}, \ldots, \zeta_{z,6}]^T$

$$\dot{\boldsymbol{p}} = \begin{bmatrix} v_z^R \\ \omega_x^R \\ \omega_y^R \\ \dot{\boldsymbol{\varphi}}_B \\ \dot{\tilde{\boldsymbol{\varphi}}}_W \\ \dot{\boldsymbol{\varphi}}_C \\ \dot{\boldsymbol{\rho}} \\ \boldsymbol{\zeta}_x \\ \boldsymbol{\zeta}_z \end{bmatrix} \in \mathbb{R}^{30+|\mathcal{W}_s|+|\mathcal{W}_h|} \tag{4.63}$$

Pseudoinverse Weighting

The weighting matrix $\boldsymbol{W}$ for the pseudoinverse $\boldsymbol{L}_{\boldsymbol{W}}^{+}$ is specified as a $\tilde{n} \times \tilde{n}$ diagonal matrix with $\boldsymbol{W} = \mathrm{diag}(\boldsymbol{w})$, $\boldsymbol{w} \in \mathbb{R}^{\tilde{n}}$, $\tilde{n} = 30 + |\mathcal{W}_s| + |\mathcal{W}_h|$ and

$$\boldsymbol{w}_{\dot{\varphi}_{W_j} | j \in \mathcal{W}_h} = 10 \tag{4.64}$$

$$\boldsymbol{w}_{\rho_j | j \in \mathcal{W}_s} = 10 \tag{4.65}$$

$$\boldsymbol{w}_{\rho_j | j \in \mathcal{W}_b} = \frac{1}{10} \tag{4.66}$$

with the index specifying the element of $\boldsymbol{w}$ according to its location in $\dot{\boldsymbol{p}}$. This definition aims at

- suppressing any motion of the walking joints for holding wheels (4.64)

- suppressing the wheel rolling motion for stopped wheels (4.65)
- achieving the burnout motion by turning the burnout wheels on the spot (4.66)

4.3.3 Simplified Implementation

On the ExoMars flight rover, available computing power is scarce, since it needs to rely on low-power, radiation-hardened components. Running a full-body kinematic model at a sufficiently high frequency is computationally intensive and may not be feasible or sensible for such a system. Moreover, algorithms running in this kind of environment need to be entirely predictable and safe in their behavior. For a previous test campaign, a simplified Wheel Walking algorithm was developed based on the 2D geometry of the leg assembly of a single wheel moving on flat terrain. It neglects the interaction between the kinematic chains, the motion of the bogie joints and any vertical movement. However, it is computationally inexpensive and the joint motions behave deterministically, independently of the terrain. On the EXM-BB2 rover, this algorithm runs at a rate of 1000 Hz.

Walking Phase

Similarly to the kinematic model implementation, each gait is split into a number of phases. For each phase, a set of active wheels $\mathcal{W}_a \subset \mathcal{W} = \{1, \ldots, 6\}$ is defined and the corresponding legs are swiveled forwards until a predefined limit for the walking joint angle is reached. For the active wheels, the longitudinal velocity of the contact points $v_x^{C_j}$ is computed as

$$v_x^{C_j} = n_p v_{x,\text{des}}^R \quad \forall\, j \in \mathcal{W}_a \tag{4.67}$$

based on the desired longitudinal velocity of the rover reference frame $v_{x,\text{des}}^R$ and the number of phases n_p of the current gait, under the assumption that each phase has the same duration. The corresponding walking joint rates $\dot{\varphi}_{W_j}$ are then computed as

$$\dot{\varphi}_{W_j} = -\frac{v_x^{C_j}}{l_{11}} \frac{1}{\cos(\varphi_{W_j})} \quad \forall\, j \in \mathcal{W}_a \tag{4.68}$$

taking into account the walking joint position φ_{W_j} and the leg length l_{11}. This movement is compensated by a counter-rotation of the leg around the wheel axis, with the contact angle rates $\dot{\varphi}_{A_j}$ given as

$$\dot{\varphi}_{A_j} = -\dot{\varphi}_{W_j} \quad \forall\, j \in \mathcal{W}_a \tag{4.69}$$

The wheel rolling rates $\dot{\rho}_j$ for the active wheels are computed as

$$\dot{\rho}_j = \frac{v_x^{C_j}}{r} \quad \forall\, j \in \mathcal{W}_a \tag{4.70}$$

with r being the wheel radius. They are commanded to the driving motors in addition to the contact angle rates as $\dot{\varphi}_{A_j} + \dot{\rho}_j$. The inactive wheels $\mathcal{W}_i = \mathcal{W} \setminus \mathcal{W}_a$ are kept stationary with no joint movement, so

$$\dot{\varphi}_{W_j} = \dot{\varphi}_{A_j} = \dot{\rho}_j = 0 \quad \forall\, j \in \mathcal{W}_i \tag{4.71}$$

During all phases, the steering joints are kept in their nominal position at all times:

$$\dot{\varphi}_{S_j} = 0 \quad \forall\, j \in \mathcal{W} \tag{4.72}$$

Burnout Phase

If burnout is enabled for a gait, an additional phase is added after each walking phase where the active wheels $\mathcal{W}_a$ are rotating on the spot to dig into the ground. To keep the duration of this phase in sync with the other phases, a time limit equivalent to the time needed to complete a walking phase can be calculated. The time needed to rotate a walking joint from the minimum walking joint angle $\varphi_{W,\min}$ to the maximum walking joint angle $\varphi_{W,\max}$ can be derived from the walking joint rate $\dot{\varphi}_W$ of the active wheels during the walking phase, given by (4.68):

$$\dot{\varphi}_W = \frac{\mathrm{d}\varphi_W}{\mathrm{d}t} \tag{4.73}$$

$$\Rightarrow \quad \mathrm{d}t = \frac{1}{\dot{\varphi}_W}\mathrm{d}\varphi_W \tag{4.74}$$

$$\Rightarrow \quad \Delta t = t_{\max} - t_{\min} = \int_{t_{\min}}^{t_{\max}} \mathrm{d}t = \int_{\varphi_{W,\min}}^{\varphi_{W,\max}} \frac{1}{\dot{\varphi}_W}\mathrm{d}\varphi_W \tag{4.75}$$

$$= -\frac{l_{11}}{n_p v_{x,\mathrm{des}}^R} \int_{\varphi_{W,\min}}^{\varphi_{W,\max}} \cos(\varphi_W)\mathrm{d}\varphi_W \tag{4.76}$$

$$= \frac{l_{11}}{n_p v_{x,\mathrm{des}}^R} \left(\sin(\varphi_{W,\min}) - \sin(\varphi_{W,\max})\right) \tag{4.77}$$

The burnout phase is performed for a duration of Δt by applying the wheel rolling rates of the walking phase to the driving joints without rotating the walking joints:

$$\dot{\varphi}_{W_j} = 0 \quad \forall\, j \in \mathcal{W}_a \tag{4.78}$$

$$\dot{\varphi}_{A_j} = 0 \quad \forall\, j \in \mathcal{W}_a \tag{4.79}$$

$$\dot{\rho}_j = \frac{n_p v_{x,\mathrm{des}}^R}{r} \quad \forall\, j \in \mathcal{W}_a \tag{4.80}$$

All other wheels are kept stationary with no joint movement, so

$$\dot{\varphi}_{W_j} = \dot{\varphi}_{A_j} = \dot{\rho}_j = 0 \quad \forall\, j \in \mathcal{W}_i \tag{4.81}$$

Body Motion Phase

The motion of the rover body is not continuous in this algorithm; during the walking and burnout phases, no forward motion of the rover body is intended. Instead, an additional body motion phase is introduced as the final phase of a gait to move the rover body forward while all wheels remain stationary. This is achieved by inverting the rotation of the

walking joints of the walking phase until the backward walking joint limit is reached. The joint rates in this phase are computed as

$$\dot{\varphi}_{W_j} = \frac{n_p v^R_{x,\mathrm{des}}}{l_{11}} \frac{1}{\cos(\varphi_{W_j})} \quad \forall\, j \in \mathcal{W} \tag{4.82}$$

$$\dot{\varphi}_{A_j} = \dot{\rho}_j = 0 \quad \forall\, j \in \mathcal{W} \tag{4.83}$$

After finishing the body motion phase, the motion sequence starts again with the first walking phase.

5 Experimental Setup

To evaluate the kinematic model and the implemented driving modes, a two-week test campaign was carried out in the Planetary Exploration Laboratory (PEL) at DLR. In an artificial soft-soil environment, the rover was driven up slopes and over ramps to assess and compare its traversability performance and overall behavior in relevant scenarios. In this chapter, the test facility is introduced, its features and specifications are presented and the integration of the rover into the facility is explained. A list of all performed tests is presented and the relevant preparatory procedures are described.

Figure 5.1: **The Planetary Exploration Laboratory at DLR**

5.1 The PEL Facility

The Planetary Exploration Laboratory at DLR (see Figure 5.1) is a test facility for planetary locomotion systems to assess their mobility characteristics in soft-soil environments. It consists of a large sand tub test bed with an adjustable slope, a tracking system for accurate position tracking and a system for automated creation of a digital elevation model (DEM) of the terrain. A movable overhead crane is available for lifting heavy equipment (like rovers) into the test bed, while an adjacent control room is intended for controlling and monitoring of test procedures.

5.1.1 Sand Test Bed

The sand test bed (see Figure 5.2) is a large 10 m x 5.5 m rectangular sand-filled tub, currently subdivided into two segments: A smaller 2.7 m x 5.5 m single-wheel test bed for analysis of wheel-soil interaction, separated from the rest of the tub, and a larger 7.3 m x 5.5 m area for mobility analysis and evaluation of locomotion control algorithms. Part of the larger mobility area is a movable ramp of 3.5 m length, which can be raised up to a slope of 30° through a spindle drive. Soil preparation in the test bed is generally performed using manual tools like shovels, rakes and planks. For reallocation of larger amounts of soil, a vacuum conveyor is available. To cope with the dispersion of dust in the air during soil preparation, a ventilation system is installed.

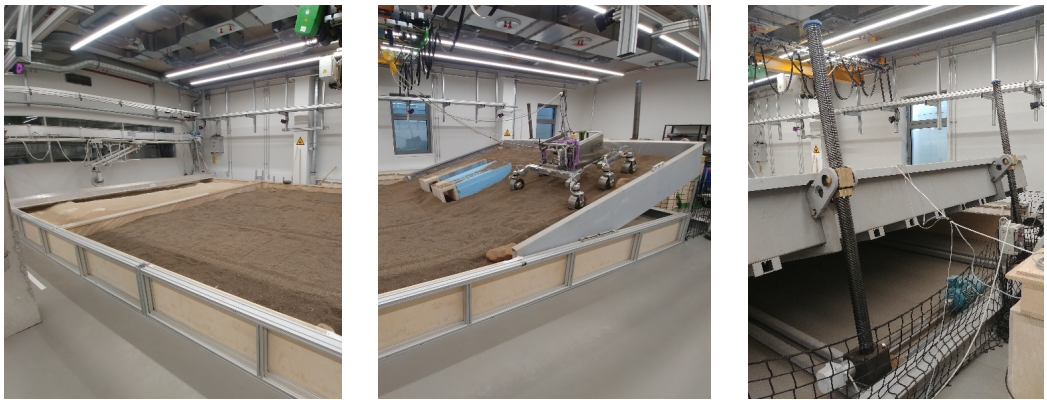

(a) **Single-wheel test bed next to mobility area** (b) **Mobility area with movable ramp** (c) **Backside of ramp with spindle drive**

Figure 5.2: **PEL sand test bed**

Table 5.1: **Bekker parameters (k_c, k_Φ, n), cohesion c and angle of repose Φ**

Soil Type	k_c (kN/m^{n+1})	k_Φ (kN/m^{n+2})	n (-)	c (kPa)	Φ (°)
Eifel Lava	-5.62×10^3	1.85×10^7	1.74	101.8	31.0

Eifel Lava Soil

Figure 5.3: **Close-up of Eifel Lava soil**

Multiple soil types are available in the PEL with various properties regarding grain sizes, composition and cohesion [55]. During this test campaign, the mobility area of the PEL test bed was filled with Eifel Lava soil. Eifel Lava is a general purpose soil used mainly as a foundation material in outdoor construction projects. It has a high angle of repose and is relatively easy to acquire, handle and prepare. Compared to other Mars soil simulants [56], Eifel Lava is a coarser, less cohesive soil with a larger grain size (see Figure 5.3). Key specification figures are listed in Table 5.1 and are taken from [57]. The grain size varies mostly between 1.0 and 4.0 mm.

5.1.2 Tracking System

To accurately measure the position of any mobility system placed in the sand test bed, an infrared tracking system is installed in the PEL. Eight cameras (see Figure 5.4a) are mounted above the test bed, sending out infrared flashes to detect the position of ball-

shaped tracking markers placed on an object, based on time-of-flight measurements. A room calibration of the tracking system was performed right before the beginning of the test campaign according to the documented procedures of the system manufacturer with the global coordinate frame placed as seen in Figure 5.10.

(a) **Camera** (b) **Target**

Figure 5.4: **Tracking system components**

A minimum of two cameras need to detect a marker in order to locate its position. To additionally track the orientation of an object, an arrangement of multiple markers can be defined in the system as a tracking target (see Figure 5.4b), where the markers are positioned in a unique pattern and a local coordinate system is defined. The position and orientation measurements for the tracking targets are broadcast by the tracking server as UDP packets via Ethernet.

5.2 Test Setup

The EXM-BB2 rover was integrated into the PEL facility through power and network connections as well as through the tracking system which tracks the pose of the targets installed on the rover body. Rover configuration and control was performed from a desktop PC in the adjacent control room where the network of modules running on different nodes was monitored. Prior to the tests, the soil in the driving area was prepared. Additionally, two GoPro cameras were installed on the edges of the test bed to record the test runs. Figure 5.5 shows an overview of the test setup and the data connections.

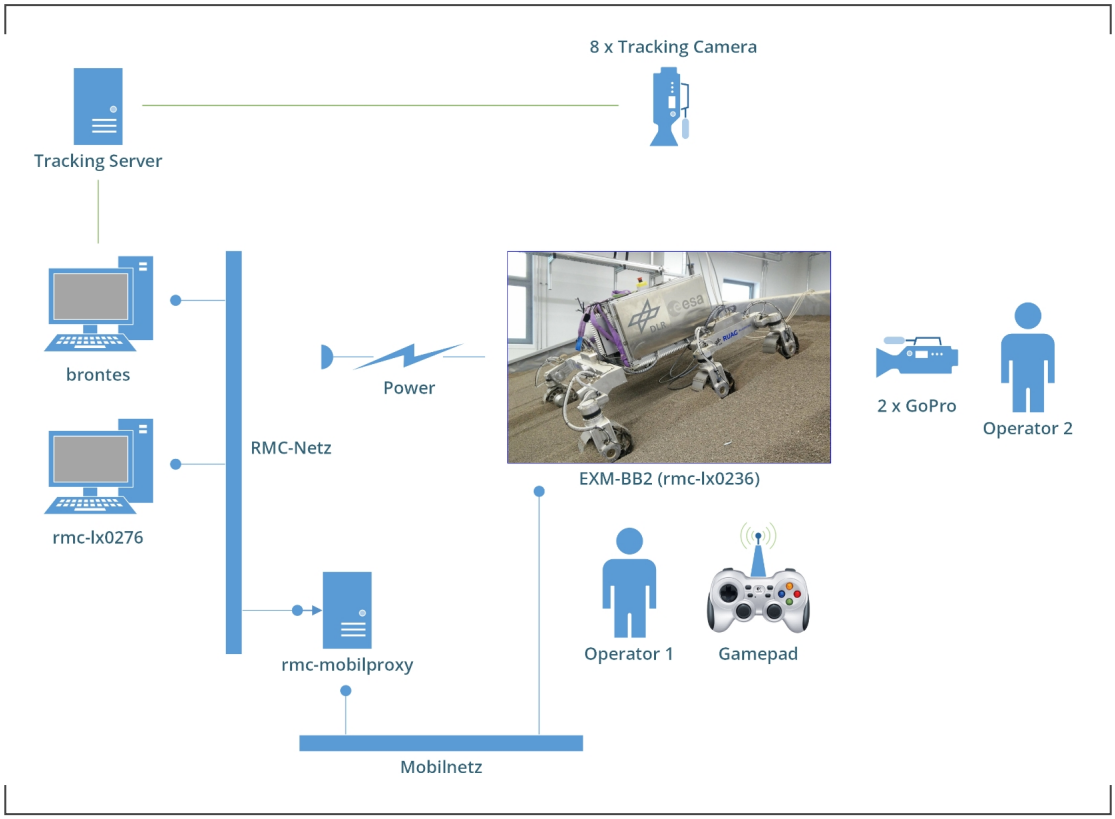

Figure 5.5: **Overview of test setup and data connections**

5.2.1 Tracking Integration

To integrate the EXM-BB2 rover into the tracking system, three tracking targets $\mathcal{T} = \{1, 2, 3\}$ were mounted on the outer aluminium frame of the rover body (see Figure 5.6). The system measures the transformations $\boldsymbol{T}_{T_k}^{G}$ from the target coordinate frame T_k, $k \in \mathcal{T}$ to a global coordinate frame G. The global pose $\boldsymbol{T}_{R,k}^{G}$ of the rover reference frame R can be computed from any one target measurement as

$$\boldsymbol{T}_{R,k}^{G} = \boldsymbol{T}_{T_k}^{G} \boldsymbol{T}_{R}^{T_k} = \boldsymbol{T}_{T_k}^{G} \left(\boldsymbol{T}_{T_k}^{R}\right)^{-1} \tag{5.1}$$

For this, the relative transformation $\boldsymbol{T}_{T_k}^{R}$ is needed. $\boldsymbol{T}_{T_1}^{R}$ was measured by hand as

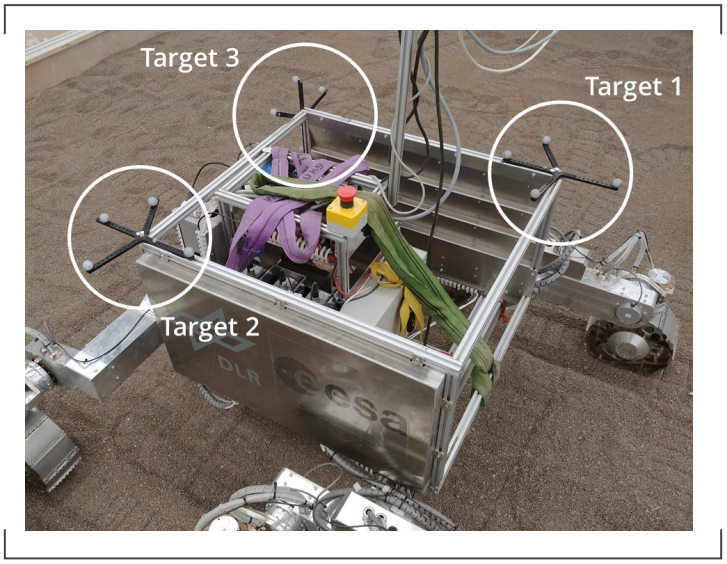

Figure 5.6: **Placement of tracking targets on rover body**

$$\boldsymbol{T}_{T_1}^{R} = \begin{bmatrix} 1 & 0 & 0 & 0 \\ 0 & 1 & 0 & -0.310 \\ 0 & 0 & 1 & -0.420 \\ 0 & 0 & 0 & 1 \end{bmatrix} \tag{5.2}$$

Given the measurements $\boldsymbol{T}_{T_k}^{G}$, $\boldsymbol{T}_{T_2}^{R}$ and $\boldsymbol{T}_{T_3}^{R}$ were then computed as

$$\boldsymbol{T}_{T_k}^{R} = \boldsymbol{T}_{T_1}^{R} \left(\boldsymbol{T}_{T_1}^{G}\right)^{-1} \boldsymbol{T}_{T_k}^{G} \quad \text{for } k \in \{2, 3\} \tag{5.3}$$

resulting in

$$\boldsymbol{T}_{T_2}^{R} = \begin{bmatrix} 1.0000 & 0.0068 & -0.0009 & 0.6852 \\ -0.0068 & 0.9997 & -0.0244 & 0.3081 \\ 0.0007 & 0.0244 & 0.9997 & -0.4123 \\ 0 & 0 & 0 & 1 \end{bmatrix} \tag{5.4}$$

and

$$\boldsymbol{T}_{T_3}^{R} = \begin{bmatrix} 0.0074 & -0.0108 & -0.9999 & 0.6895 \\ 0.0256 & -0.9996 & 0.0110 & -0.3119 \\ -0.9996 & -0.0257 & -0.0071 & -0.3908 \\ 0 & 0 & 0 & 1 \end{bmatrix} \tag{5.5}$$

Data Fusion

The tracking system detects each target separately. To increase tracking accuracy and robustness, the estimated pose of the rover reference frame according to each target measurement can be fused for all valid targets $\mathcal{T}_v \subset \mathcal{T}$. The fused position $\boldsymbol{p}_{R,\text{fused}}^{G}$ of the rover reference frame in global coordinates can simply be computed as the mean of the individual measurements $\boldsymbol{p}_{R,k}^{G}$ as

$$\boldsymbol{p}_{R,\text{fused}}^{G} = \frac{1}{|\mathcal{T}_v|} \sum_{k \in \mathcal{T}_v} \boldsymbol{p}_{R,k}^{G} \quad \in \mathbb{R}^3 \tag{5.6}$$

$\boldsymbol{p}_{R,k}^{G}$ can be directly extracted as the first three elements from the last column of $\boldsymbol{T}_{R,k}^{G}$. Finding a fused orientation on the other hand is not so straight forward. The measured orientation of the rover reference frame according to a single target T_k is given by the rotation matrix $\boldsymbol{R}_{R,k}^{G}$. It can be extracted as the top left 3×3 matrix of $\boldsymbol{T}_{R,k}^{G}$. However, rotation matrices can not simply be averaged. They are elements of the Lie group SO(3) and as such there exists a unique mapping into their tangent space so(3), through the matrix logarithm of $\boldsymbol{R}_{R,k}^{G}$ [58]. In this tangent space (the associated Lie algebra), the measurements can simply be averaged. Afterwards, the average representation can be mapped back to SO(3) through the matrix exponential. Thus, the fused rotation matrix $\boldsymbol{R}_{R,\text{fused}}^{G}$ can be computed as

$$\boldsymbol{R}_{R,\text{fused}}^{G} = \exp\left(\frac{1}{|\mathcal{T}_v|} \sum_{k \in \mathcal{T}_v} \log\left(\boldsymbol{R}_{R,k}^{G}\right) \right) \quad \in \text{SO}(3) \tag{5.7}$$

The fused position and orientation measurements can then be combined into a transformation matrix $\boldsymbol{T}_{R,\text{fused}}^{G}$ as

$$T^{G}_{R,\text{fused}} = \begin{bmatrix} R^{G}_{R,\text{fused}} & p^{G}_{R,\text{fused}} \\ \mathbf{0}_{1\times 3} & 1 \end{bmatrix} \tag{5.8}$$

A python script was written to compute the transformation data $T^{G}_{R,1}$, $T^{G}_{R,2}$, $T^{G}_{R,3}$ and $T^{G}_{R,\text{fused}}$ and publish it as an LN topic.

5.2.2 Initial Soil Preparation

In preparation of the tests, the tub was filled with additional amounts of Eifel Lava soil up to a nominal level of 0.3 m to avoid effects caused by the the bottom of the tub on the soil behavior at the surface. The soil was distributed evenly using a shovel and a flattening tool. Soil close to the surface was loosened up and smoothed using a rake, which was repeated before each test run traversing the same area. Figure 5.7 shows the tools and procedures involved.

(a) **Shovel and flattening tool** (b) **Rake** (c) **After initial soil preparation**

Figure 5.7: **Tools and procedures used for soil preparation**

5.3 Test Plan

A test plan was devised in order to systematically compare and assess the behavior of the driving modes. The tests were grouped into six categories:

- Obstacle Tests (OBS) to show the general functionality of the kinematic model and the contact angle estimation through force-torque sensors by driving over a stone

and observing the behavior of the rover body and the joint rates. Figure 5.8 shows the stone with approximate dimensions of 0.20 x 0.15 x 0.10 m (length x width x height).

Figure 5.8: **Stone obstacle for OBS tests**

- Balancing Platform Tests (BLP) to analyze the behavior of the rover body while driving with one side on a raised platform using the Balancing mode. It was created out of polystyrene boards with an 18° on- and off-ramp. Since the wheel-soil interaction was of no interest during these tests, the platform was only covered with a thin layer of soil. The platform and its main dimensions can be seen in Figure 5.9.

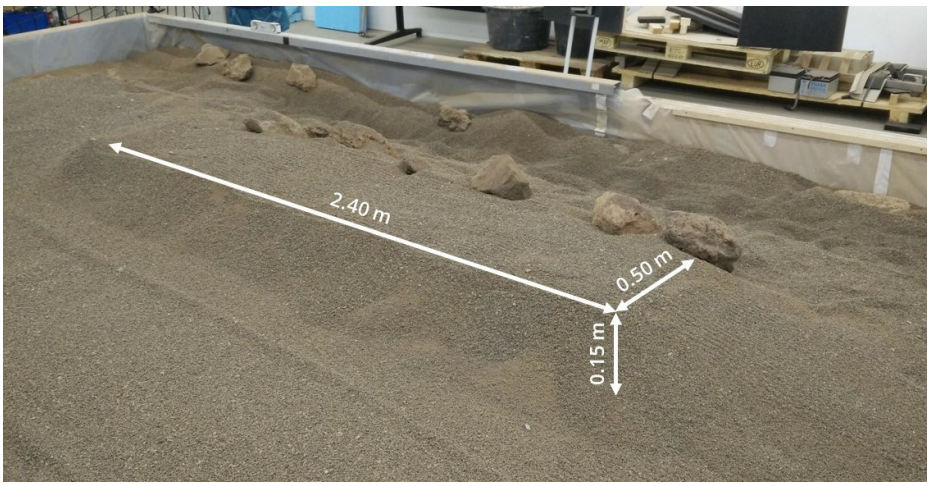

Figure 5.9: **Raised platform for BLP tests**

- Balancing Sideways Slope Tests (BLS) to analyze potential benefits of the Balancing Mode while driving sideways along a slope with the aim of decreasing sideways slip.

- Wheel Walking Comparison Tests (WWC) to compare Normal Driving (ND) with multiple Wheel Walking gaits for the full-body kinematic model (FB) and the simplified implementation as well as different swivel angles while driving up a slope. Normal Driving is a basic driving mode where the walking joints are kept in their nominal position and all wheels are turning at a constant rate. These tests were performed at a slope angle γ of 18° which was still manageable but challenging for Normal Driving.

- Wheel Walking Traversability Tests (WWT) to assess the behavior of Wheel Walking when Normal Driving fails. These were conducted at a slope angle γ of 21° and only using the implementation based on the kinematic model. Additionally, the benefits of enabling the burnout motion (BO) were tested.

- Wheel Walking Extreme Tests (WWX) to work out the maximal capabilities of Wheel Walking on a slope by finding the maximally traversable slope angle γ and trying out additional gait combinations.

The parameter combinations tested in each category are listed in Tables 5.2 and 5.3.

5.4 Test Procedures

During the tests, the following procedures were followed to ensure the validity of the test results:

- In general, before traversing the same terrain area twice, the soil surface was loosened up and flattened using a rake to ensure repeatable results.

- While driving on the slope, soil tends to be moved down the ramp, thus decreasing the true slope angle. After a maximum of two test runs, soil was shoveled back towards the top of the slope and flattened to compensate this effect.

- During all test runs, the rover was kept at a distance > 0.5 m from the sides of the tub to avoid any effects on soil behavior.

Table 5.2: **Obstacle, Balancing Platform and Balancing Sideways Slope Tests**

Test Group ID	γ (°)	$v^R_{x,\text{des}}$ ($\frac{\text{m}}{\text{s}}$)	Gait	k_W	k_Θ	k_Φ	k_μ
OBS-01	0	60	Normal Driving	N/A	N/A	N/A	N/A
OBS-02	0	60	Balancing	32	128	128	1
BLP-01	0	60	Normal Driving	N/A	N/A	N/A	N/A
BLP-02	0	60	Balancing	2	128	128	1
BLS-01	15	40	Normal Driving	N/A	N/A	N/A	N/A
BLS-02	15	40	Balancing	2	128	128	1

Table 5.3: **Wheel Walking Comparison, Traversability and Extreme Tests**

Test Group ID	γ (°)	$v^R_{x,\text{des}}$ ($\frac{\text{m}}{\text{s}}$)	Gait	$\varphi_{W_{\text{min}}} \rightarrow \varphi_{W_{\text{max}}}$
WWC-01	10	20	Normal Driving	N/A
WWC-02	15	20	Normal Driving	N/A
WWC-03	18	20	Normal Driving	N/A
WWC-04	18	40	Normal Driving	N/A
WWC-05	18	60	Normal Driving	N/A
WWC-06	18	20	ABA simple	$4 \rightarrow 34$
WWC-07	18	20	KRU simple	$4 \rightarrow 34$
WWC-08	18	20	ABA simple	$4 \rightarrow 19$
WWC-09	18	20	ABA full body	$4 \rightarrow 34$
WWC-10	18	20	KRU full body	$4 \rightarrow 34$
WWC-11	18	20	ABA full body	$4 \rightarrow 19$
WWT-01	21	20	Normal Driving	N/A
WWT-02	21	20	ABA full body	$4 \rightarrow 34$
WWT-03	21	20	KRU full body	$4 \rightarrow 34$
WWT-04	21	20	ABA full body	$4 \rightarrow 19$
WWT-05	21	20	ABA full body + burnout	$4 \rightarrow 34$
WWX-01	26	20	ABA full body + burnout	$4 \rightarrow 34$
WWX-02	30	20	ABA FB $\rightarrow$ KRU FB + BO	$4 \rightarrow 34$
WWX-03	30	20	KRU FB $\rightarrow$ KRU FB + BO	$4 \rightarrow 34$
WWX-04	30	20	KRU full body + burnout	$4 \rightarrow 34$
WWX-05	30	$60 \rightarrow 20$	ND $\rightarrow$ KRU FB + BO	$4 \rightarrow 34$
WWX-06	30	20	KRU simple + burnout	$4 \rightarrow 34$
WWX-07	30	20	KRU full body + burnout	$4 \rightarrow 34$
WWX-08	30	20	HYB simple + extended BO	$4 \rightarrow 19$
WWX-09	30	20	HYB simple + extended BO	$4 \rightarrow 19$

- Power and network connections were suspended from the overhead crane to provide strain relief and to keep the cables away from terrain and wheels.

- Before each run, the active rover joints were brought to their nominal (zero) position.

- For each test, log data and video footage were recorded and the validity of a run and any additional comments were noted. Log data includes driving mode parameters, commanded and measured joint speeds and positions, force-torque sensor and IMU measurements, motor controller power consumption and tracking system data.

- For the OBS tests, the rover was driven forwards on flat ground with a stone placed in front of the front-right wheel (see Figure 5.8).

- For the BLP tests, the rover was driven forwards along the raised platform (see Figure 5.9).

- For the BLS tests, the rover was driven sideways along the slope with its heading aligned with a yaw angle of 90° before starting each test run.

- For the WWC, WWT and WWX tests, the rover was driven up the slope at a constant desired body velocity. Since the length of the ramp in the PEL is relatively short (roughly two times the body length of the EXM-BB2 rover), the test runs start at the bottom of the ramp in flat terrain and transition into the slope. The result plots are based on the data gathered in the *measurement zone* (see Figure 5.10). Prior to each test run, the rover heading was adjusted to match a yaw angle of 0° according to the tracking system data, thus driving straight towards the slope along the path with highest inclination.

- A key indicator for traversability performance for the WW tests is the body slip ratio $\upsilon_{x,\text{body}}$, which is defined here by the ratio of the currently measured forward velocity in rover body x-direction and the achievable forward rover body velocity in flat terrain:

$$\upsilon_{x,\text{body}} = 1 - \frac{v^R_{x,\text{cur}}}{v^R_{x,\text{flat}}} \tag{5.9}$$

  $v^R_{x,\text{flat}}$ is assessed at the beginning of each run while driving through the flat terrain area (in the *calibration zone*, see Figure 5.10).

- All BLP, BLS, WWC and WWT tests were repeated three times to ensure consistent results and detect outliers. The OBS and WWX tests were only performed once. The OBS tests were functional behavior tests with no need for accurate quantifiable results. The WWX tests were aimed at exploring the capability boundaries and provide directions for future tests.

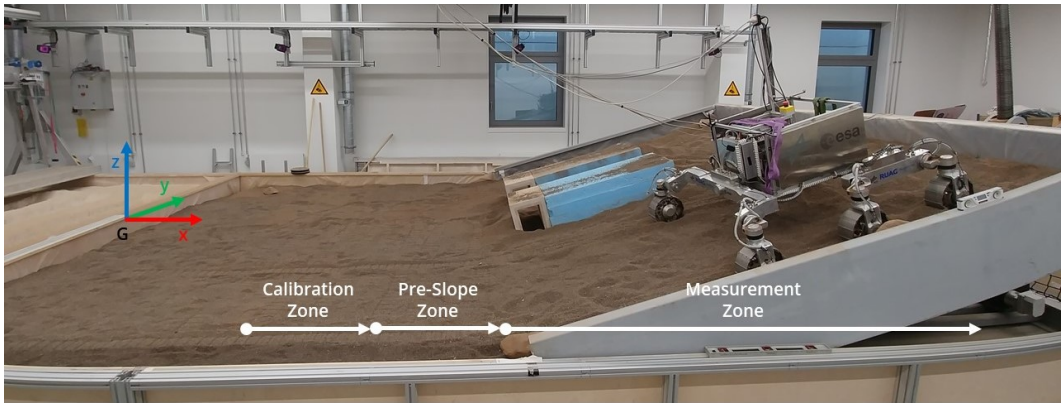

Figure 5.10: **Global tracking coordinate system and driving zones for slope tests**

6 Results

This chapter presents the results from the two-week test campaign carried out in DLR's Planetary Exploration Laboratory. The experimental setup and the test procedures are described in the previous chapter. The results are presented in three subsections:

1. Verification tests to show the general functionality of the kinematic model, the validity of the test setup and the reasoning behind the test plan

2. Balancing tests to assess the benefits of this locomotion mode when driving in uneven terrain regarding side-slip and body tilt

3. Wheel Walking tests to compare the traversability performance to Normal Driving without actuation of the walking joints and analyze the impact of various parameters

All plots in this chapter were generated from the log data recorded from the tracking system and the rover. In each plot, the test IDs of the corresponding test runs are given. The set of parameters used for the test runs can be looked up in the respective table in Section 5.3.

6.1 Verification Tests

6.1.1 Obstacle Test

For the Obstacle Test, the rover was driven on otherwise flat and even terrain with the right-side wheels of the rover passing over a stone with a height of slightly less than the wheel radius (see Figure 5.8). The aim of this test was to validate the functionality of the kinematic model and the contact angle estimation through the force-torque sensors (see Section 4.1.2). Figure 6.1 shows the progression of the estimated contact angle $\varphi_{A,\text{est}}$ and the reaction of the kinematic model through the walking joint angle for the right-side

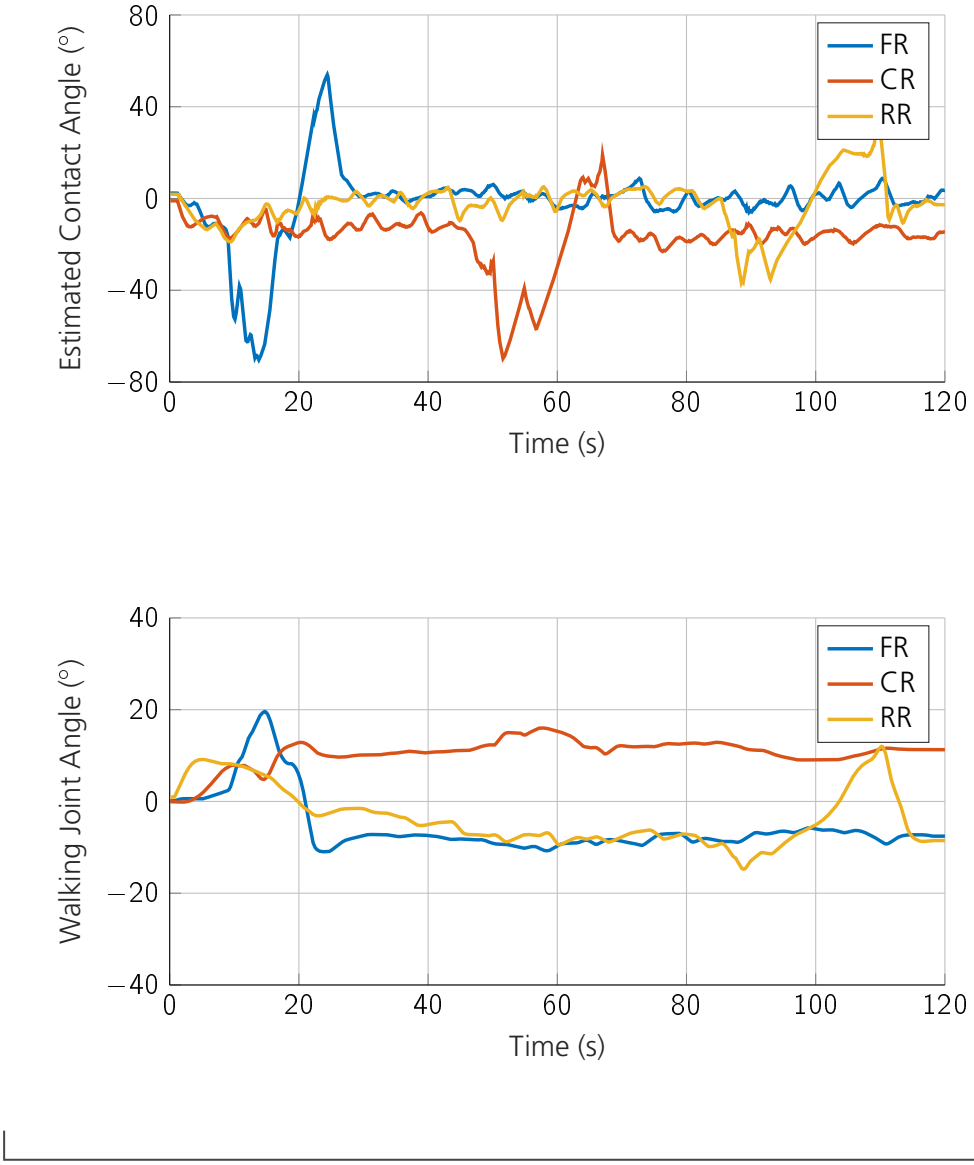

Figure 6.1: **Plots of the OBS-02 obstacle test for the right side wheels – driving over a stone using the kinematic model. Top: Estimated contact angle over time. The spikes clearly mark the time ranges when the wheels pass over the stone. Bottom: Reaction of the walking joint angles over time. Front and rear walking joints adjust accordingly by tilting backwards, center leg is already tilting backwards due to the bogie joint motion.**

wheels. The points in time when the wheels encounter the stone can clearly be deduced from the spikes in the plot. The values pass from a negative to a positive contact angle, corresponding to the wheel-terrain contact point moving from the front of the wheel to the back while passing over the stone. For the front and rear wheel, the rover increases the walking joint angle φ_W and tilts the leg backwards to accommodate for the change in travel direction when climbing the obstacle. For the center wheel, the leg is already moved backwards by the bogie motion when being pushed upwards, and no change in the walking joint angle is necessary.

6.1.2 Slip vs. Slope Angle

The traversability performance of the Wheel Walking locomotion mode was assessed by driving on a slope to simulate similar challenges on Mars. Slip is expected to increase with the terrain inclination. To choose the slope angle γ to use for the Wheel Walking tests, the performance of Normal Driving was evaluated at a range of slopes. Figure 6.2 shows the travel distance over time and the evolution of the slip ratio for each test. It can be seen that the slip ratio tends to plateau towards the end of the travel distance, indicating the approach of a steady state.

For the WWC tests, the aim was to find a slope angle where Normal Driving was still capable of traversing the slope, but at a high slip ratio to bring out the differences between the driving modes. The WWT tests were aimed to be carried out at a slope angle where Normal Driving started to clearly fail. Failing is defined here as reaching one of the following conditions:

- A permanent slip ratio above 90%
- Wheel sinkage to a point where soil reaches the wheel hub at half the wheel diameter, risking damage to the rover

A high slip ratio typically goes hand in hand with high wheel sinkage. Corresponding to the results, the slope angle for the WWC tests was chosen as 18° where the slip ratio stays just below 90%. The slope angle for the WWT tests was chosen as 21° where the slip ratio permanently stays above 90%. The plots of the 21° run end at the point where wheel sinkage became to high to continue safely.

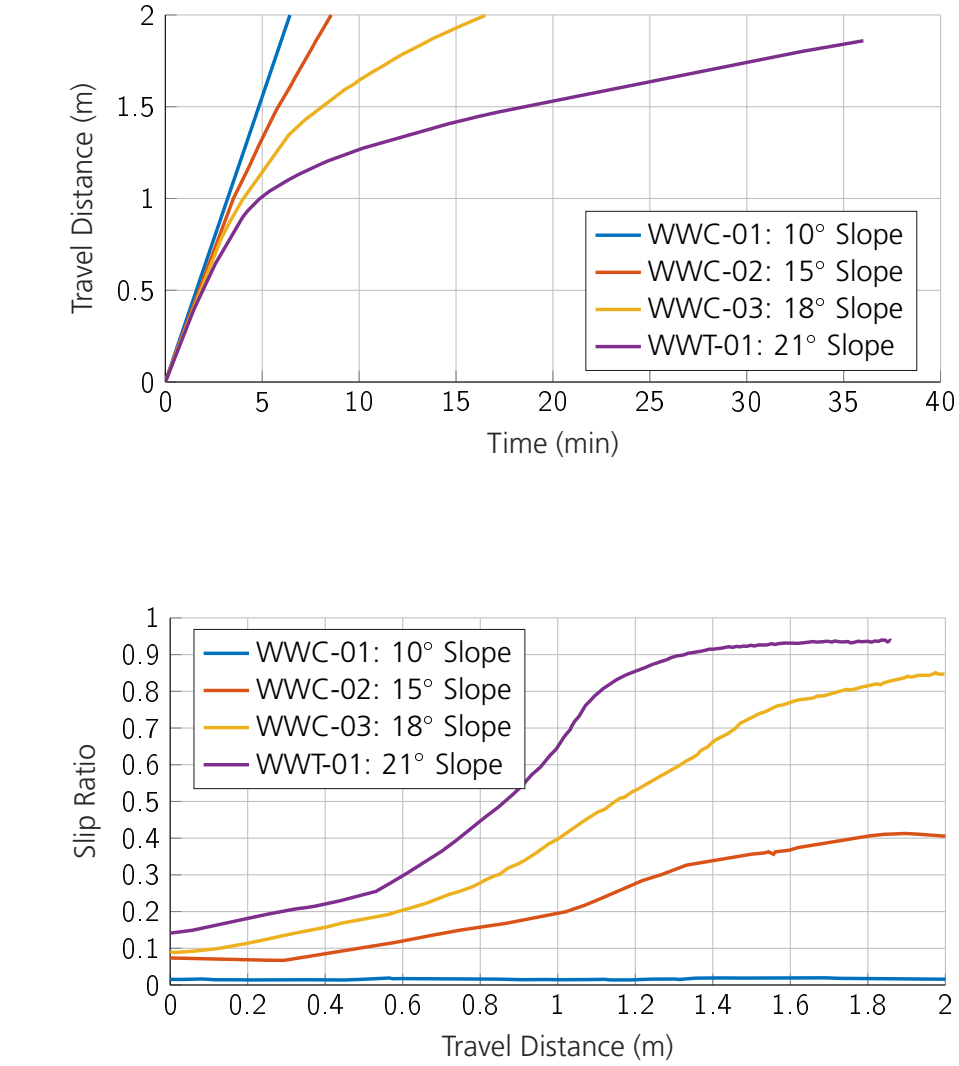

Figure 6.2: **Plots of Normal Driving with 20 m/h commanded body speed at various slope angles. Top: Travel distance over time. Steeper plots indicate higher slip at higher slope angles. Bottom: Slip ratio over travel distance. All plots tend to plateau towards a steady state at the end. At 10° slope, slip is almost unnoticeable, but increases quickly to over 90% for 21° slope where the run had to be stopped due to excessive sinkage.**

6.1.3 Speed Slip Independence

For the Wheel Walking tests, a common body speed of 20 $\frac{m}{h}$ was selected for all gaits. However, the average wheel rotation speeds differ depending on the number of phases of a gait. To confirm the assumption that slip is independent of wheel speed in the test environment, the rover was driven up a slope at an inclination γ of 18° at 20, 40 and 60 $\frac{m}{h}$ using the Normal Driving mode. Figure 6.3 shows the travel distance over time and the evolution of the slip ratio during the runs. The variation of the slip ratio stays below 10 percentage points between the runs over the course of the travel distance, in line with the assumption. Additionally, this test shows a good repeatability of the test results.

6.2 Balancing Tests

The aim of the Balancing Mode is to keep the rover body leveled and increase its static stability by making use of the walking joint actuators through the kinematic model. The mode was evaluated through two sets of tests:

1. Driving on flat terrain with one side of the rover along a raised platform
2. Driving cross-slope along the ramp at an inclination of 15° to test side-slip stability

6.2.1 Raised Platform

To assess the capability of the Balancing Mode to keep the rover body leveled, a raised platform was built (see Figure 5.9) to drive along with one side of the rover on top. Figure 6.4 shows the progression of the rover body pitch and roll angles Θ and Φ while driving along the platform. The target function of the Balancing Mode tries to keep these values close to zero. As can be seen from the plots, both body pitch and roll are reduced by over 60% compared to Normal Driving and are kept below an absolute value of 3° over the entire length of the travel distance. Figure 6.6 (top) shows the progression of the walking joint angles over time, which are kept below $\pm$ 50° at all times.

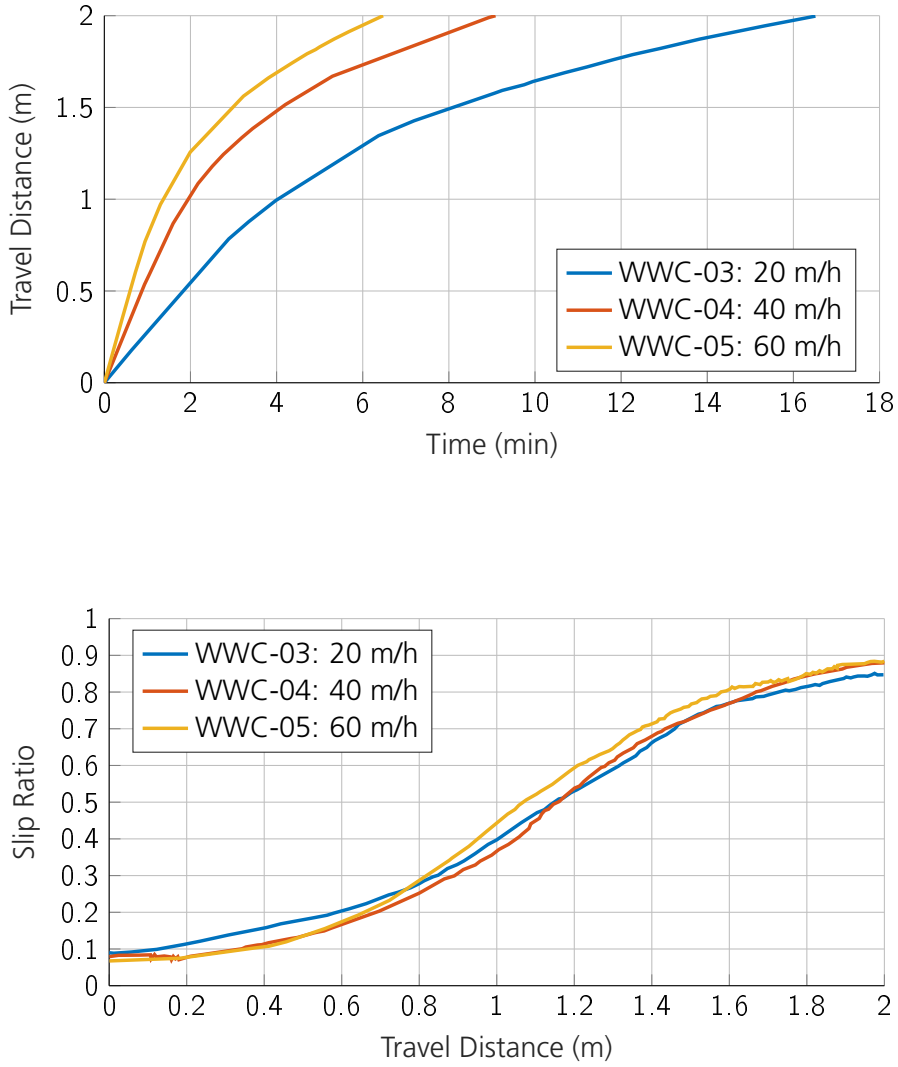

Figure 6.3: **Plots of Normal Driving at various driving speeds on an 18° slope to validate the assumption that slip is independent of commanded driving speeds. Top: Travel distance over time. Bottom: Slip ratio over travel distance. Slip measurements are within 10 percentage points of each other over the whole distance, confirming the assumption.**

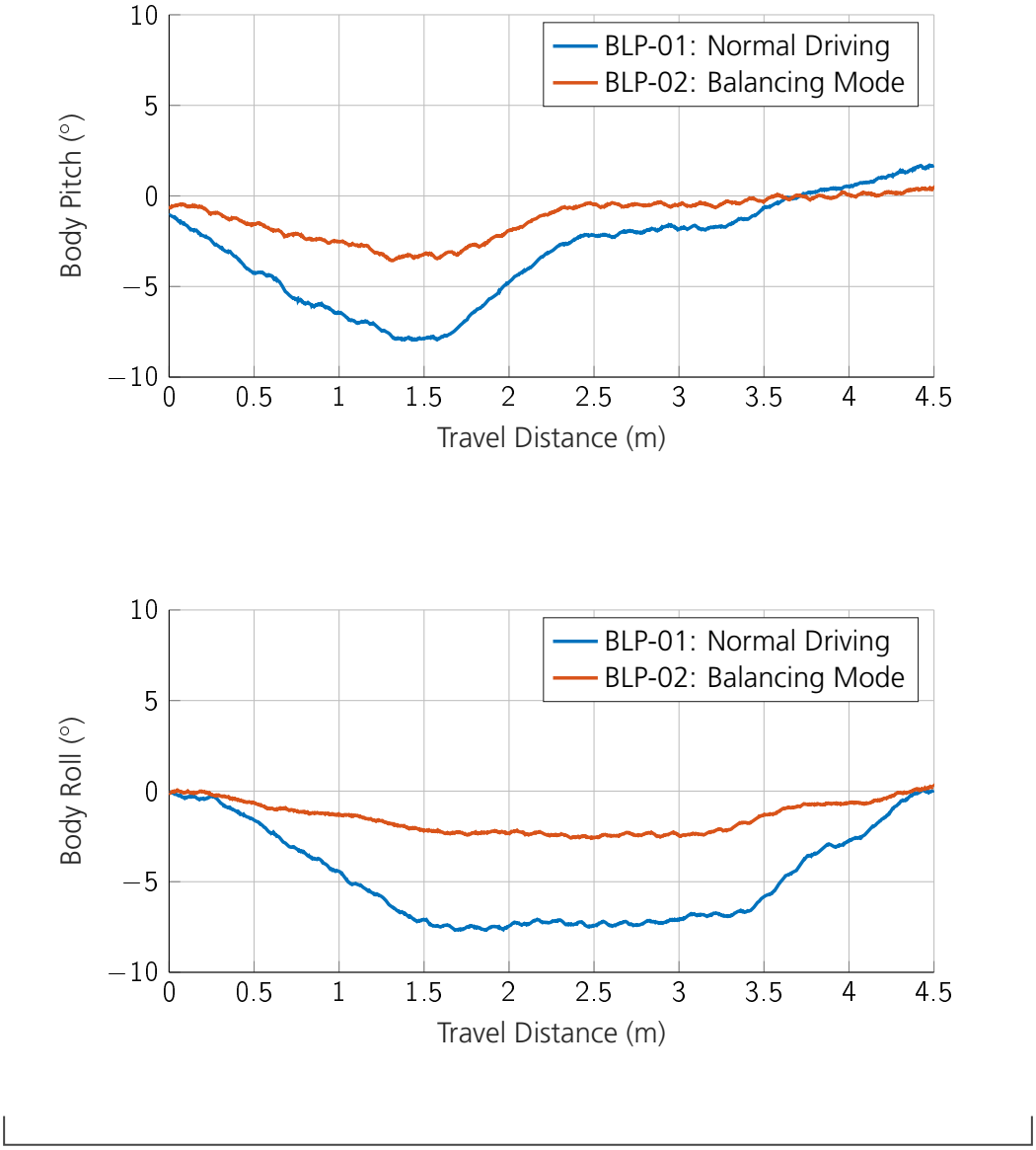

Figure 6.4: **Plots of one-sided raised platform driving to evaluate the Balancing locomotion mode. Top: Body pitch over travel distance along the platform, comparing Normal Driving to Balancing. The pitch angle is reduced over the whole travel distance by more than 50% using Balancing. Bottom: Body roll over travel distance along the platform, with similar observations.**

6.2.2 Side-Slip Stability

The performance of the Balancing Mode while driving cross-slope is evaluated through the lateral path deviation. Ideally, the rover should traverse the width of the slope without sliding towards the bottom. The results for the Balancing Mode compared to Normal Driving are shown in Figure 6.5 (top). The ratio of longitudinal and lateral travel at the end of the travel distance is at 30% for Normal Driving compared to 13% for the Balancing Mode. Thus, by enabling Balancing, the lateral deviation over a longitudinal travel distance of 2.4 meters is reduced by more than 50%. Figure 6.5 (bottom) additionally shows the effect of the Balancing Mode on the body roll angle Φ. Its absolute value is decreased from 15° on average to below 10°. This is achieved through the motion of the walking joints which are used to spread out the legs on the right side of the rover (the up-slope side). Figure 6.6 (bottom) shows the progression of the walking joint angles over time, which are kept below $\pm$ 60° at all times.

6.3 Wheel Walking Tests

The Wheel Walking tests were conducted on a slope as described in Section 5.4. Overall, comparisons between Normal Driving, the Axle-by-Axle and the Kruse gait were performed (see Section 4.3.1 for a description), as well as between the implementation based on the full-body kinematic model (see Section 4.3.2) and the simplified implementation (see Section 4.3.3). Additionally, the impact of an additional burnout phase and of changes to the swivel angle were investigated as well as power consumption and performance at extreme slope angles.

Results are mainly presented as plots displaying travel distance over time and slip ratio over travel distance. For the former plots, when including the simplified Wheel Walking implementation, the travel distance is normalized to a common rover body velocity of 20 $\frac{m}{h}$ in the calibration zone, since the desired body velocity for the simple wheel walking implementation can not be set exactly. In the latter plots, the slip ratio typically rises from left to right while the rover is transitioning into the slope and settles at a steady state when reaching the end of the travel distance.

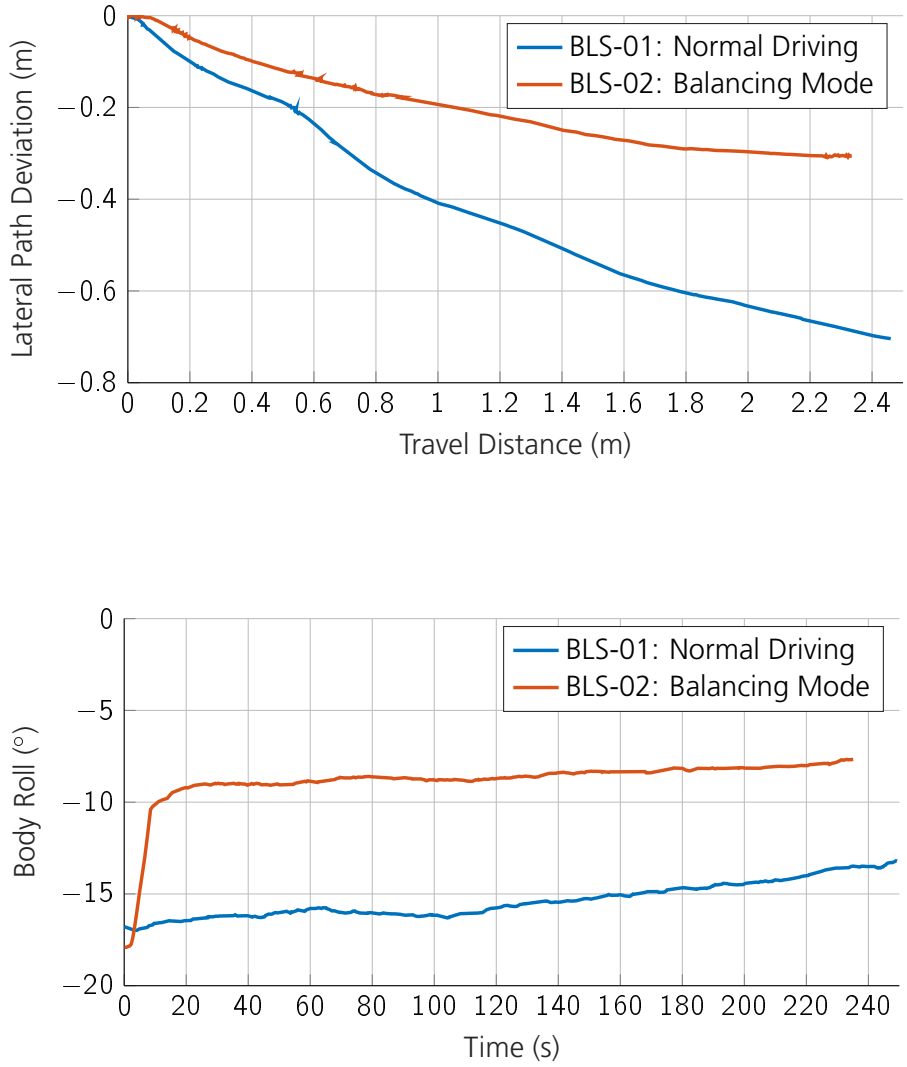

Figure 6.5: **Plots of cross-slope driving to evaluate the Balancing locomotion mode. Top: Lateral path deviation over travel distance, comparing Normal Driving to Balancing. Side-slip is reduced by more than 50% using Balancing. Bottom: Body roll angle over travel distance, reduced by over 5° to below 10° for the whole travel distance.**

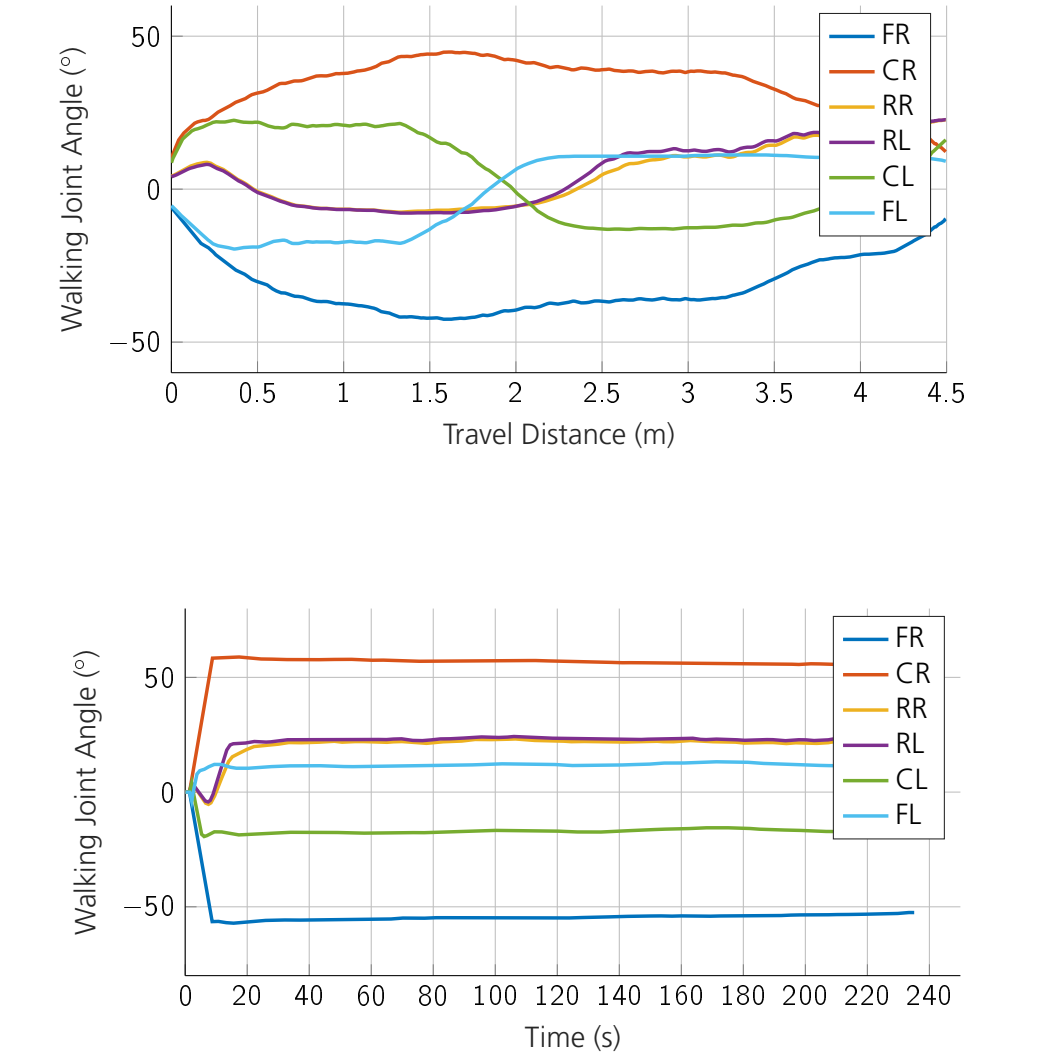

Figure 6.6: **Plots of walking joint behavior using Balancing. Top: Progression of walking joint angles over travel distance for one-sided raised platform driving. Angles of front-right and center-right wheel go up to ±50° to achieve the reduction in body pitch and roll. Bottom: Progression of walking joint angles over time for cross-slope driving. Angles of front-right and center-right wheel go over ±50° to reduce body roll.**

6.3.1 Gait Comparison

Figure 6.7 shows the performance of Normal Driving compared to the Axle-by-Axle and the Kruse gait, both for the simplified and the full-body kinematics implementation. Reaching the end of the travel distance, the slip ratios of all Wheel Walking runs lie more than 20 percentage points below the slip ratio of Normal Driving. Looking at the individual gaits, the Axle-by-Axle gait shows a consistently lower slip ratio than the Kruse gait, for both implementations. Comparing the simplified and the full-body kinematics implementation of Wheel Walking, both the Axle-by-Axle run and the Kruse run using full-body kinematics reach the end of the travel distance sooner than their counterparts. However, analyzing the slip ratio, this is mainly due to higher slip of the simplified implementation in the flatter regions when transitioning into the slope. Progressing up the slope, slip ratios of the full-body implementations increase more steeply and in the end the trend reverses, with the slip ratios of the simplified implementations dropping below the others.

6.3.2 Impact of Additional Parameters

Additionally investigated parameters were the swivel angle of the walking joints and the introduction of an additional burnout phase. The default swivel angle in all tests is set to span a range of 30°, with the walking joints rotating from $\varphi_{W,\text{min}} = 4°$ to $\varphi_{W,\text{max}} = 34°$ for the front wheels and the corresponding negative values for the center and back wheels. This is due to the walking joint rotation constraints of the ExoMars rover (see Section 2.1.3). To analyze the impact of the swivel angle on body slip, a second configuration was tested, with the walking joint angles rotating with an amplitude of 15° from $\varphi_{W,\text{min}} = 4°$ to $\varphi_{W,\text{max}} = 19°$. Additionally, the effect of an additional burnout phase (see Section 4.3.1) was tested, where the wheels dig into the ground to increase traction. All of these tests were performed using the Axle-by-Axle full-body kinematics implementation.

As can be seen from Figure 6.8, halving the swivel angle degrades the performance in terms of slip by around 5 percentage points over the entire travel distance or about one third of the slip advantage of Axle-by-Axle Wheel Walking over Normal Driving. The impact of the burnout phase is more noticeable, but the effect only starts to appear at higher inclinations after transitioning into the slope. Looking at the end of the travel distance, the slip ratio dropped from 80% to 60% compared to no burnout.

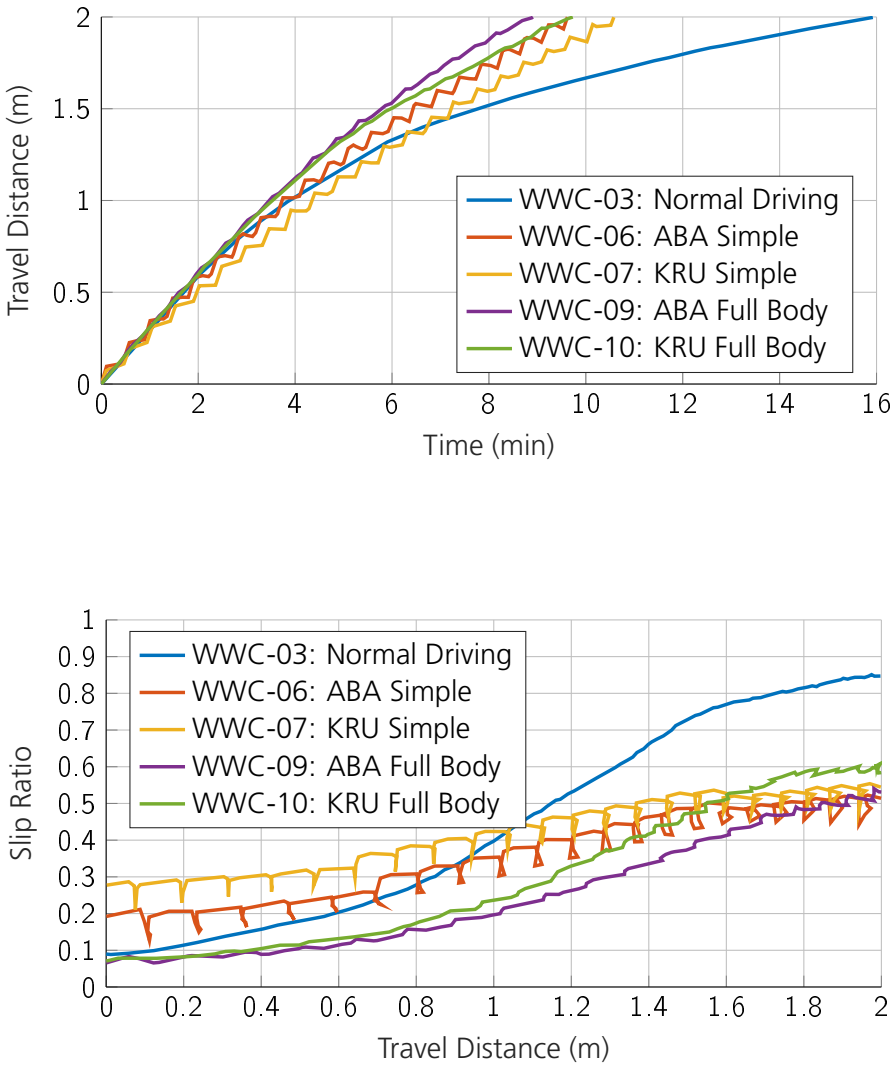

Figure 6.7: **Plots of Normal Driving compared to different WW gaits and implementations on an 18° slope. Top: Travel distance over time. Normal Driving takes double the amount of time to complete the full distance. The ridges in the plot of simplified WW are caused by the separate body motion phase. Bottom: Slip ratio over travel distance. All WW modes outperform Normal Driving. Jags in the simplified Wheel Walking plots are caused by passing over the same area twice after sliding backwards.**

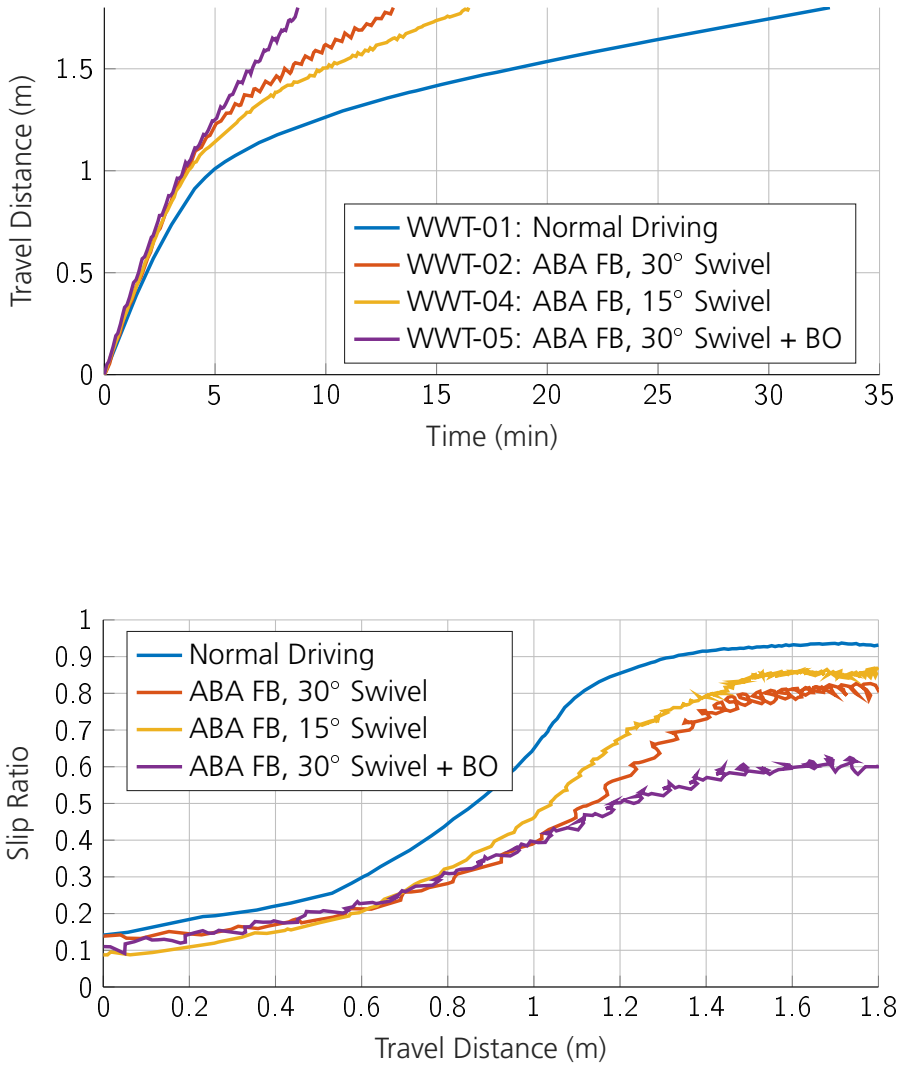

Figure 6.8: **Plots of Normal Driving compared to Axle-by-Axle Wheel Walking with different swivel angles and activated burnout motion. Top: Travel distance over time. The difference between 30° and 15° swivel angle is small compared to the advantage brought by the burnout motion. Bottom: Slip ratio over travel distance. Halving the swivel angle slightly increases slip by 5 percentage points. The burnout motion is advantageous further up the slope at higher body inclinations.**

6.3.3 Power Draw and Energy Consumption

A major constraint for planetary rovers is power consumption. For rovers like ExoMars, energy generated through the solar cells must be carefully managed to maximize its utility during a day. Thus, in addition to overall traversability performance, the energy efficiency of the rover locomotion modes are of interest. During all test runs, power consumption of the motor controllers was recorded for all joint motors combined.

Figure 6.9 (top) shows the instantaneous power consumption of Normal Driving at different speeds as well as for both implementations of the Axle-by-Axle gait at an 18° slope. Higher driving speeds and higher inclinations increase power draw but also reduce the time needed to complete the travel distance (indicated by the end of each line). At comparable body speeds ($\approx 20\ \frac{m}{h}$), power consumption for Wheel Walking locomotion is between 10 to 15% higher than for Normal Driving, which can be expected due to additionally actuated joints. The power draw of the simple Wheel Walking implementation shows more fluctuation than the full body kinematics implementation, but on similar levels.

Figure 6.9 (bottom) shows the energy consumption given as the accumulated power draw. For Normal Driving, higher speeds consume less energy due to the shorter travel time. For Wheel Walking, lower slip leads to shorter travel times and thus less energy consumption. Even though the instantaneous power draw is higher, over the total travel distance both Wheel Walking implementations only use approximately 50% of the energy needed for Normal Driving at $\approx 20\frac{m}{h}$ body speed. Increasing the speed for Normal Driving lowers the energy consumption to similar levels, however, the slopes of the curves indicate that Wheel Walking remains beneficial in any case over longer travel distances.

Similar observations can be gained from Figure 6.10 for the additional burnout motion. In general, power draw is higher, since the additional phases must be compensated by increased joint speeds to achieve a similar desired body velocity. However, due to the significantly decreased body slip at higher inclinations, burnout proves advantageous over longer travel distances and energy consumption is further reduced.

6.3.4 Extreme Slope

On top of the regular Wheel Walking tests (WWT and WWC), some additional test runs were carried out to find the maximum slope angle at which a traverse was still achievable and to explore some additional parameter variations. Each WWX test was just run once and should only serve as an indication on the capabilities of Wheel Walking. The tests were

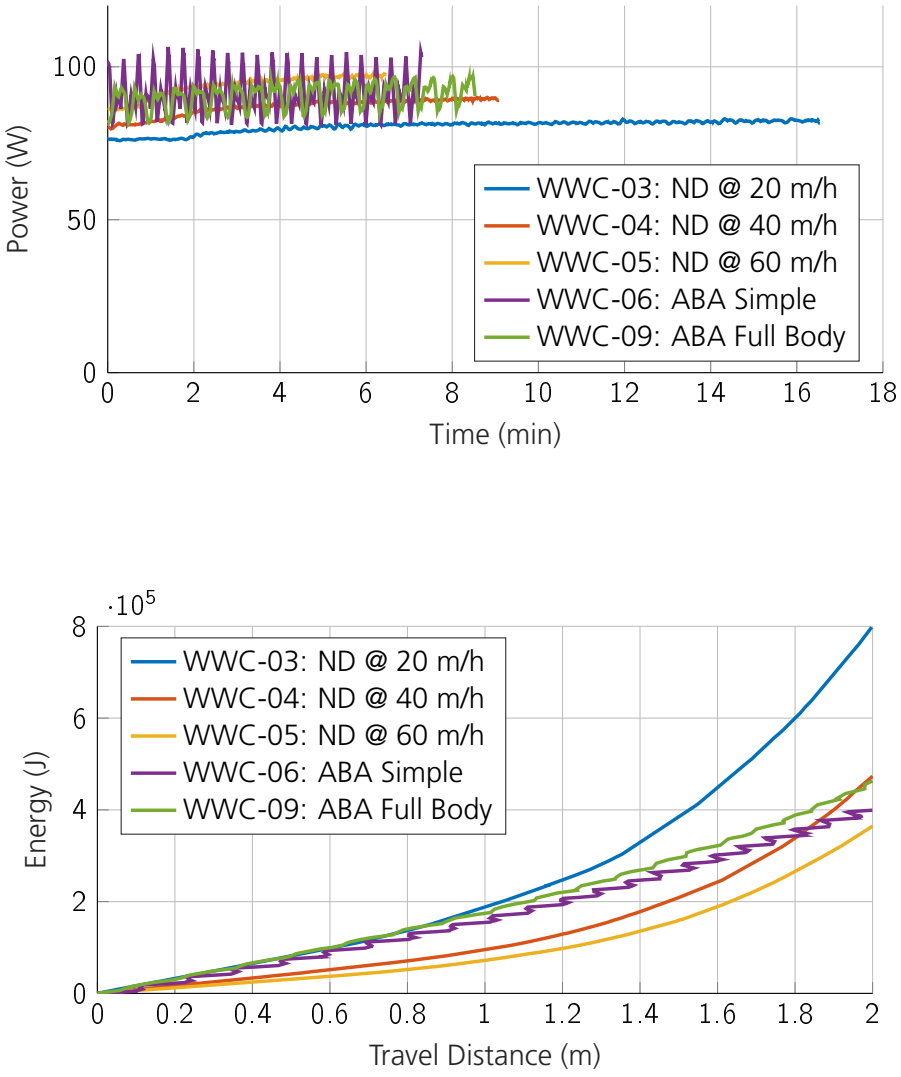

Figure 6.9: **Plots of power draw and energy consumption for Normal Driving and Wheel Walking at 18° slope. Top: Power draw over time. Power draw slightly increases for faster commanded driving speeds. Wheel Walking draws 10 to 15% more power at similar driving speeds, but completes the travel distance significantly faster due to lower slip. Bottom: Energy consumption over travel distance. Wheel Walking uses half of the energy of Normal Driving at similar driving speeds.**

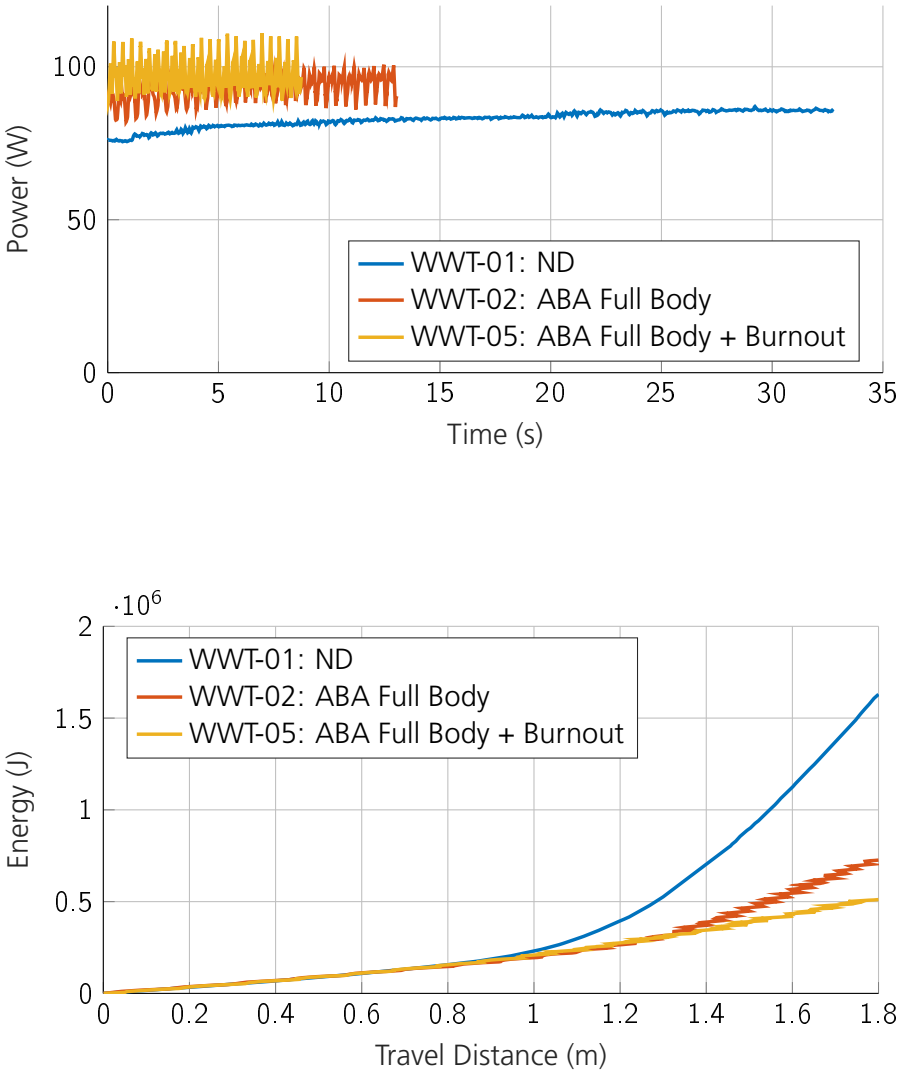

Figure 6.10: **Plots of power draw and energy consumption for Normal Driving, Wheel Walking and Wheel Walking with burnout at 21° slope and 20 m/h commanded driving speed. Top: Power draw over time. Burnout slightly increases power draw, but completes the travel distance significantly faster. Bottom: Energy consumption over travel distance. Burnout further reduces energy consumption at higher inclinations due to decreased body slip.**

limited by the capabilities of the facility with a maximum ramp inclination of 30°. At this slope angle, the Axle-by-Axle gait failed to complete a run due to excessive sinkage (WWX-02). However, traversal was still possible after switching to the Kruse gait, indicating an advantage of this gait at higher slope angles.

Taking into account the conclusions and observations of the previous tests, a new gait was introduced (the Hybrid gait), with the aim of combining the advantages of the Axle-by-Axle and the Kruse gait. It splits the first phase of the Kruse gait into two phases and moves the front and center axle forward separately (see Table 4.4 for the active wheel sequence). Additionally, the length of the burnout phase was quadrupled to increase the dig-in effect. Figure 6.11 shows the results of this final run. At a slope angle of 30°, this combination manages to traverse the slope with a steady-state slip ratio of approximately 70%, 20 percentage points below the Kruse gait with regular burnout length.

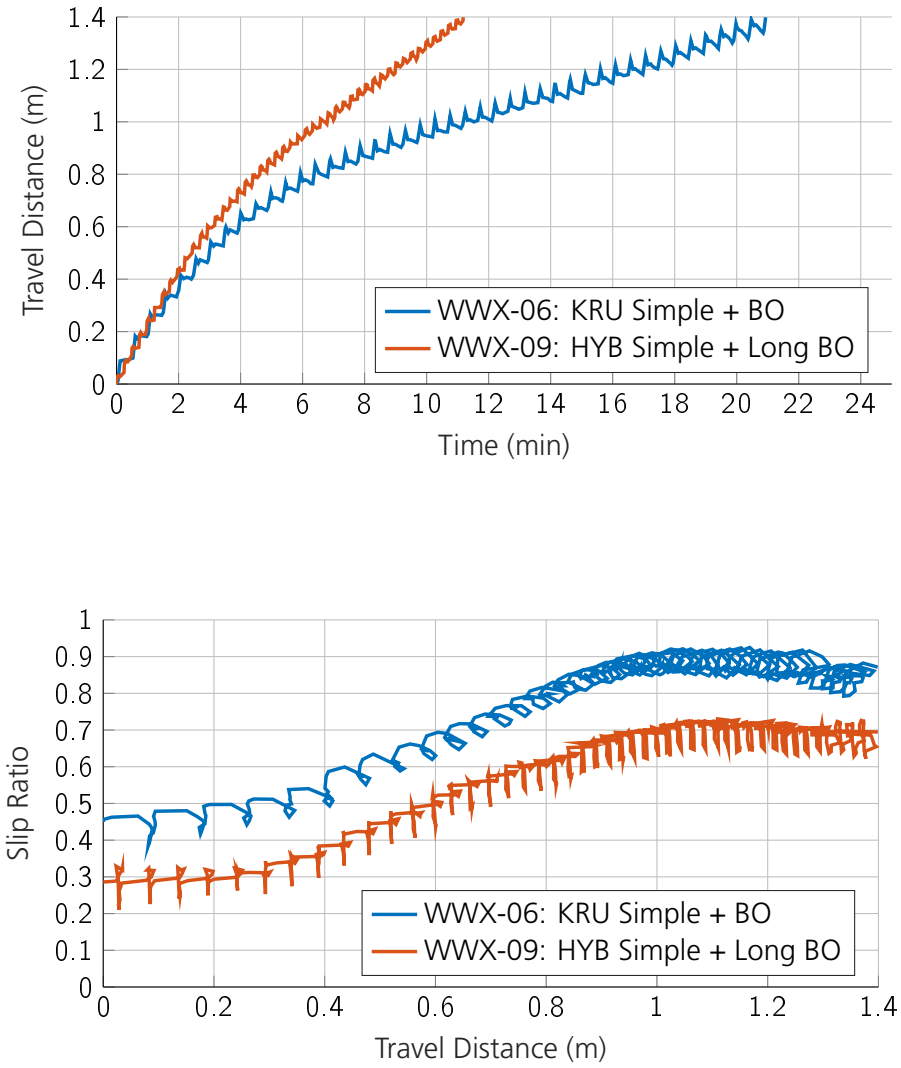

Figure 6.11: **Plots of WW with Kruse gait compared to WW with Hybrid gait and an extended burnout phase at 30° slope. The Hybrid gait was introduced to combine advantages of Axe-by-Axle and Kruse gait. Top: Travel distance over time. The new gait sequence takes only about half the time to cover the travel distance. Bottom: Slip ratio over travel distance. The Hybrid gait with extended burnout climbs the 30° slope with 70% slip.**

7 Discussion

In the previous chapter, the results of the test campaign were presented. During these tests, the full-body kinematic model implementation and, based on this, two locomotion modes for driving on rough terrain were evaluated for the EXM-BB2 rover. These locomotion modes are aimed to take advantage of the additional degrees of freedom offered by the deployment joints in the ExoMars rover's kinematic configuration: Balancing is meant to increase tip-over stability, reduce rover body tilt and reduce side-slip while driving along slopes. Wheel Walking is intended to increase traversability performance by reducing body slip while driving up slopes, increasing the maximally traversable slope angle, reducing wheel sinkage on soft soils and providing increased traction in entrapment situations.

In an initial set of verification tests (see Section 6.1), the general behavior of the kinematic model was verified. The contact angle estimation through the force-torque sensors installed at the wheel hubs provided plausible values and the kinematic model reacted accordingly. Additionally, for Normal Driving without using the walking joints, a maximum slope climbing capability below 21° on Eifel Lava soil could be determined. The slip ratio was verified to be velocity independent.

During the Balancing tests (see Section 6.2), a significant reduction in roll and pitch angle of the rover body of over 60% could be achieved while driving with one side of the rover along a raised platform. This could be useful for fulfilling tilt limits of experiments while being able to traverse steeper terrain. The mode proved additionally beneficial when driving cross-slope, reducing side-slip by more than 50%. These results were achieved through a rotation of the walking joints to spread out the rover legs on the side to be lowered. For this, large walking joint angles of up to $\pm$ 60° were necessary, since the legs are relatively short. Since the steering axes are rotated with the walking joints, steering capability is degraded in this mode. Moreover, by lowering the rover body, ground clearance is reduced.

For Wheel Walking, a large set of tests was performed, comparing gaits, implementations, slope angles and other parameters (see Section 6.3). As a general result, Wheel Walking outperformed Normal Driving significantly in terms of overall body slip for all parameters. More specifically, on an 18° slope, slip could be reduced by more than 30 percentage

points from over 80% to 50%. At the same slope angle, the Axle-by-Axle gait proved to be slightly more efficient than the Kruse gait. However, at higher slope angles with more weight on the rear wheels, the Kruse gait showed better performance, in which the rear wheels are moved independently. Wheel Walking performance could additionally be improved by the introduction of a burnout motion. At a slope angle of 21°, the slip ratio remained at 60% compared to 80% without burnout and over 90% for Normal Driving. The positive effect only started to appear at higher inclinations with increased body slip, making burnout an optional parameter for traversing steep slopes. Shorter swivel angles were investigated as well, since they might be limited for the flight rover. A 50% reduction of the range from 30° to 15° led to a slip increase by 5 percentage points, about one third of the difference between Normal Driving and Wheel Walking with 30° swivel angle. In general, larger swivel angles allow for a longer "step" of each wheel in the walking sequence, allowing it to climb further out of its self-created pit.

As major constraints for Mars rovers, power draw and energy consumption were analyzed. Even though Wheel Walking drew 10 to 15% more power compared to Normal Driving, its total energy consumption over the travel distance on the slope was lower due to the decreased body slip and thus faster travel speed. For the burnout motion, the on-the-spot rotation of the wheels increased the instantaneous power draw, however this was more than compensated by the reduced body slip and thus the overall energy consumption over the travel distance was decreased. The aforementioned findings led to the introduction of a new Hybrid Wheel Walking gait with an extended burnout phase with which the maximally traversable slope angle was intended to be found. However, this was limited by the capabilities of the facility with a maximum slope angle of 30°, for which traversal was still possible using the Hybrid Wheel Walking gait, whereas Normal Driving failed at 21°. In this configuration, body slip remained at approximately 70%, 20 percentage points less than for the Kruse gait with regular burnout length.

Additionally to the full-body kinematics implementation of Wheel Walking, a simplified implementation based on the 2D geometry of a single leg was tested, with significantly reduced mathematical complexity and computational requirements. In both implementations, the wheel is assumed to be a rigid disc with only one point of contact on non-deformable terrain, which is a simplification for the EXM-BB2 rover driving on soft soils. The simplified implementation contains a separate body motion phase, leading to an irregular motion of the rover body compared to the full-body kinematics implementation where a constant body velocity is specified. In flatter terrain at the beginning of the slope, body slip of the simplified implementation was worse than for the full-body kinematics implementation, likely due to modeling inaccuracies caused by the simplified assumptions. However, it outperformed the full-body kinematics implementation at higher inclinations. A cause for this could not yet be determined, but might be based partly in a loss of accuracy of the contact angle estimation on steeper terrain.

8 Conclusion

In this thesis, a full-body kinematic model was developed for a mobility subsystem prototype for ESA's upcoming ExoMars rover, based on a systematic velocity propagation approach. Wheel-terrain contact angles are estimated through force-torque sensors installed at the wheel hubs. The model allows to specify desired body velocities and additional constraints on joint rates to achieve desired motions and includes a slip formulation on wheel level. Additionally, kinematic redundancies can be exploited by introducing secondary subtasks through a null-space projection method.

The EXM-BB2 rover features an articulated suspension design with 18 active and 3 passive joints. Based on the formulated kinematic model, two locomotion modes were implemented to make use of the available degrees of freedom. Balancing increases tip-over stability and reduces rover body tilt. In a test scenario, body pitch and roll could be reduced by up to 5° on uneven terrain. Moreover, the mode was able to reduce side-slip while driving sideways along a slope by more than 50%. Wheel Walking increases traction in soft soils while driving up slopes and in entrapment situations by keeping a set of wheels stationary for an anchoring effect in the soil and swiveling the others forward in relation to the rover body. In a set of slope gradeability tests, Wheel Walking outperformed Normal Driving, where only the driving joints are actuated, significantly. Using Wheel Walking, the rover managed to climb a 30° slope at 70% slip, whereas with Normal Driving, it reached 80% slip at 18° and failed to climb a 21° slope. Higher slip ratios go hand in hand with higher wheel sinkage and thus a higher risk of damage to the wheels. In addition, higher slip ratios lead to higher energy consumption due to longer travel times. In a test scenario, instantaneous power consumption for Wheel Walking was 10 to 15% higher than for Normal Driving; however, the total energy consumption over the full travel distance was 50% lower.

In light of the reduced amount of available computational power on space probes and a demand for reliable, sequence-based, deterministic algorithms, a simplified implementation of Wheel Walking was tested alongside the full-body kinematics implementation and shown to be a viable alternative. Although mathematically not as elegant, it offers similar gains in traversability performance while being algorithmically less complex.

Both implemented locomotion modes made use of the rover joints mainly intended for deployment of the wheels after landing on Mars, which proved highly beneficial. Especially the addition of Wheel Walking to the rover's locomotion capabilities seems worthwhile, since it significantly increases the traversability envelope with gradeability of steeper slopes and increased traction on soft soils.

9 Future Work

Based on the work completed in this thesis, several potential areas of improvement as well as directions for future research could be found:

- The kinematic modeling approach and the contact angle estimation were based on the assumption of a rigid wheel with a single point of contact with the terrain, which is not accurate for the EXM-BB2 rover. For the contact angle estimation, this worked well on flat ground, but was less reliable at steeper slope angles with high wheel sinkage and multiple points of contact, which might have led to the performance deterioration compared to the simplified implementation. Further improvements could try to relax these assumptions.

- For the contact angle estimation, a prediction through geometrical considerations or visual methods could be introduced. This is especially relevant since no force-torque sensors are installed on the flight rover.

- Regarding Balancing, the weighting parameters of the objective function were set by trial and error to achieve good performance. Their impact could be further analyzed and their values optimized.

- The objective function for the walking joints is based on a simple biquadratic equation to draw them towards their nominal position. This could be replaced by a better suited equation that guarantees that joint limits are not reached.

- Regarding Wheel Walking, the range of tests completed for this thesis was quite broad. Future investigations could focus on some aspects in more detail, e.g. performance characterization of all gaits depending on slope angle or optimal length of the burnout motion.

- All tests were performed on Eifel Lava soil. To verify and increase the validity of the results, further tests could be carried out using additional Mars soil simulants [56].

- The joint rate limits of the ExoMars rover could be taken into account when comparing the driving modes.

- As an entirely new set of tests, the advantage of Wheel Walking in entrapment situations could be analyzed, which is a relevant scenario for Mars rovers where improved traction would be beneficial.

- The different locomotion modes could be integrated into higher-level autonomy functionality, where the best mode is chosen based on the current situation. This could include the capability to follow given trajectories using the available locomotion modes. Automatic mode switching and path planning involving Wheel Walking has been investigated before [59, 60].

- Steering capability could be introduced to Wheel Walking as skid steering.

- To further enhance tractive performance, investigations into traction control could be carried out. Slip prediction could be based on soil parameters, IMU data or visual methods.

Bibliography

[1] Arvidson, R., Bell, J., Bellutta, P., Cabrol, N., Catalano, J., Cohen, J., Crumpler, L., Des Marais, D., Estlin, T., Farrand, W., et al., "Spirit Mars Rover Mission: Overview and selected results from the northern Home Plate Winter Haven to the side of Scamander crater," *Journal of Geophysical Research: Planets*, Vol. 115, No. E7, 2010.

[2] European Space Agency, "The ExoMars programme 2016-2020," `http://exploration.esa.int/mars/46048-programme-overview/`, 2016, accessed 2017-10-04.

[3] ESA/ATG medialab, "Trace Gas Orbiter, Schiaparelli and the ExoMars rover at Mars," `http://www.esa.int/spaceinimages/Images/2015/11/Trace_Gas_Orbiter_Schiaparelli_and_the_ExoMars_rover_at_Mars`, 2015, accessed 2017-09-27.

[4] Ellery, A., *Planetary rovers: robotic exploration of the solar system*, Springer, 2015.

[5] NASA/JPL-Caltech, "Three Generations of Rovers in Mars Yard," `https://mars.jpl.nasa.gov/mer/gallery/press/opportunity/20120117a.html`, 2012, accessed 2017-09-27.

[6] Harvey, B., *Russian planetary exploration: history, development, legacy and prospects*, Springer Science & Business Media, 2007.

[7] Kemurdjian, A., Gromov, V., Mishkinyuk, V., Kucherenko, V., and Sologub, P., "Small marsokhod configuration," *Robotics and Automation, 1992. Proceedings., 1992 IEEE International Conference on*, IEEE, 1992.

[8] Lavochkin Association, "https://apod.nasa.gov/apod/ap060114.html," `https://apod.nasa.gov/apod/ap060114.html`, 2006, accessed 2017-09-27.

[9] NASA, "PROP-M," `https://solarsystem.nasa.gov/galleries/prop-m`, 2009, accessed 2017-09-27.

[10] Science & Technology ROVER Company Ltd., http://autsys.aalto.fi/fsr/attach/Material/RCLslides.pdf, accessed 2017-09-27.

[11] Bares, J., Hebert, M., Kanade, T., Krotkov, E., Mitchell, T., Simmons, R., and Whittaker, W., "Ambler: An autonomous rover for planetary exploration," *Computer*, Vol. 22, No. 6, 1989, pp. 18–26.

[12] Kennedy, B., Okon, A., Aghazarian, H., Garrett, M., Huntsberger, T., Magnone, L., Robinson, M., and Townsend, J., "The lemur II-Class robots for inspection and maintenance of orbital structures: A system description," *Climbing and Walking Robots*, 2006, pp. 1069–1076.

[13] Gorner, M., Wimbock, T., Baumann, A., Fuchs, M., Bahls, T., Grebenstein, M., Borst, C., Butterfass, J., and Hirzinger, G., "The DLR-Crawler: A testbed for actively compliant hexapod walking based on the fingers of DLR-Hand II," *Intelligent Robots and Systems, 2008. IROS 2008. IEEE/RSJ International Conference on*, IEEE, 2008.

[14] Bartsch, S., Birnschein, T., Römmermann, M., Hilljegerdes, J., Kühn, D., and Kirchner, F., "Development of the six-legged walking and climbing robot SpaceClimber," *Journal of Field Robotics*, Vol. 29, No. 3, 2012, pp. 506–532.

[15] Kucherenko, V., Bogatchev, A., and Van Winnendael, M., "Chassis concepts for the ExoMars rover," *The 8th ESA Workshop on Advanced Space Technologies for Robotics and Automation (ASTRA'04)*, 2004.

[16] Ellery, A., Patel, N., Richter, L., Bertrand, R., and Dalcomo, J., "Exomars rover chassis analysis and design," *Proceedings of the 8th international symposium on artificial intelligence, robotics and automation in space (iSAIRAS), ESTEC*, 2005.

[17] Michaud, S., Richter, L., Thueer, T., Gibbesch, A., Huelsing, T., Schmitz, N., Weiss, S., Krebs, A., Patel, N., Joudrier, L., et al., "Rover chassis evaluation and design optimisation using the RCET," 2006.

[18] Michaud, S., Hoepflinger, M., Thueer, T., Lee, C., Krebs, A., Despont, B., Gibbesch, A., and Richter, L., "Lesson learned from exomars locomotion system test campaign," *Proceedings of 10th Workshop on Advanced Space Technologies for Robotics and Automation, ESTEC The Netherlands*, 2008.

[19] Patel, N., Slade, R., and Clemmet, J., "The ExoMars rover locomotion subsystem," *Journal of Terramechanics*, Vol. 47, No. 4, 2010, pp. 227–242.

[20] ESA/ATG medialab, "ExoMars Rover - Front View," `http://exploration.esa.int/mars/58841-exomars-rover/`, 2017, accessed 2017-09-28.

[21] McCoubrey, R., Smith, J., Cernusco, A., Durrant, S., Phillips, R., Jessen, S., Jones, H., and Fulford, P., "ExoMars Suspension and Locomotion," *iSAIRAS 2014*, 2014, pp. 4–7.

[22] Poulakis, P., Vago, J., Loizeau, D., Vicente-Arevalo, C., Hutton, A., McCoubrey, R., Arnedo-Rodriguez, J., Smith, J., Boyes, B., Jessen, S., et al., "Overview and development status of the exomars rover mobility subsystem," *Proc. Adv. Space Technol. Robot. Autom.*, 2015.

[23] Hu, Z., "Study and implementation of wheel walking for a Mars rover," 2007.

[24] VNIITRANSMASH, "Specimens of space technology, Earth based demonstrator of planetary rovers, running mock-ups 1963-2002," Tech. rep., VNIITRANSMASH, St Petersburg, Russia, 2002.

[25] Bogatschev, A., Gromov, V., Koutcherenko, V., Matrossov, S., and Petriga, V., "Walking and wheel-walking robots," *Proceedings of the 3rd International Conference on Climbing and Walking Robots*, 2000.

[26] Creager, C., Moreland, S., Skonieczny, K., Johnson, K., Asnani, V., and Gilligan, R., "Benefit of "Push-Pull" Locomotion for Planetary Rover Mobility," *Earth and Space 2012: Engineering, Science, Construction, and Operations in Challenging Environments*, 2012, pp. 11–20.

[27] Hu, Z. and Halme, A., "Implementation of Wheel Walking for a Mars Rover," 2009.

[28] Grosse-Scharmann, F., "Die Triebkraftsteigerung bei Geländefahrzeugen durch das Schub-Schritt-Verfahren," *Landtechnische Forschung*, Vol. 11, No. 4, 1960.

[29] Czako, T., Janosi, Z., and Liston, R., "An analysis of multi-element inching vehicles," *Center Line, MI: US Army Tank-automotive Center, Land Locomotion Laboratory*, 1963.

[30] Moreland, S., Skonieczny, K., Wettergreen, D., Asnani, V., Creager, C., and Oravec, H., "Inching locomotion for planetary rover mobility," *Aerospace Conference, 2011 IEEE*, IEEE, 2011.

[31] Cordes, F., Oekermann, C., Babu, A., Kuehn, D., Stark, T., and Kirchner, F., "An active

suspension system for a planetary rover," *Proceedings of the International Symposium on Artificial Intelligence, Robotics and Automation in Space (i-SAIRAS 2014), June*, 2014.

[32] ESA/ATG medialab, "ExoMars Rover - Side View," `http://exploration.esa.int/mars/58838-exomars-rover/`, 2017, accessed 2017-09-28.

[33] Azkarate, M., Zwick, M., Hidalgo-Carrio, J., Nelen, R., Wiese, T., Poulakis, P., Joudrier, L., and Visentin, G., "First experimental investigations on wheel-walking for improving triple-bogie rover locomotion performances," *Proceedings Advanced Space Technologies for Robotics and Automation (ASTRA). Noordwijk, The Netherlands: European Space Agency*, 2015.

[34] Siciliano, B. and Khatib, O., *Springer handbook of robotics*, Springer, 2016.

[35] Craig, J. J., *Introduction to robotics: mechanics and control*, Vol. 3, Pearson Prentice Hall Upper Saddle River, 2005.

[36] Muir, P. F. and Neuman, C. P., "Kinematic modeling of wheeled mobile robots," *Journal of Field Robotics*, Vol. 4, No. 2, 1987, pp. 281–340.

[37] Tarokh, M., McDermott, G., Hayati, S., and Hung, J., "Kinematic modeling of a high mobility Mars rover," *Robotics and Automation, 1999. Proceedings. 1999 IEEE International Conference on*, Vol. 2, IEEE, 1999.

[38] Tarokh, M. and McDermott, G. J., "Kinematics modeling and analyses of articulated rovers," *IEEE Transactions on Robotics*, Vol. 21, No. 4, 2005, pp. 539–553.

[39] Tarokh, M. and McDermott, G., "A systematic approach to kinematics modeling of high mobility wheeled rovers," *Robotics and Automation, 2007 IEEE International Conference on*, IEEE, 2007.

[40] Tarokh, M., Ho, H. D., and Bouloubasis, A., "Systematic kinematics analysis and balance control of high mobility rovers over rough terrain," *Robotics and Autonomous Systems*, Vol. 61, No. 1, 2013, pp. 13–24.

[41] Iagnemma, K., Rzepniewski, A., Dubowsky, S., and Schenker, P., "Control of robotic vehicles with actively articulated suspensions in rough terrain," *Autonomous Robots*, Vol. 14, No. 1, 2003, pp. 5–16.

[42] Iagnemma, K. and Dubowsky, S., "Vehicle wheel-ground contact angle estimation:

with application to mobile robot traction control," *7th International Symposium on Advances in Robot Kinematics, ARK 00*, 2000.

[43] Xu, H., Liu, X., Fu, H., Putra, B. B., and He, L., "Visual contact angle estimation and traction control for mobile robot in rough-terrain," *Journal of Intelligent & Robotic Systems*, Vol. 74, No. 3-4, 2014, pp. 985.

[44] Hidalgo, J. and Cordes, F., "Kinematics modeling of a hybrid wheeled-leg planetary rover," *International Symposium on Artificial Intelligence, Robotics and Automation in Space (Turin)*, 2012.

[45] Hidalgo, J., "Navigation and slip kinematics for high performance motion models," *Symposium on Advanced Space Technologies in Robotics and Automation*, 2013.

[46] Chang, Y., Ma, S., Wang, H., and Tan, D., "A kinematic modeling method for a wheeled mobile robot," *Mechatronics and Automation, 2009. ICMA 2009. International Conference on*, IEEE, 2009.

[47] Seegmiller, N. and Kelly, A., "Enhanced 3D Kinematic Modeling of Wheeled Mobile Robots." *Robotics: Science and Systems*, Vol. 2, 2014.

[48] Apfelbeck, M., Kuß, S., Rebele, B., Michaud, S., Boesch, C., Krpoun, R., and Schäfer, B., "ExoMars Phase B2 breadboard locomotion sub-system test campaign," *Proceedings of Advanced Space Technologies for Robotics and Automation (ASTRA'11)*, 2011.

[49] Wedler, A., Rebele, B., Reill, J., Suppa, M., Hirschmüller, H., Brand, C., Schuster, M., Vodermayer, B., Gmeiner, H., Maier, A., et al., "LRU - lightweight rover unit," *Proc. of the 13th Symposium on Advanced Space Technologies in Robotics and Automation (ASTRA)*, 2015.

[50] Xsens Technologies B.V., "MTi and MTx User Manual and Technical Documentation," 2010.

[51] Schmidt, F. and Burger, R., "How we deal with software complexity in robotics: links and nodes and the robotkernel," *14th IEEE-RAS International Conference on Humanoid Robots (Humanoids)*, IEEE, 2014.

[52] Burger, R., Schmidt, F., and Brunner, B., "Development of a runtime-configurable robotic hardware abstraction framework," *13th Symposium on Advanced Space Technologies in Robotics and Automation (ASTRA), RCOS Forum*, ESA, 2015.

[53] De Luca, A., "Robots with kinematic redundancy, lecture slides to Robotics 2," `http://www.diag.uniroma1.it/~deluca/rob2_en/02_KinematicRedundancy.pdf`, 2017, accessed 2017-10-15.

[54] Nakamura, Y., *Advanced robotics: redundancy and optimization*, Addison-Wesley Longman Publishing Co., Inc., 1990.

[55] Apfelbeck, M., Kuß, S., Rebele, B., and Schäfer, B., "A systematic approach to reliably characterize soils based on Bevameter testing," *Journal of Terramechanics*, Vol. 48, No. 5, 2011, pp. 360–371.

[56] Brunskill, C., Patel, N., Gouache, T. P., Scott, G. P., Saaj, C. M., Matthews, M., and Cui, L., "Characterisation of martian soil simulants for the ExoMars rover testbed," *Journal of Terramechanics*, Vol. 48, No. 6, 2011, pp. 419–438.

[57] Buse, F., *Machbarkeitsstudie für einen roboterbasierten Radprüfstand zur Entwicklung von Mars Mondrovern*, Ph.D. thesis, RWTH Aachen, 2015.

[58] Eade, E., "Lie Groups for 2D and 3D Transformations," `http://ethaneade.com/lie.pdf`, 2017, accessed 2017-10-15.

[59] Leppänen, I. et al., *Automatic locomotion mode control of wheel-legged robots*, Helsinki University of Technology, 2007.

[60] Pérez-del Pulgar, C., Sánchez, J., Sánchez, A., Azkarate, M., and Visentin, G., "Path planning for reconfigurable rovers in planetary exploration," *Advanced Intelligent Mechatronics (AIM), 2017 IEEE International Conference on*, IEEE, 2017.